



Plasma Physics

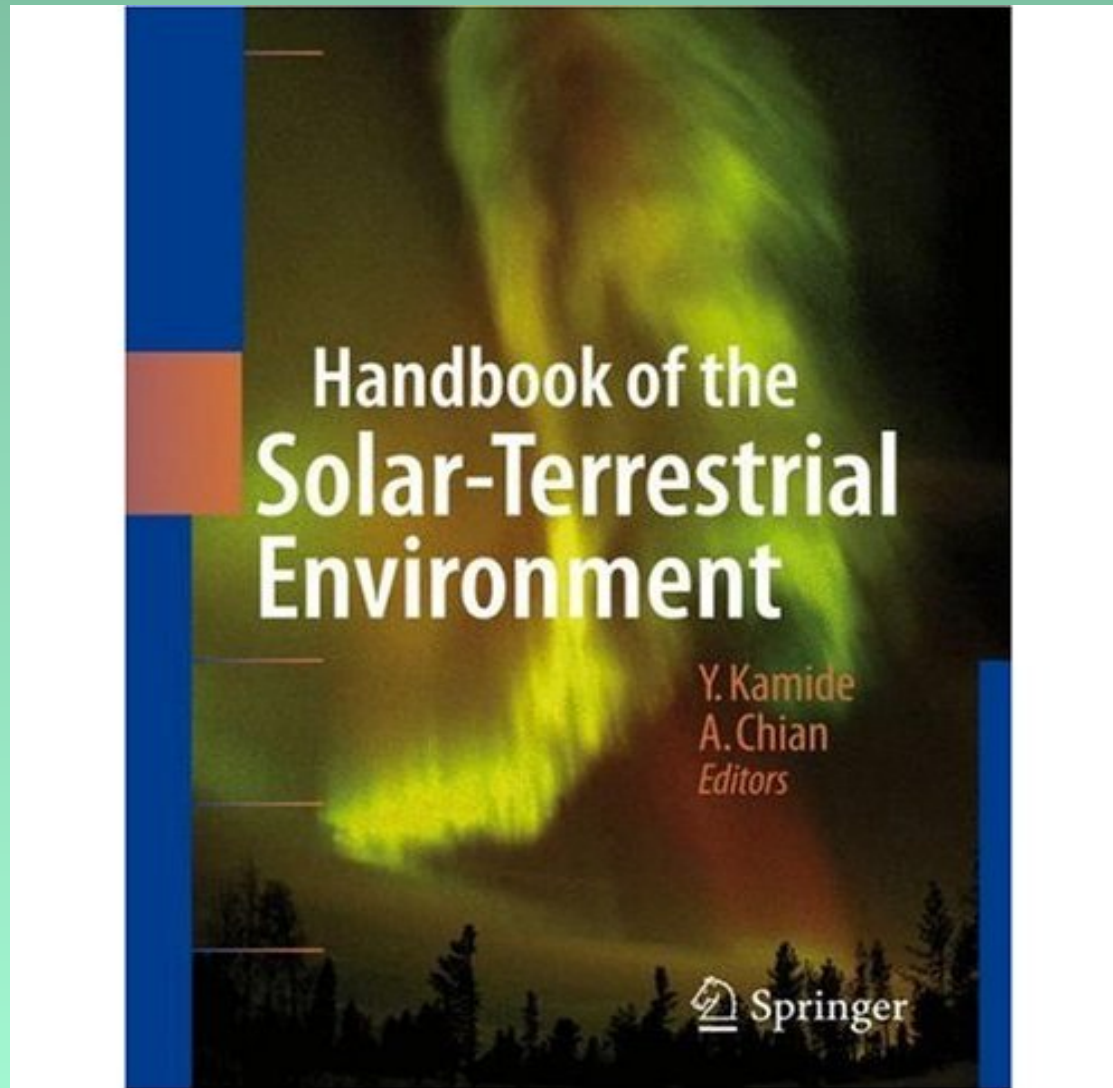
Abraham Chian

*National Institute for Space Research (INPE), Brazil
&
University of Adelaide, Australia*

abraham.chian@gmail.com

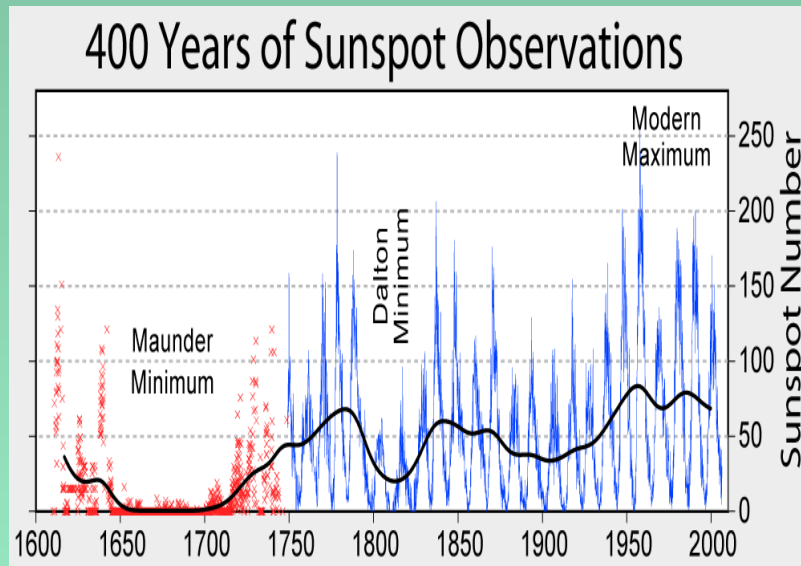
Outline

- **A brief history of space plasma physics**
- **Langmuir waves, instabilities, chaos & turbulence**
- **Alfvén waves, instabilities, chaos & turbulence**
- **Magnetic reconnection, coherent structures & turbulence**
- **Applications of plasma physics**

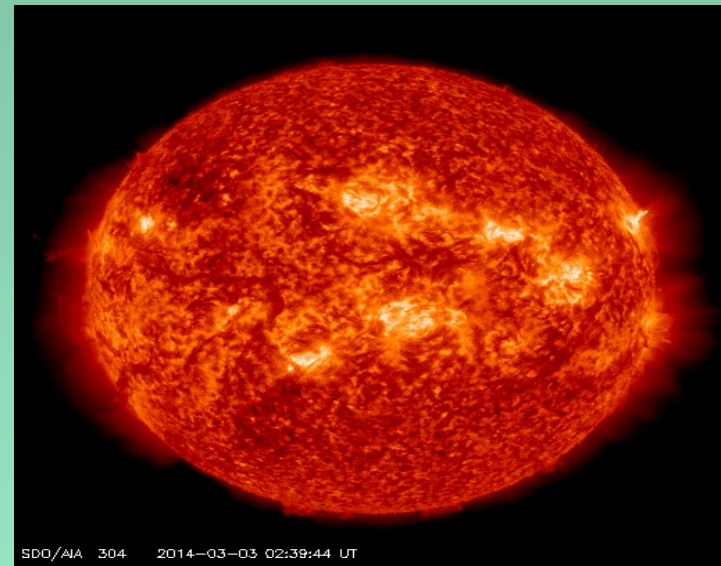


Complex dynamics of the Sun: Intermittent turbulence

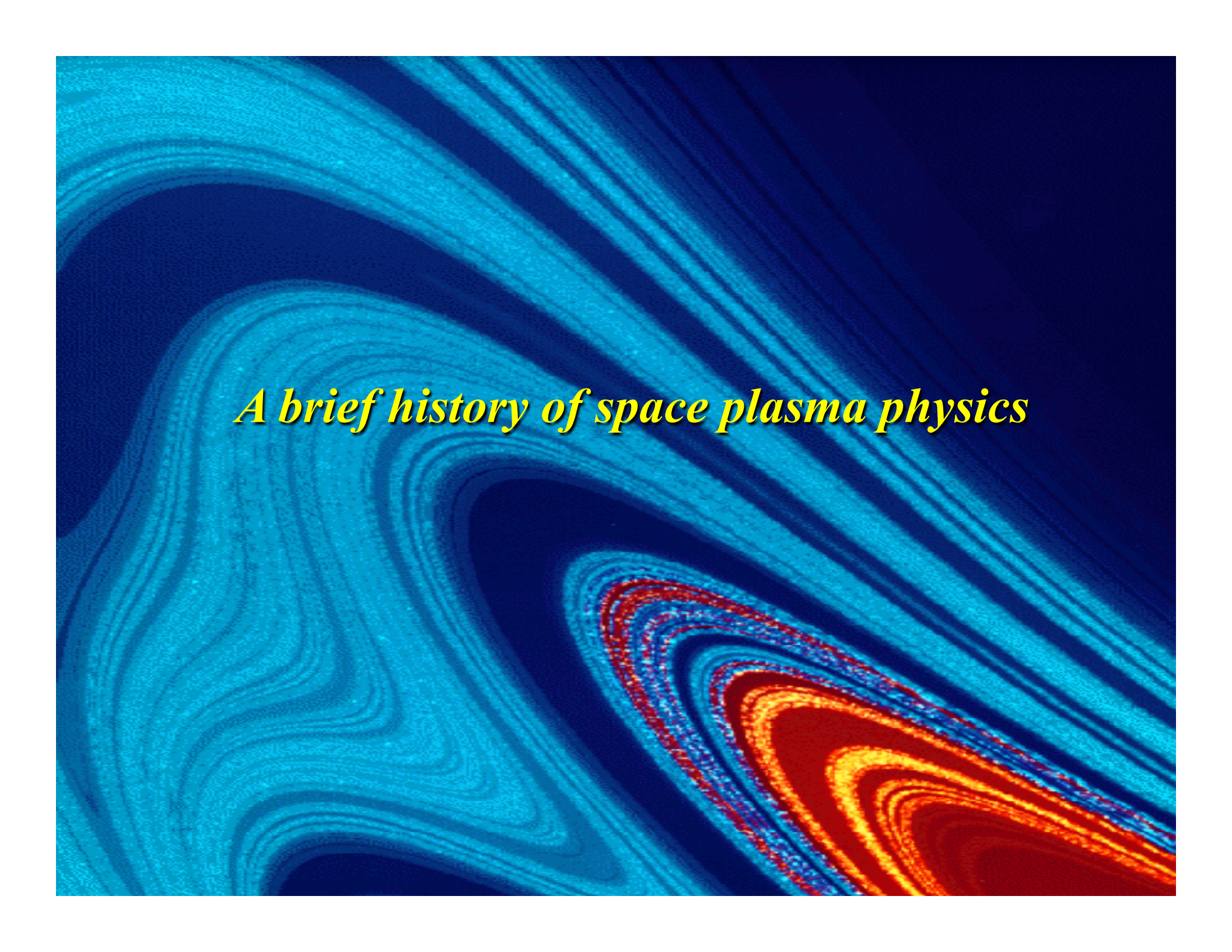
Sunspot cycles



UV image of active Sun



- Time series display random regime switching between laminar periods of small-amplitude fluctuations and bursty periods of large-amplitude fluctuations
- Probability distribution functions (PDF) display a non-Gaussian shape (broad-tail and sharp peak) due to an excess of large- and small-amplitude fluctuations at small scales
- Power spectra display a power-law behavior indicative of multiscale interactions
- Images display localized regions of patchiness (multifractality) associated with coherent structures

The background of the slide is an abstract, high-resolution image featuring complex, wavy patterns. The color palette is primarily deep blues and cyan, with a prominent feature in the lower right quadrant that transitions into bright red and orange, resembling a plasma or a high-energy field. The overall effect is dynamic and scientific.

A brief history of space plasma physics

1 An Overview of the Solar–Terrestrial Environment

A.C.-L. Chian, Y. Kamide

1.1	Introduction	2
1.2	Overview and History of Solar-Terrestrial Environment Research	2
1.2.1	Sun.....	2
1.2.2	Solar Wind	5
1.2.3	Magnetosphere–Ionosphere–Thermosphere	7
1.2.4	Geomagnetism and Geomagnetic Storms/Substorms	9
1.2.5	Aurora	11
1.2.6	Planets and Comets	13
1.2.7	Cosmic Rays	14
1.3	Nature of the Solar-Terrestrial Environment	14
1.3.1	Linear Waves	15
1.3.2	Instabilities	16
1.3.3	Nonlinear Waves	17
1.3.4	Turbulence	18
1.4	Applications	19
1.4.1	Space Weather and Space Climate	19
1.4.2	Plasma Astrophysics	20
1.4.3	Controlled Thermonuclear Fusion	21
1.5	Concluding Remarks	21
	References	22

10 Space Plasmas

C. Uberoi

10.1	Characteristic Properties of Plasmas	250
10.2	Particles in Space Plasmas	252
10.2.1	Motion of Charged Particles in a Uniform Magnetic Field	252
10.2.2	Particle Drifts	253
10.2.3	Magnetic Mirrors	255
10.2.4	Motion in a Dipole Magnetic Field	256
10.2.5	Currents	256
10.3	Mathematical Equations for Plasmas	257
10.4	Plasma as an MHD Fluid	259
10.4.1	MHD Equations	260
10.4.2	Motion of the Magnetic Field	261
10.4.3	Hydromagnetic Equilibrium	263
10.4.4	Transport Coefficients: Electrical Conductivity	263
10.5	Waves in Space Plasmas	264
10.5.1	Electromagnetic Waves	264
10.5.2	Dielectric Constant for Magnetized Plasma	266
10.5.3	Electrostatic Waves	268
10.5.4	Magnetohydrodynamic Waves	269
10.5.5	Kinetic Theory of Plasma Waves	270
10.5.6	Surface Waves	271
10.6	Equilibria and Their Stability	273
10.6.1	Interface Instabilities	273
10.6.2	Two-stream Instability	275
10.6.3	Tearing Mode Instability	276
10.7	Conclusion	277
	References	277

12 Nonlinear Plasmas

L. Stenflo and P.K. Shukla

12.1	Introduction	312
12.2	Stimulated Scattering of Electromagnetic Waves	312
12.3	Resonant Three-Wave Interactions in Plasmas	316
12.4	Parametric Instabilities of Magnetic Field-Aligned Alfvén Waves	318
12.5	Kinetic Alfvén Waves Driven Zonal Flows	320
12.6	Ponderomotive Forces and Plasma Density Modifications	322
12.7	Modulated Circularly Polarized Dispersive Alfvén Waves	323
12.8	Electron Joule Heating	324
12.9	Self-Interaction Between DSAWs	325
12.10	Nonlinear Drift-Alfvén–Shukla–Varma Modes	325
12.11	Summary and Conclusions	327
	References	328

Irving Langmuir (1881-1957)

Langmuir waves - plasma



Langmuir discussed plasma oscillations for the first time in 1928 (Langmuir, 1928; Langmuir and Tonks, 1929). In fact, he found that the characteristic behavior of the jelly-like movement of the group of charged particles was similar to that of blood plasma and this led him to use the name “plasma”. Plasma frequency is also sometimes called Langmuir frequency.

Plasma Oscillations The plasma electron oscillations arise as a consequence of the property of the plasma to try to remain neutral. If the electrons in a plasma are displaced from a uniform background of ions, electric fields will be built up in such a direction so as to restore the neutrality of the plasma by pulling the electrons back to their original position. Because of their inertia, the electrons will overshoot and oscillate around their equilibrium positions with a characteristic frequency namely the radian plasma frequency

$$\omega_p = \left(\frac{4\pi n_e^2}{m_e} \right)^{1/2} . \quad (10.5)$$

$$\omega^2 = \omega_p^2$$

Voyager 1 Wide Band

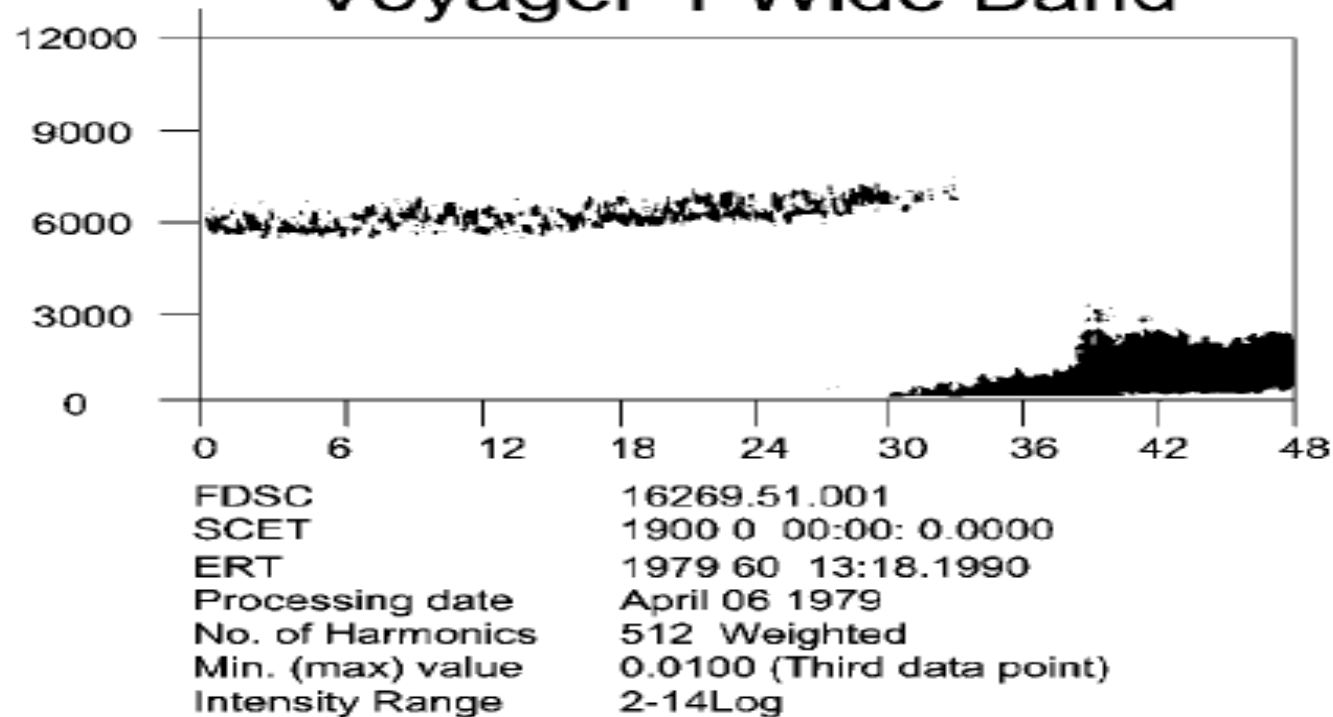


Fig. 10.2. Jovian plasma oscillations: Frequency-time diagram of the electron plasma oscillations detected in Jupiter's magnetosphere by the spacecraft *Voyager*. The plasma probe picked up the signals on 1 March 1979, which when plotted on the frequency-time graph, showed constant frequency oscillations. A frequency of 6000 Hz was calculated to be the plasma frequency in the vicinity of the spacecraft. After the 33 seconds mark, plasma turbulence features are seen

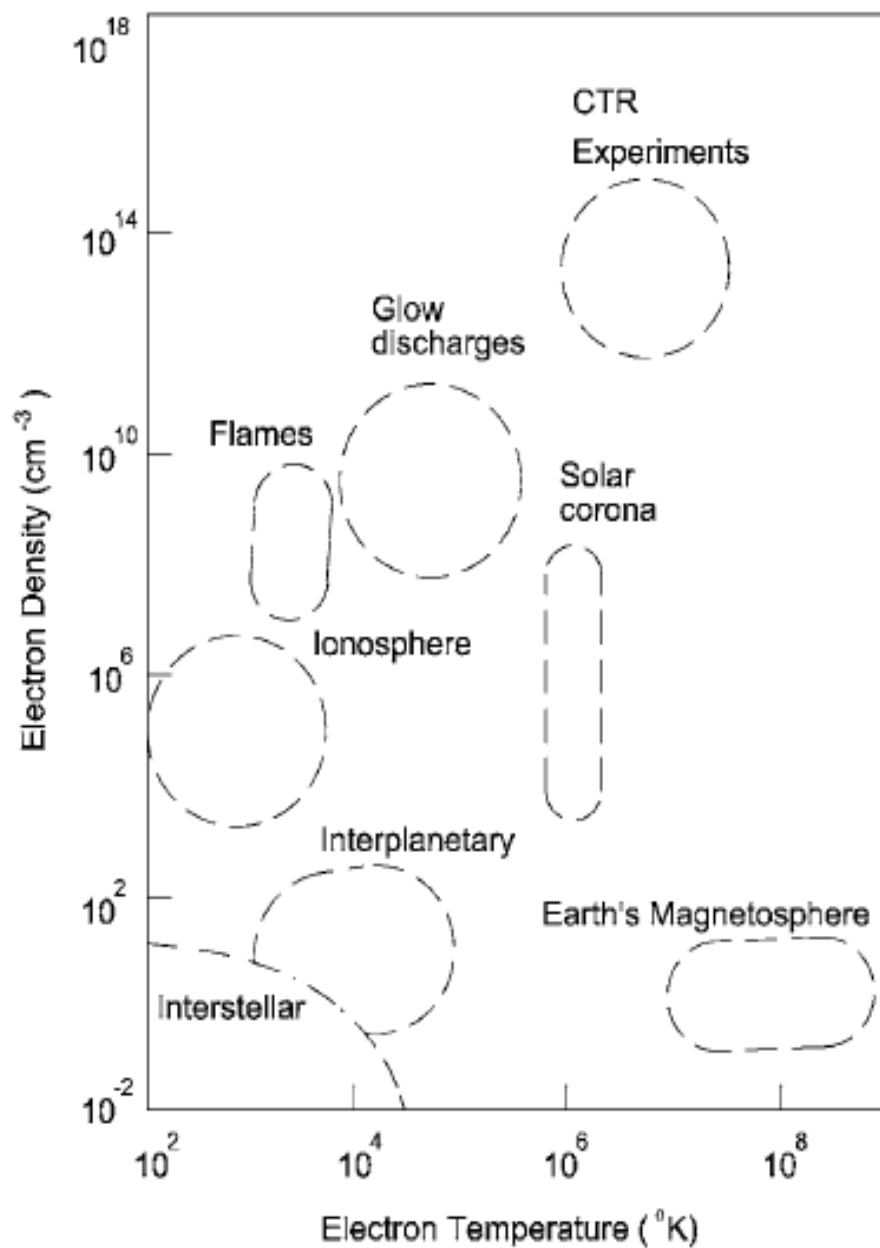


Fig. 10.1. Plasma parameters for a variety of natural plasmas in terms of electron density and temperature. For comparison, laboratory plasmas used for controlled thermonuclear reaction (CTR) experiments are also shown

Guglielmo Marconi (1874-1937)
radio wave propagation via ionosphere



For plasma with $\epsilon(\omega)$ given by (10.86) the dispersion relation for transverse waves can be written as from (10.92) as

$$\omega^2 = c^2 k^2 + \omega_p^2. \quad (10.94)$$

Note that v_{ph} for a light wave in a plasma is greater than the velocity of light. However,

$$v_g = \frac{\partial \omega}{\partial k} = \frac{c^2}{v_{ph}} < c.$$

At $\omega = \omega_p$, $k = 0$, which means that electromagnetic wave has a cut-off frequency at $\omega = \omega_p$ in a plasma. For $\omega < \omega_p$, k becomes imaginary and the wave is damped with a characteristic length $1/|k|$ (Fig. 10.6).

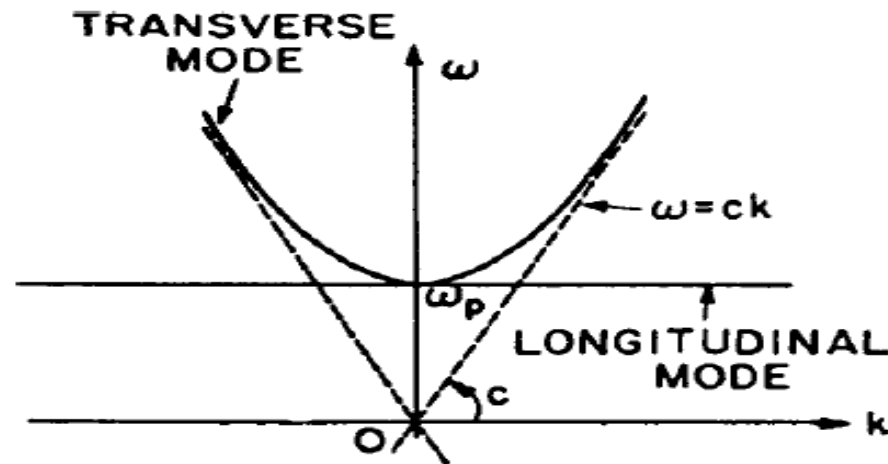


Fig. 10.6. Dispersion relation of electromagnetic waves in a cold, unmagnetized plasma

Hannes Alfvén

(1908-1995)



Alfvén, Nature (1942): *Existence of Electromagnetic-Hydrodynamic Waves*

Existence of Electromagnetic-Hydrodynamic Waves

If a conducting liquid is placed in a constant magnetic field, every motion of the liquid gives rise to an E.M.F. which produces electric currents. Owing to the magnetic field, these currents give mechanical forces which change the state of motion of the liquid.

Thus a kind of combined electromagnetic-hydrodynamic wave is produced which, so far as I know, has as yet attracted no attention.

Consider the simple case when $\sigma = \infty$, $\mu = 1$ and the imposed constant magnetic field H_0 is homogeneous and parallel to the z -axis. In order to study a plane wave we assume that all variables depend upon the time t and z only. If the velocity v is parallel to the x -axis, the current i is parallel to the y -axis and produces a variable magnetic field H' in the x -direction. By elementary calculation we obtain

$$\frac{d^2 H'}{dz^2} = \frac{4\pi\sigma}{H_0^2} \frac{d^2 H'}{dt^2},$$

which means a wave in the direction of the z -axis with the velocity

$$V = \frac{H_0}{\sqrt{4\pi\sigma}}.$$

Alfvén Waves At the very low frequency $\omega \ll \omega_{ci}$, the motion of ions cannot be neglected. In this case, we can show that

$$n_R^2 = n_L^2 = 1 + \frac{4\pi\rho c^2}{B_0^2}, \quad (10.104)$$

where $\rho = n_0 m_i$. This gives

$$\frac{c^2 k^2}{\omega^2} = 1 + \frac{c^2}{v_A^2}, \quad (10.105)$$

As $v_A^2 \ll c^2$, this gives the Alfvén wave with velocity $v_A = B_0 / (4\pi\rho)^{1/2}$. This is a very important result, be-

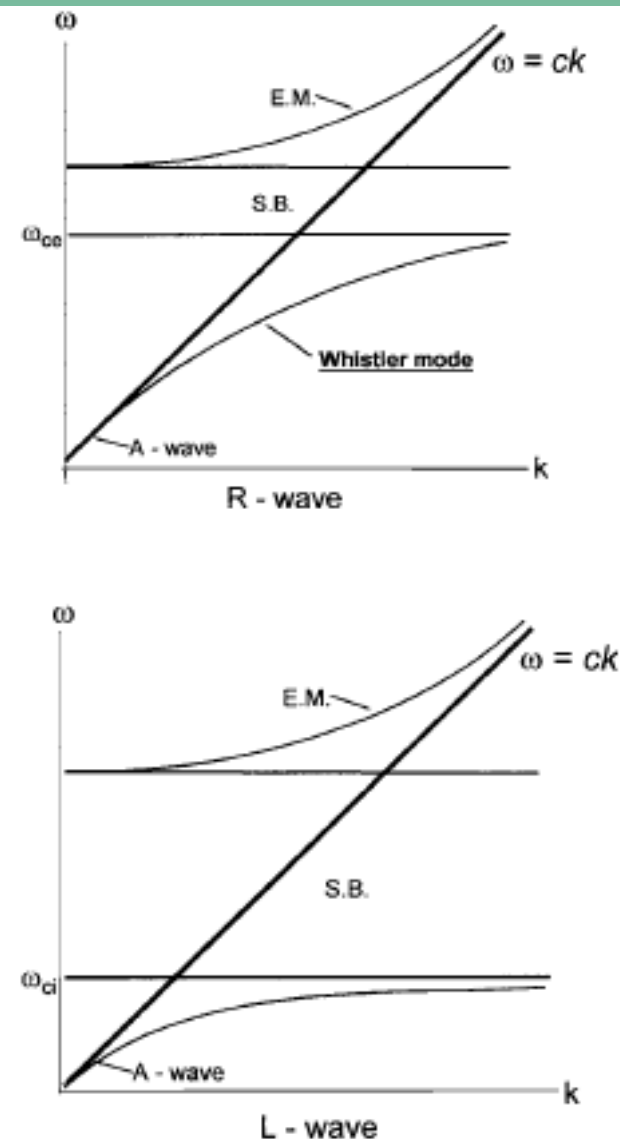
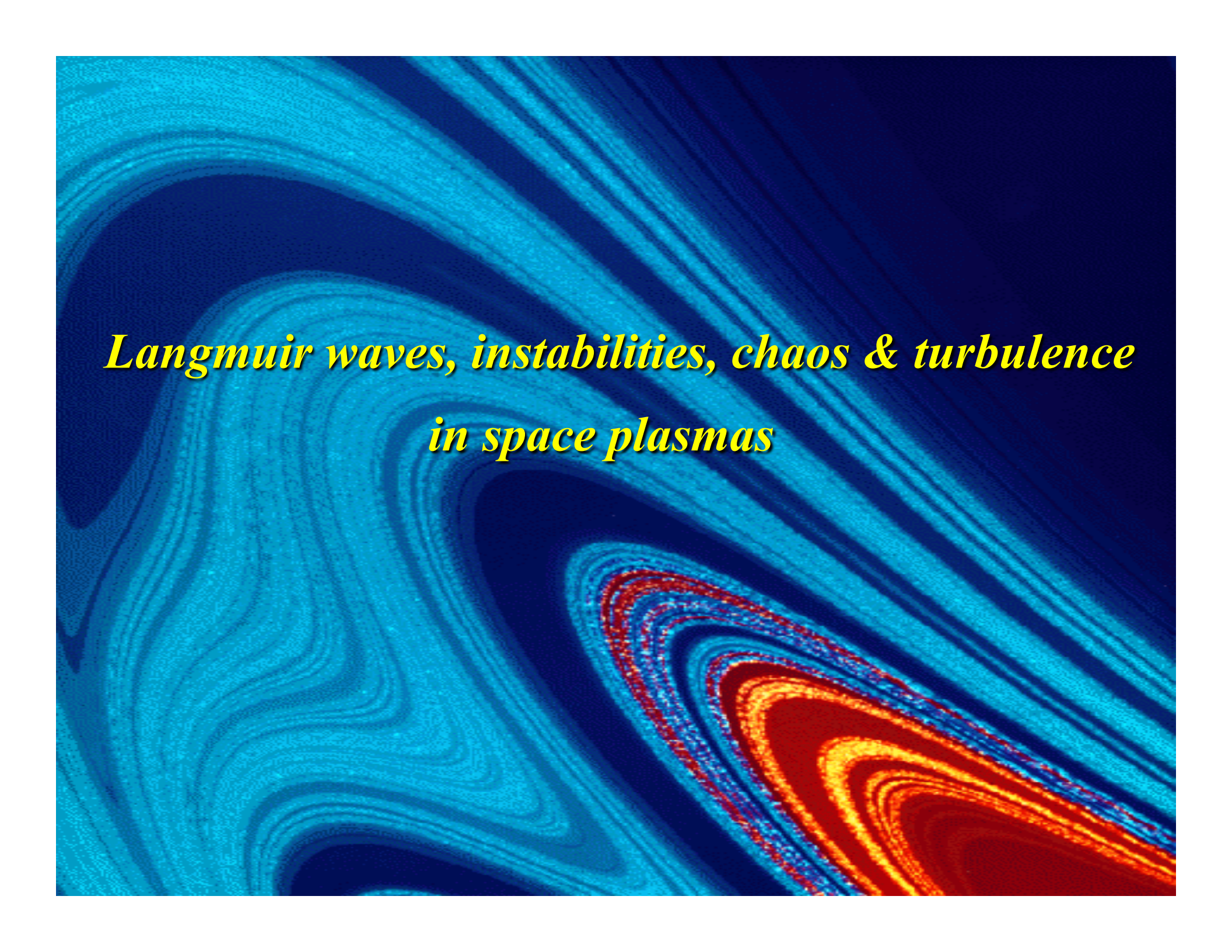
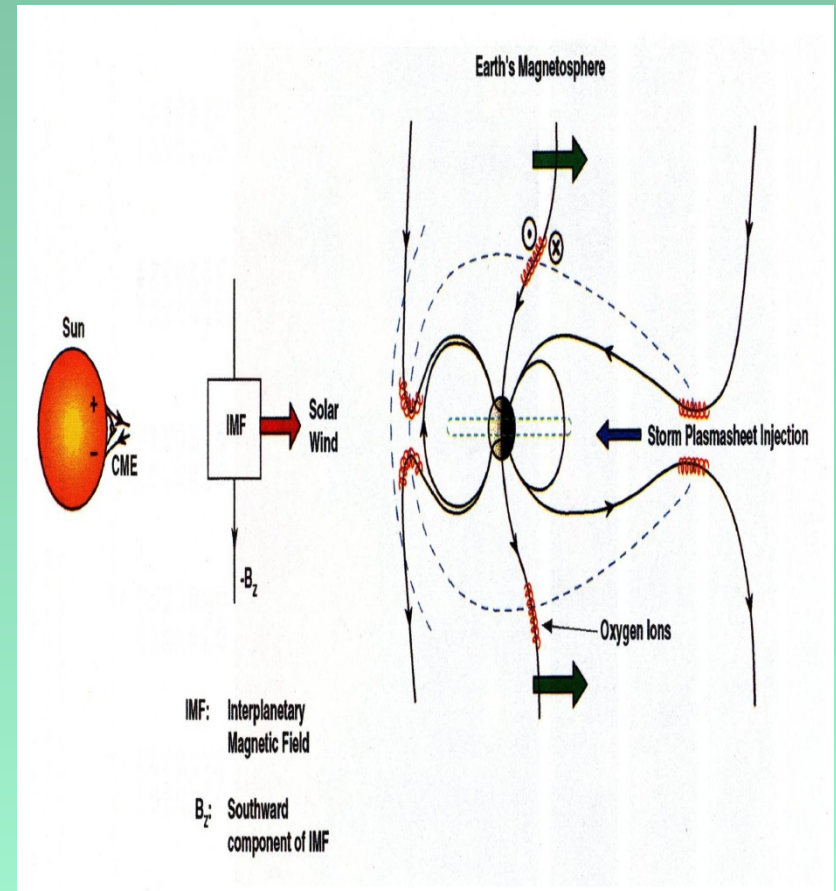
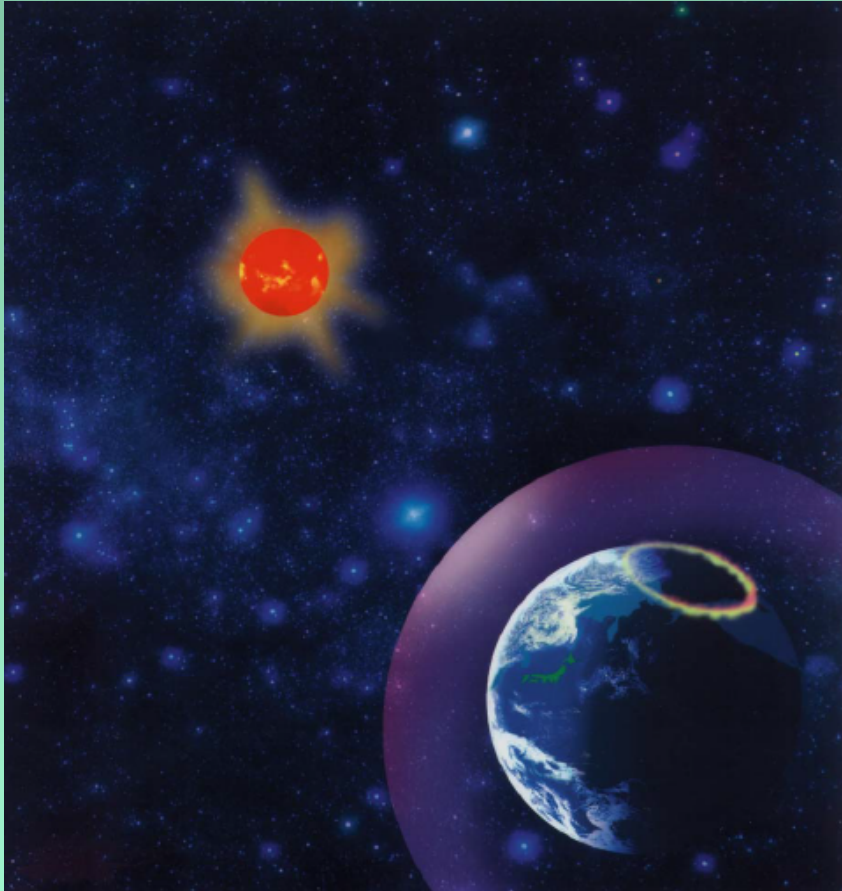


Fig. 10.7. Dispersion relation of R and L electromagnetic waves in magnetized plasma



*Langmuir waves, instabilities, chaos & turbulence
in space plasmas*

Complex dynamics of solar-terrestrial relation: Sun-Earth relation & Space weather



Gonzalez and Tsurutani, INPE/JPL

4 Solar Wind

E.N. Parker

4.1	Introduction	96
4.2	The Corona	96
4.3	Outward Decline of Density and Pressure	97
4.4	Comets and Solar Corpuscular Radiation	98
4.5	Cosmic Ray Variations	98
4.6	Plasma in Interplanetary Space	99
4.7	The State of the Corona	100
4.8	Theoretical Foundations of Hydrodynamics and Magnetohydrodynamics	101
4.9	Kinetic Conditions in the Corona	103
4.10	Magnetohydrodynamics	104
4.11	Hydrodynamic Expansion of the Solar Corona	105
4.12	Sufficient Conditions on Coronal Temperature	107
4.13	Analogy with Expansion Through a Laval Nozzle	108
4.14	Gravitational Throttling of Coronal Expansion	109
4.15	Wind Density and Solar Mass Loss	110
4.16	Magnetic Fields and Streams in the Solar Wind	112
4.17	Discussion	113
	References	114

6 Solar Radio Emissions

J.-L. Bougeret and M. Pick

6.1	Introduction	134
6.2	Radio Wave Propagation	135
6.2.1	Basics	135
6.2.2	Scattering of Radio Waves	137
6.3	Thermal Radiation from the Sun	137
6.3.1	Microwave Domain	137
6.3.2	Decimeter–Meter Domain	137
6.4	Solar Radio Bursts	138
6.4.1	Emission Mechanisms	139
6.4.2	Electron Beams	139
6.4.3	Remote Tracking of Collisionless Shock Waves	141
6.4.4	Radio Emission Following Flares and Large-Scale Disturbances	142
6.5	In Situ Wave and Particle Measurements	144
6.6	Radio Signatures of Coronal and Interplanetary Coronal Mass Ejections .	145
6.6.1	Flare/CME Events: Lift-Off and Angular Spread in the Corona	146
6.6.2	Direct Radio CME Imaging	146
6.6.3	Interplanetary Coronal Mass Ejections	147
6.7	Conclusions: The Relevance of Radio Observations to the Understanding of the Solar-Terrestrial Environment	148
	References	150

THE ASTROPHYSICAL JOURNAL, 330:L77-L80, 1988 July 1

© 1988. The American Astronomical Society. All rights reserved. Printed in U.S.A.

NONLINEAR GENERATION OF THE FUNDAMENTAL RADIATION OF INTERPLANETARY TYPE III RADIO BURSTS

ABRAHAM C.-L. CHIAN AND MARIA V. ALVES

Institute for Space Research-INPE, São José dos Campos-SP, Brazil

Received 1988 February 18; accepted 1988 March 30

ABSTRACT

A new generation mechanism of interplanetary type III radio bursts at the fundamental electron plasma frequency is discussed. It is shown that the electromagnetic oscillating two-stream instability, driven by two oppositely propagating Langmuir waves, can account for the experimental observations. In particular, the major difficulties encountered by the previously considered electromagnetic decay instability are removed.

Subject headings: plasmas — Sun: radio radiation — Sun: solar wind

A theory of the fundamental plasma emission of type-III solar radio bursts

M. V. Alves¹, A. C.-L. Chian^{1,2}, M. A. E. De Moraes¹, J. R. Abalde³, and F. B. Rizzato^{2,4}

¹ National Institute for Space Research – INPE, PO Box 515, 12221-970 S. J. Campos, SP, Brazil
e-mail: achian@dge.inpe.br; moraes@plasma.inpe.br

² World Institute for Space Environment Research, WISER, University of Adelaide, SA5005, Australia

³ UNIVAP-IPD, Av. Shishima Hifumi 2911, 12224-000 S. J. dos Campos, SP, Brazil
e-mail: abalde@univap.br

⁴ Institute of Physics, UFRGS, PO Box 15051, 91500 Porto Alegre, RS, Brazil
e-mail: rizzato@if.ufrgs.br

Received 25 March 2002 / Accepted 6 May 2002

Abstract. Results from plasma wave experiments in spacecraft give support to nonlinear interactions involving Langmuir waves, electromagnetic waves and ion-acoustic waves in association with type III solar radio bursts. In this paper we present a theory of the fundamental plasma emission of type-III solar radio bursts. Starting from the generalized Zakharov equations, considering the pump wave as a pair of oppositely propagating Langmuir waves with different amplitudes, and the excitation of electromagnetic and induced Langmuir waves, we obtain a general dispersion relation for the coupled waves. We numerically solve the general dispersion relation using the pump wave amplitude and plasma parameters as observed in the interplanetary medium. We compare our results with previous models. We find that the stability properties depend on the pump wave numbers and on the ratio of wave amplitude between the forward and backward pump wave. The inclusion of a second pump wave allows the simultaneous generation of up and down converted electromagnetic waves. The presence of a second pump with different amplitude from the first one brings a region of convective instability not present when amplitudes are the same.

Langmuir waves & turbulence:

Type-III radio waves emitted by a solar flare electron beam

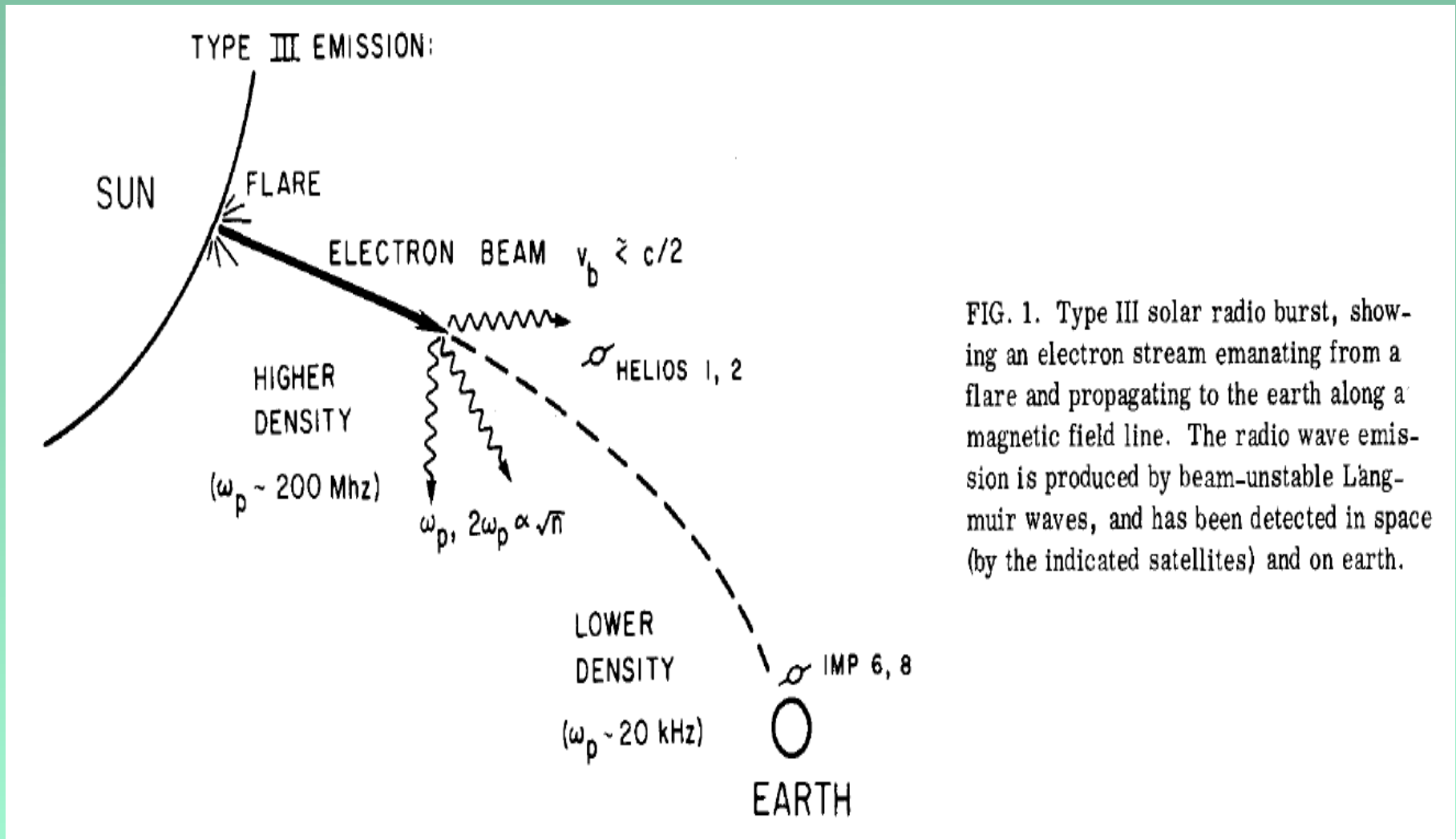
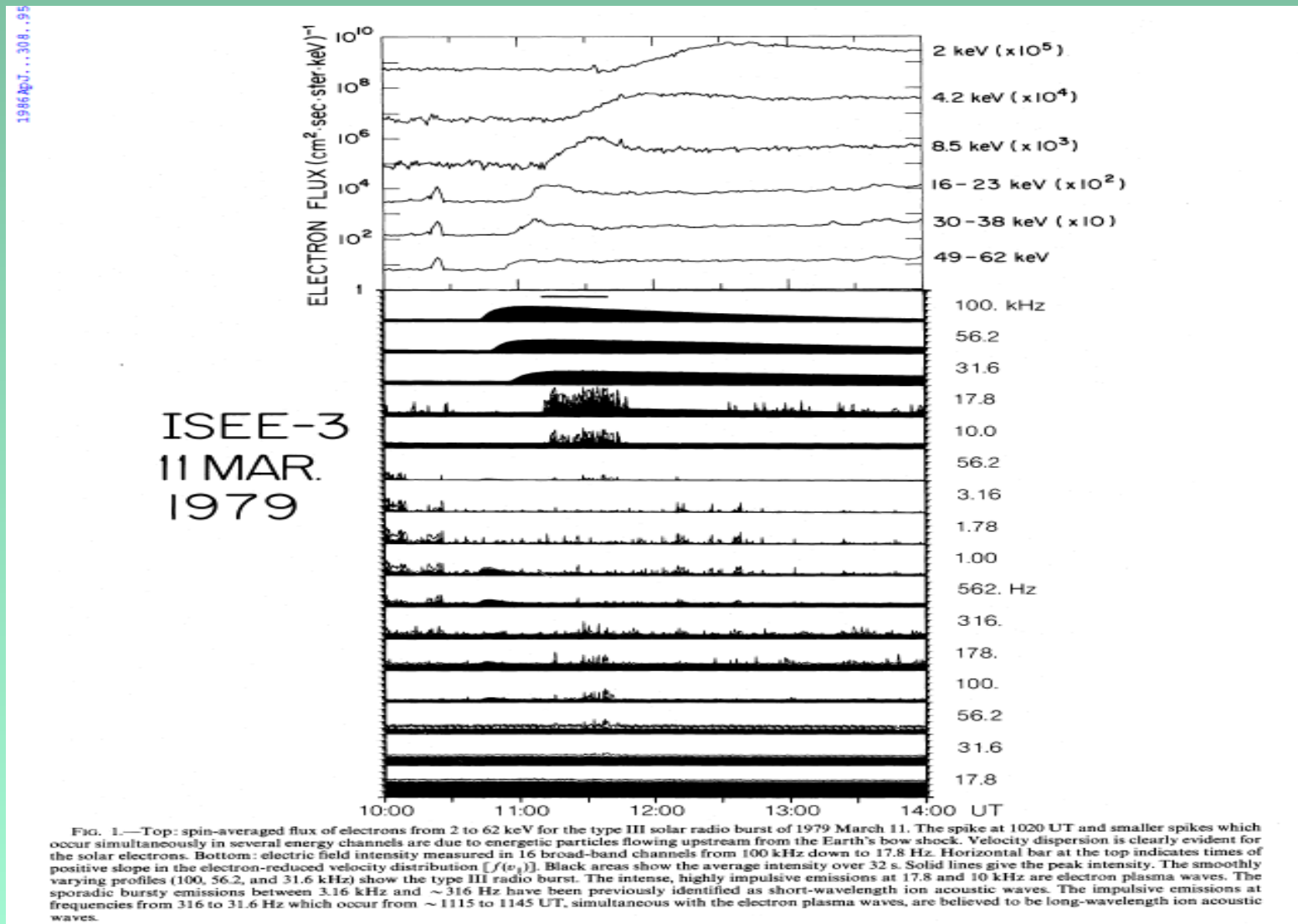


FIG. 1. Type III solar radio burst, showing an electron stream emanating from a flare and propagating to the earth along a magnetic field line. The radio wave emission is produced by beam-unstable Langmuir waves, and has been detected in space (by the indicated satellites) and on earth.

Ref: Goldman et al., PF (1980)

Observational evidence of nonlinear wave-wave interactions: Type-III radio bursts, Langmuir waves, ion-acoustic waves



Refs: Lin et al. ApJ 1986; Henri et al. JGR 2009

Observational evidence of nonlinear coupling of Langmuir waves and ion-acoustic waves in a type-III event

1986ApJ...308...9

958

LIN ET AL.

Vol. 308

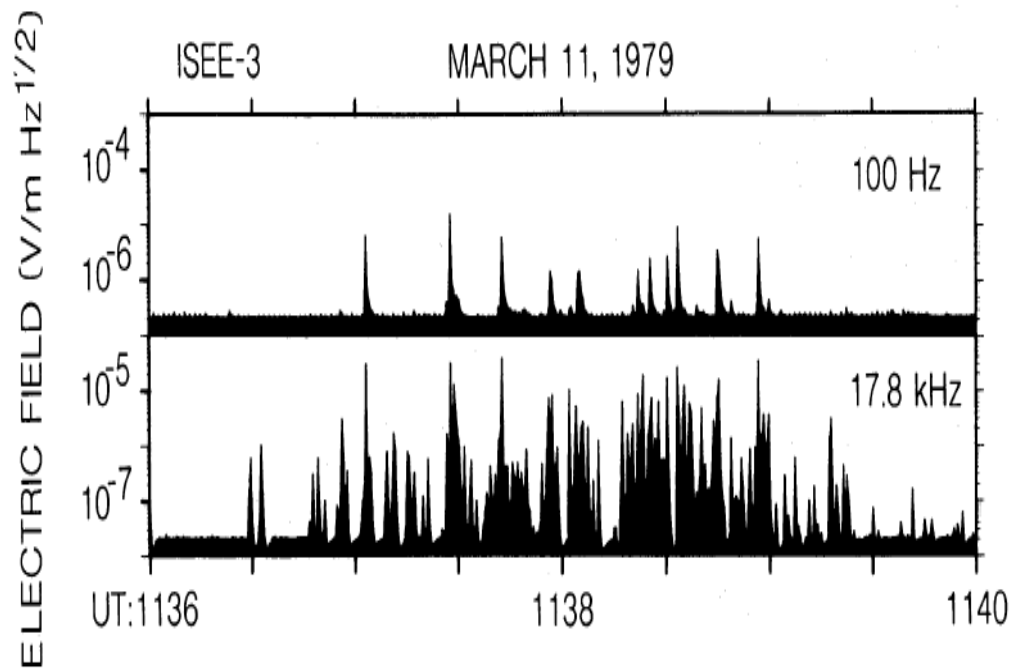
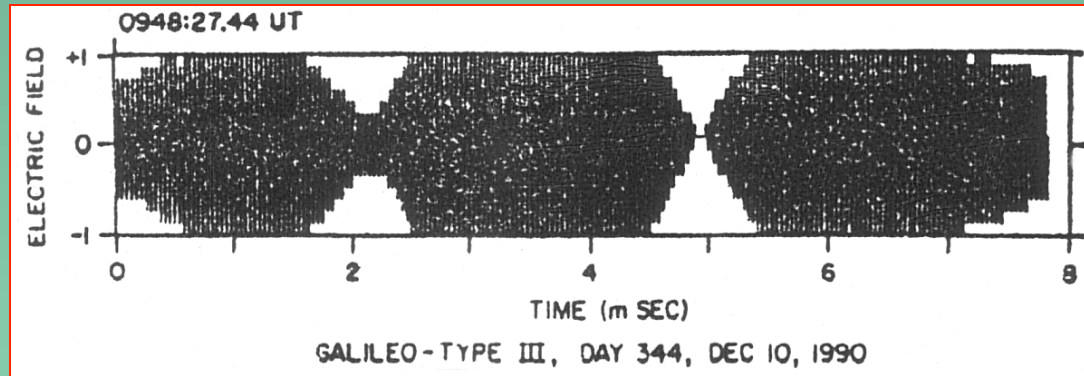
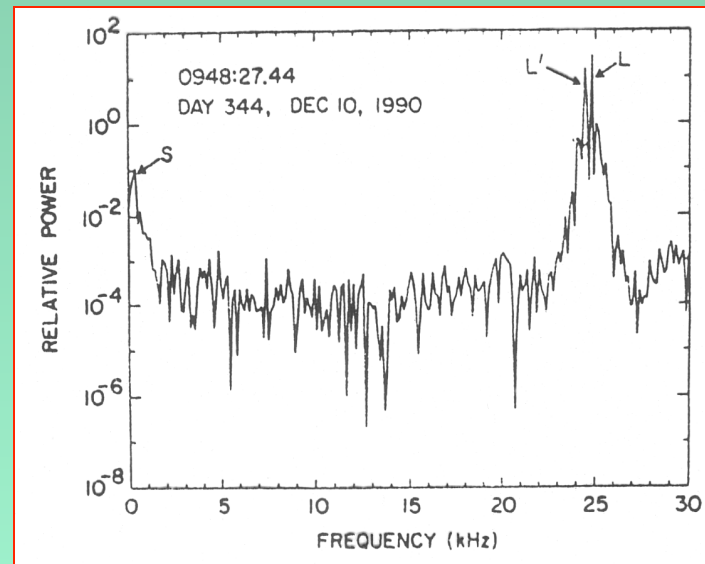


FIG. 3.—High-time resolution (0.5 s) plots of the Langmuir wave channel (17.8 kHz) and the 100 Hz long-wavelength ion acoustic wave channel for the 1979 March 11 event. Note the close correspondence between the most intense Langmuir wave spikes and the 100 Hz spikes.

Ref: Lin et al. ApJ 1986



A beat-type waveform of high-frequency oscillations near the local electron plasma frequency, at about 24 kHz in the solar wind (Gurnett et al., 1993; Hospodarsky & Gurnett, 1995).



Power Spectrum of the beat-type waveform. L is the beam-generated Langmuir wave, L' is the Langmuir wave produced by parametric decay, $L \rightarrow L' + S$, where S is the ion-acoustic wave.

Generalized Zakharov equation

(Rizzato & Chian, 1992; Alves et al., 2002)

$$\begin{aligned}(\partial_t^2 - \nu_e \partial_t + c^2 \nabla \times (\nabla \times) - \gamma_e v_{th}^2 \nabla (\nabla \cdot) + \omega_p^2) \vec{E} &= - \frac{\omega_p^2}{n_0} n \vec{E} \\ (\partial_t^2 - \nu_i \partial_t - v_s^2 \nabla^2) n &= \frac{\varepsilon_0}{2m_i} \nabla^2 \langle \vec{E}^2 \rangle\end{aligned}$$

\vec{E} : high - frequency electrostatic and electromagnetic fields

n : low - frequency ion density fluctuations

Three-wave couplings:

$$L \rightarrow L + S \quad (\text{Chian \& Abalde, 1995})$$

$$L \rightarrow T + S \quad (\text{Chian \& Abalde, 1995})$$

Four-wave couplings:

$$L \rightarrow L^- + L^+ + S \quad (\text{Chian \& Abalde, 1996})$$

$$L \rightarrow L^+ + T^- + S \quad (\text{Akimoto, 1988; Barta \& Karlicky, 2000})$$

$$L \rightarrow L^- + T^+ + S \quad (\text{Abalde, Alves \& Chian, 1998; Barta \& Karlicky, 2000})$$

Twelve-wave couplings: (Rizzato & Chian, 1992; Alves et al. 2002)

One-pump hybrid parametric instability

A traveling Langmuir pump wave $\mathbf{E}_0(\omega_0, \mathbf{k}_0)$ with dispersion relation $\omega_0^2 = \omega_p^2 + \gamma_e v_{th}^2 k_0^2$ can excite two types of four-wave hybrid modulational instabilities (Akimoto 1988; Chian & Abalde 1997): $L_0 \rightarrow T^+ + L^- + S$ and $L_0 \rightarrow T^- + L^+ + S$, respectively, provided the following frequency and wave-vector matching conditions are fulfilled

$$\omega_{\alpha}^{-} \approx \omega_0 - \omega^*, \quad \omega_{\alpha}^{+} \approx \omega_0 + \omega, \quad \mathbf{k}_{\alpha}^{\mp} = \mathbf{k}_0 \mp \mathbf{k}, \quad (3)$$

where ω and \mathbf{k} are the frequency and wave vector of the low-frequency ion mode, respectively, $\alpha = T$ or L , with $|\mathbf{k}_{T}^{\mp}| \ll (|\mathbf{k}_0|, |\mathbf{k}_{L}^{\mp}|)$ and $|\mathbf{k}| \approx |\mathbf{k}_0|$, the asterisk denotes the complex conjugate. The wave-vector kinematics for $L_0 \rightarrow T^+ + L^- + S$ is illustrated in Fig. 1. In this paper, we shall focus on the process

Wave-vector kinematics for 4-wave interactions

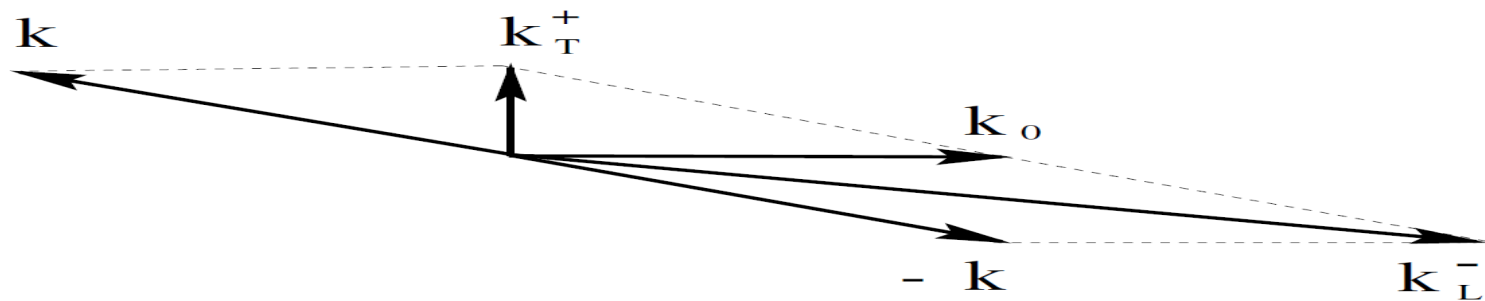


Fig. 1. Geometry of wave-vector matching conditions for the hybrid modulational instability $L_0 \rightarrow T^+ + L^- + S$

Nonlinear dispersion relation for one-pump hybrid parametric instability

The nonlinear dispersion relation for the hybrid modulational instability $L_0 \rightarrow T^+ + L^- + S$ can be derived from a Fourier analysis of Eqs. (1) and (2), making use of the phase-matching conditions (3), which yields

$$D_S(\omega, \mathbf{k}) = \Lambda[1/D_T^+(\omega^+, \mathbf{k}_T^+) + 1/D_L^-(\omega^-, \mathbf{k}_L^-)], \quad (4)$$

where $\Lambda = e^2 k_S^2 |\mathbf{E}_0|^2 / (m_e m_i)$, $D_S(\omega, \mathbf{k}) = \omega^2 + i\nu_S \omega - v_S^2 k^2$, $D_T^+(\omega^+, \mathbf{k}_T^+) = (\omega_0 + \omega)^2 + i\nu_T(\omega_0 + \omega) - c^2(\mathbf{k}_0 + \mathbf{k})^2 - \omega_p^2$, and $D_L^-(\omega^-, \mathbf{k}_L^-) = (\omega_0 - \omega^*)^2 + i\nu_L(\omega_0 - \omega^*) - \gamma_e v_{th}^2 (\mathbf{k}_0 - \mathbf{k})^2 - \omega_p^2$. We assume \mathbf{k}_T perpendicular to \mathbf{k}_0 . Making the resonant approximation for the high-frequency electromagnetic and Langmuir waves, Eq. (4) becomes

$$\omega^2 + i2\nu_S \omega - \mu\tau k_0^2 = \frac{\mu\tau k_0^2 W_0}{4} \times \left[\frac{1}{\omega + \frac{3}{2}k_0^2 - \frac{1}{2}(c/v_{th})^2 k_T^2 + i\nu_T} - \frac{1}{\omega - \frac{9}{2}k_0^2 + i\nu_L} \right], \quad (5)$$

where $\mu = m_e/m_i$, $\tau = (\gamma_e T_e + \gamma_i T_i)/T_e$, $W_0 = \epsilon_0 |\mathcal{E}_0|^2 / (2n_0 K T_e)$ is a dimensionless parameter that measures the energy density of the Langmuir pump wave, $\mathbf{E}_0 = 1/2 \mathcal{E}_0 \exp i(\mathbf{k}_0 \cdot \mathbf{r} - \omega_0 t) + c.c.$, $\lambda_D = [\epsilon_0 K T_e / (n_0 e^2)]^{1/2}$ is the Debye length and we have introduced the normalizations $\omega/\omega_p \rightarrow \omega$ and $\mathbf{k}\lambda_D \rightarrow \mathbf{k}$.

Growth rate of one-pump hybrid parametric instability

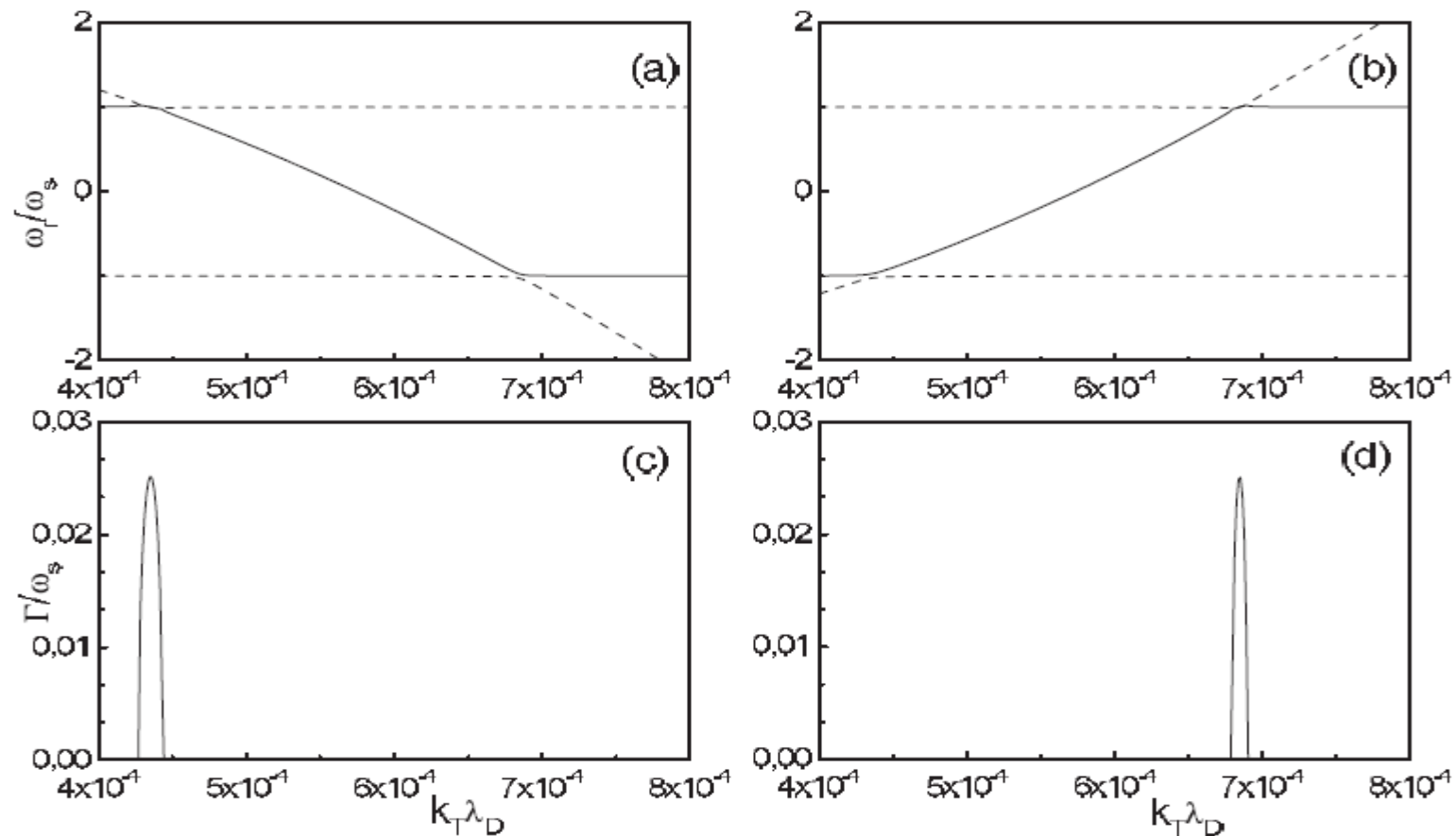


Fig. 7. Numerical solutions for one-pump models within the limit $k_0 > (2/3) (\mu\tau)^{1/2}$; **a)** and **c)** for the Akimoto (1988) model, and **b)** and **d)** for the Abalde et al. (1998) model; **a)** and **b)** plot the real part of the solution and **c)** and **d)** the growth rate, as a function of $k_T \lambda_D$.

Wave-vector kinematics for two-pump hybrid parametric instability

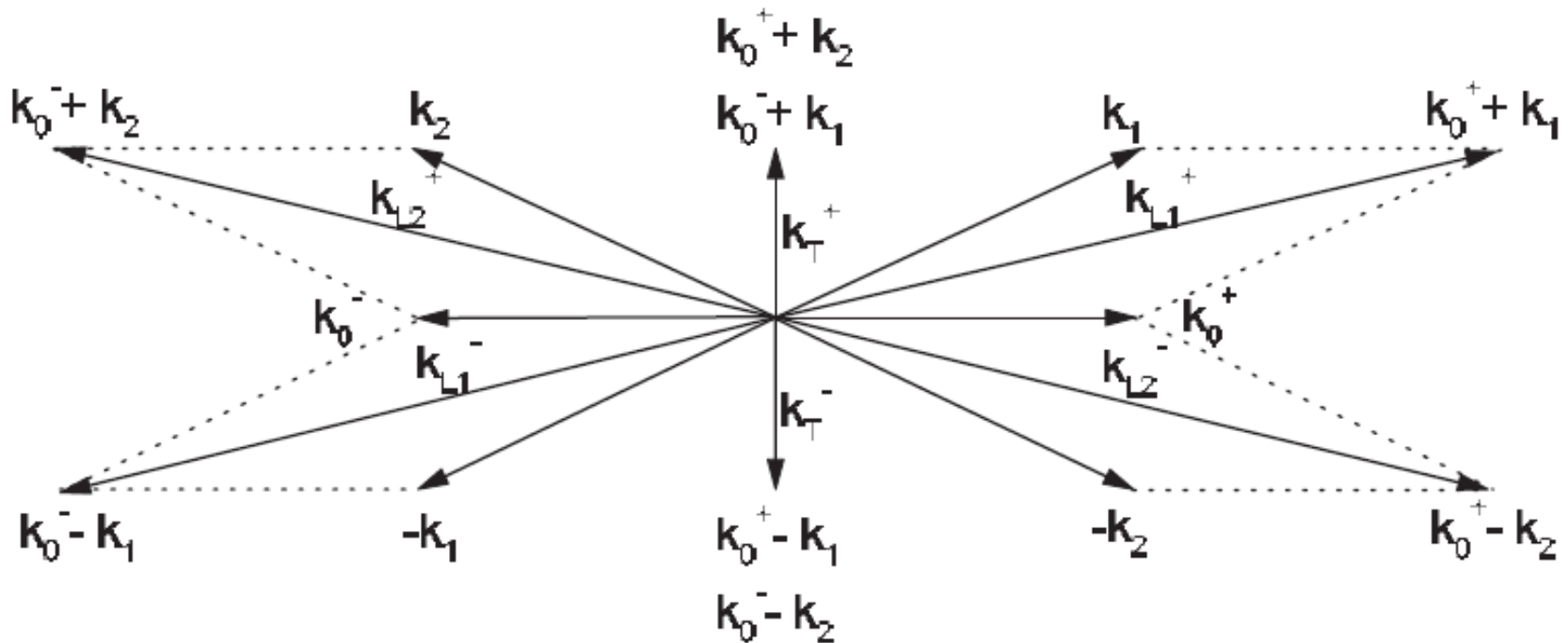


Fig. 1. Wave-vector kinematics for our model: $k_0^{+(-)}$ are related to the pump Langmuir waves, $k_{1(2)}$ to ion acoustic waves, $k_0^{+(-)} - k_{1(2)}$ are the electrostatic (oblique to $k_0^{+(-)}$) or electromagnetic (\perp to $k_0^{+(-)}$) Stokes modes and $k_0^{+(-)} + k_{1(2)}$ are the electrostatic (oblique to $k_0^{+(-)}$) or electromagnetic (\perp to $k_0^{+(-)}$) anti-Stokes modes.

Nonlinear dispersion relation for two-pump hybrid parametric instability

$$\begin{aligned}
 D_s^2 &- \frac{W_{T0}}{4\tau(\mu\tau)^{1/2}k_0} D_s \left(\frac{1}{D_L^+} - \frac{1}{D_L^-} + \frac{1}{D_T^+} - \frac{1}{D_T^-} \right) \\
 &+ \frac{W_{T0}^2}{16\mu\tau^3 k_0^2 (1+r)^2} \left[\frac{-(1-r)^2}{D_T^+ D_T^-} \right. \\
 &+ (1+r^2) \left(\frac{1}{D_T^+ D_L^+} - \frac{1}{D_L^+ D_L^-} + \frac{1}{D_T^- D_L^-} \right) \\
 &\left. - 2r \left(\frac{1}{D_L^+ D_T^-} + \frac{1}{D_T^+ D_L^-} \right) + r \left(\frac{1}{D_L^{+2}} + \frac{1}{D_L^{-2}} \right) \right] = 0
 \end{aligned}$$

Growth rate of two-pump hybrid parametric instability

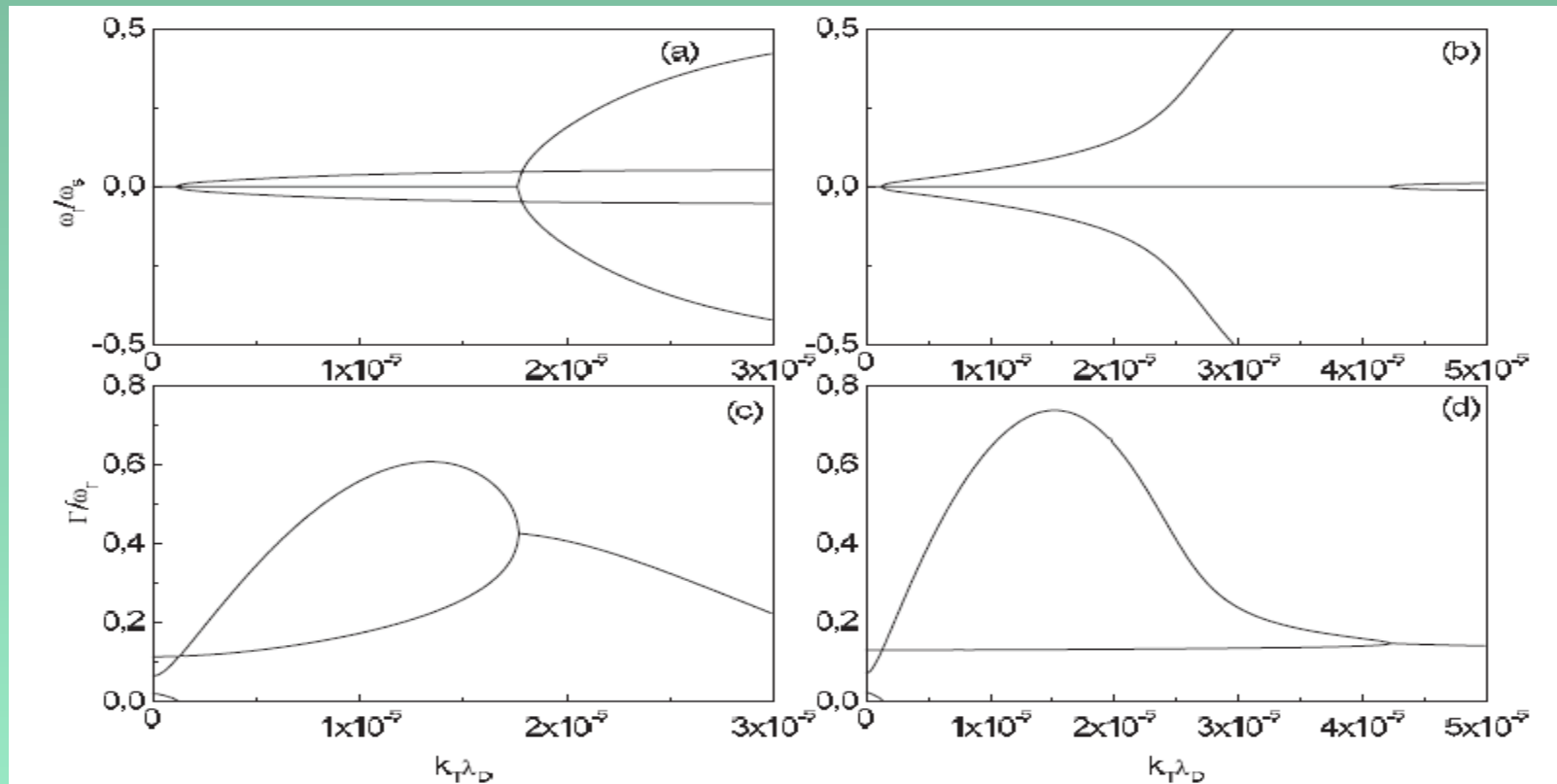
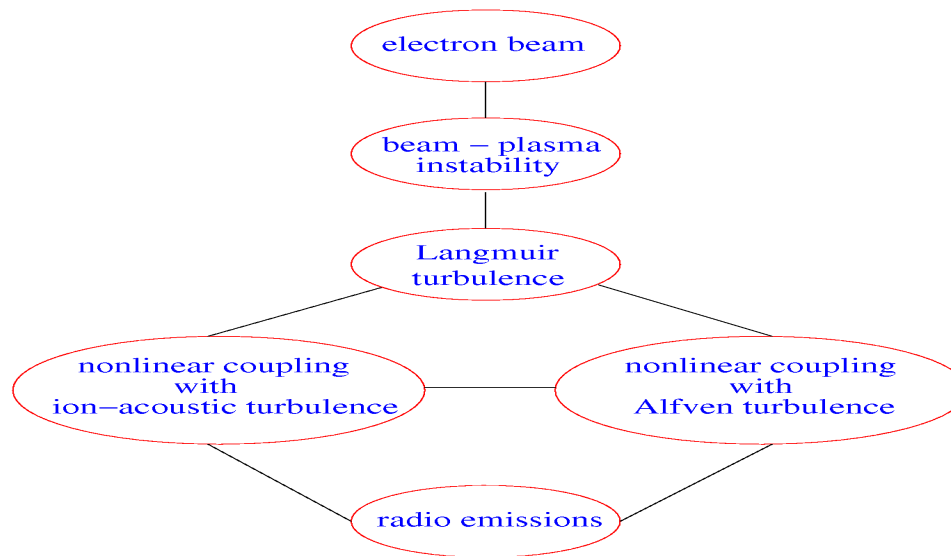


Fig. 12. Numerical solutions for the present model with different values of r ; **a)** and **b)** show the real part of the solution and **b)** and **d)** the growth rates, with $k_0 = 10^{-4}$, within the limit $k_0 < (1/3)W_0^{1/2}$; **a)** and **c)** refers to $r = 0.5$, and **b)** and **d)** to $r = 0.95$.

r : ratio of two pump amplitudes

Flow diagram for generation of radio emissions
by beam – plasma instability



Chian & Alves, ApJ Lett. 1988

Chian et al., A&A 1994

Chian et al., PSS 2000

Alves et al., A&A 2002

Voitenko et al., A&A 2003

Letter to the Editor

Generation of auroral whistler-mode radiation via nonlinear coupling of Langmuir waves and Alfvén waves

A.C.-L. Chian^{1,2,3}, S.R. Lopes^{2,3}, and M.V. Alves³

¹ Department of Physics and Mathematical Physics, University of Adelaide, SA 5005, Australia

² Department of Applied Mathematics and Theoretical Physics, University of Cambridge, Cambridge CB3 9EW, UK

³ National Institute for Space Research – INPE, P.O. Box 515, 12227-900 São José dos Campos – SP, Brazil

Received 26 May 1994 / Accepted 7 July 1994

Abstract. A novel generation mechanism of nonthermal electromagnetic radiation near the electron plasma frequency by Langmuir waves in space and astrophysical plasmas is proposed. It is shown that large-amplitude Langmuir waves may nonlinearly interact with Alfvén waves to generate electromagnetic waves. This radiation mechanism may explain the excitation of whistler-mode emission in the Earth's and Jupiter's auroral acceleration regions where the electron plasma frequency is smaller than the electron cyclotron frequency. Observational evidence in support of the proposed emission mechanism is discussed.

Key words: plasmas–instabilities–radiation mechanisms: misc.– Earth–Planets and satellites: general

it becomes quasi-electrostatic and reduces to the lower-hybrid mode. Auroral whistler-mode hiss propagates both downward and upward along the Earth's magnetic field lines. At low altitudes, less than 1000 km, the radiation usually travels downward and is correlated with downgoing 100 eV to 10 keV electron beams. At high altitudes, more than 10,000 km, the radiation usually travels upward and is correlated with upgoing ~ 50 eV electron beams. At intermediate altitudes, propagation at both directions occur. The bursts of short duration upgoing low-altitude auroral whistler waves are sometimes called saucers (Gurnett & Frank 1972). High-frequency leaked AKR (Auroral Kilometric Radiation) in the whistler mode has been detected by satellite, rocket and ground receivers (Miyaoka & Oya 1984; Morioka & Oya 1985; Oya et al. 1985; Benson & Wong 1987; Benson et al. 1988); it may provide the

Nonlinear excitation of kinetic Alfvén waves and whistler waves by electron beam-driven Langmuir waves in the solar corona

Yu. Voitenko^{1,2}, M. Goossens¹, O. Sirenko¹, and A. C.-L. Chian^{3,4}

¹ Centre for Plasma Astrophysics, K.U. Leuven, Celestijnenlaan 200B, 3001 Heverlee, Belgium

² Main Astronomical Observatory, National Academy of Sciences of Ukraine, 27 Akademika Zabolotnoho St., 03680 Kyiv, Ukraine

³ National Institute for Space Research – INPE, PO Box 515, 12201-970 Sao Jose dos Campos-SP, Brazil

⁴ World Institute for Space Research – WISER, University of Adelaide, SA 5005, Australia

Received 15 May 2003 / Accepted 16 July 2003

Abstract. We study a new nonlinear excitation mechanism of kinetic Alfvén waves (KAWs) and whistler waves (Ws) by electron beam-driven Langmuir waves (Ls). The generation conditions for the parametric decay instability $L \rightleftharpoons W + \text{KAW}$ are determined and the growth rate is calculated. We show that the resonant pairs of KAWs and whistler waves are nonlinearly coupled to the pump Langmuir waves and their amplitudes undergo exponential growth from the thermal level. The perpendicular dispersion of KAWs strongly increases the coupling due to the nonlinear current parallel to the ambient magnetic field. Our study suggests that the nonlinear coupling of Langmuir wave energy into KAWs and whistlers can provide an efficient sink for weakly dispersive Langmuir waves excited by fast electron beams in the solar corona when the electron plasma frequency is lower than the electron gyrofrequency. This condition can be satisfied in the low-density magnetic filaments that are rooted in the depleted patches at the coronal base and extend to the high corona. At the same time, the Langmuir-driven KAWs and whistlers give rise to scattering and/or thin structures of radio emission penetrating through, or generated in these regions. Since the decay into sunward propagating KAWs is strongest, the nonlinearly driven KAWs can be easily distinguished from the waves generated at the coronal base and propagating away from the Sun. Our results may be used in the analysis of solar radio data and for remote probing of the coronal plasma, magnetic fields, and waves.

Key words. Sun: corona – waves – instabilities

Auroral LAW (Langmuir-whistler-Alfvén) events

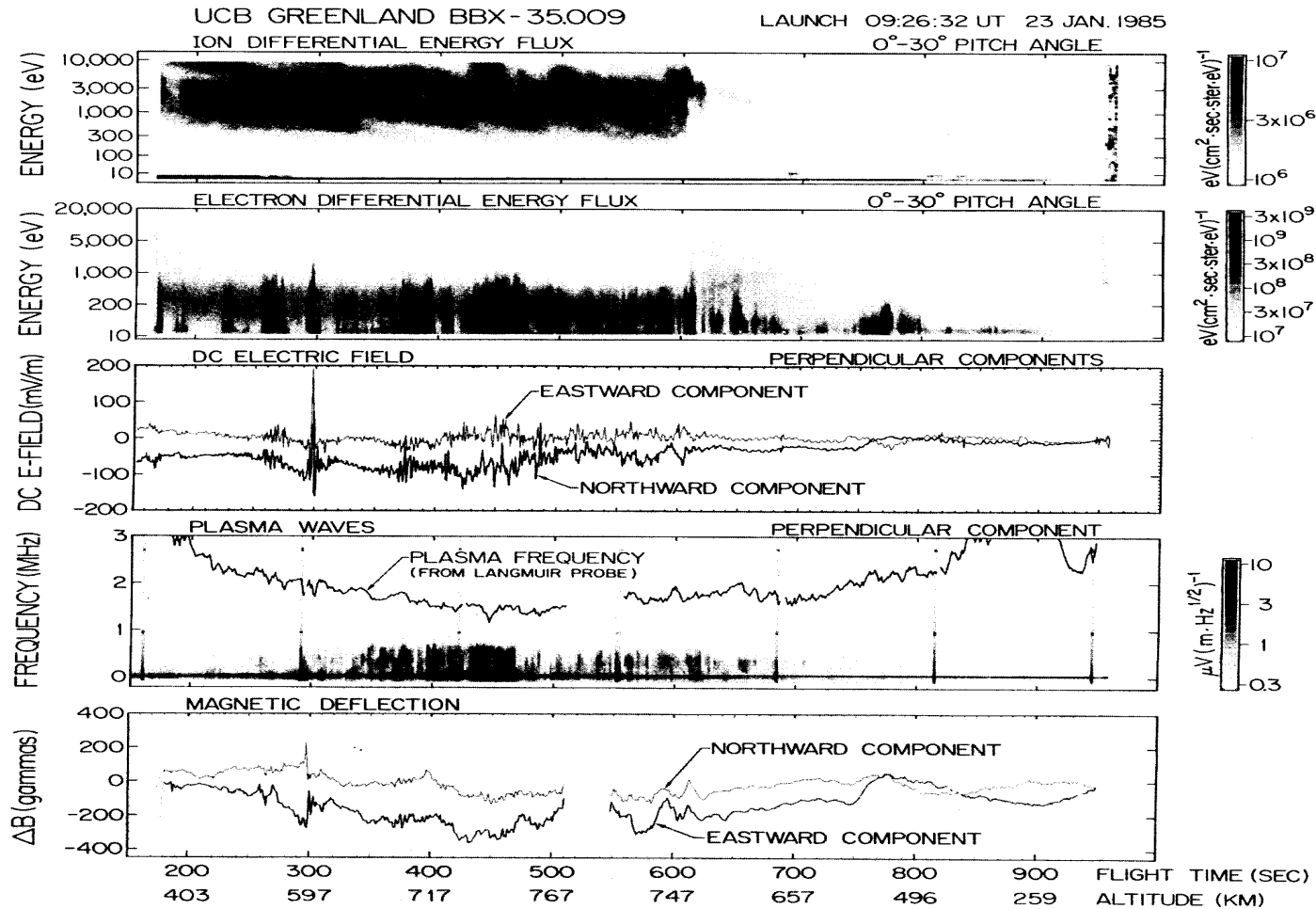


Fig. 4. A flight summary for the Greenland 1985 flight. Individual panels correspond to those in Figure 1, except that the ions are field-aligned here and the plasma wave intensity is for the component perpendicular to \mathbf{B} rather than for the parallel one. There were no large-scale potential structures, and the dispersion of the ions is characteristic of injection events in the cusp.

Ref.: Boehm et al., JGR 1990

*Examples of generation of radio waves by Langmuir waves
via nonlinear 3-wave interactions*

$$L \rightleftharpoons T + S,$$

$$L \rightleftharpoons l + W,$$

$$L \rightleftharpoons W + A,$$

$$L \rightleftharpoons W + KAW$$



PERGAMON

Planetary and Space Science 48 (2000) 9–21

**Planetary
and
Space Science**

Chaotic dynamics of nonthermal planetary radio emissions

Abraham C.L. Chian^{a, b, *}, Félix A. Borotto^{a, b, c}, Sergio R. Lopes^d, José R. Abalde^e

^a*CSSM, University of Adelaide, SA 5005, Australia*

^b*National Institute for Space Research — INPE, PO Box 515, 12227-010 São José dos Campos — SP, Brazil*

^c*Universidad de Concepción, Departamento de Física, Concepción, Chile*

^d*Universidade Federal do Paraná — UFPR, Departamento de Física, C. Postal 19081, 81531-990 Curitiba — PR, Brazil*

^e*Universidade do Vale do Paraíba — UNIVAP, Instituto de Pesquisas e Desenvolvimento — IP&D, Urbanova, 12224-000 São José dos Campos — SP, Brazil*

Received 3 March 1998; received in revised form 4 March 1999; accepted 15 April 1999

Abstract

A dynamical theory of nonlinear three-wave interactions involving Langmuir, whistler and Alfvén waves in the planetary magnetospheres is developed. By assuming linear growth for the Langmuir wave and linear damping for both whistler and Alfvén waves, the wave triplet is shown to evolve temporarily from order to chaos via either the period doubling route or the type-I Pomeau–Manneville intermittency route. Numerical solutions of this dynamical system are presented, showing the time series of the wave amplitude and the corresponding power spectra. The characterization of orderly and chaotic states is performed by plotting the Poincaré maps and calculating the largest Lyapunov exponent. The relevance of this theory for observation of chaos in the time series of nonthermal planetary radio emissions is discussed. © 1999 Elsevier Science Ltd. All rights reserved.

Temporal Dynamics of Three-Wave Coupling

Coupled wave equations for nonlinear three-wave interactions
(Chian et al., PSS 2000):

$$\partial_t A_1 = \nu_1 A_1 + A_2 A_3$$

$$\partial_t A_2 = \nu_2 A_2 - A_1 A_3^*$$

$$\partial_t A_3 = i\delta A_1 + \nu_3 A_3 - A_1 A_2^*$$

A_α : the complex amplitudes of the envelope wave fields

δ : the frequency mismatch parameter

ν_α : the growth/damping parameters

Bifurcation diagram

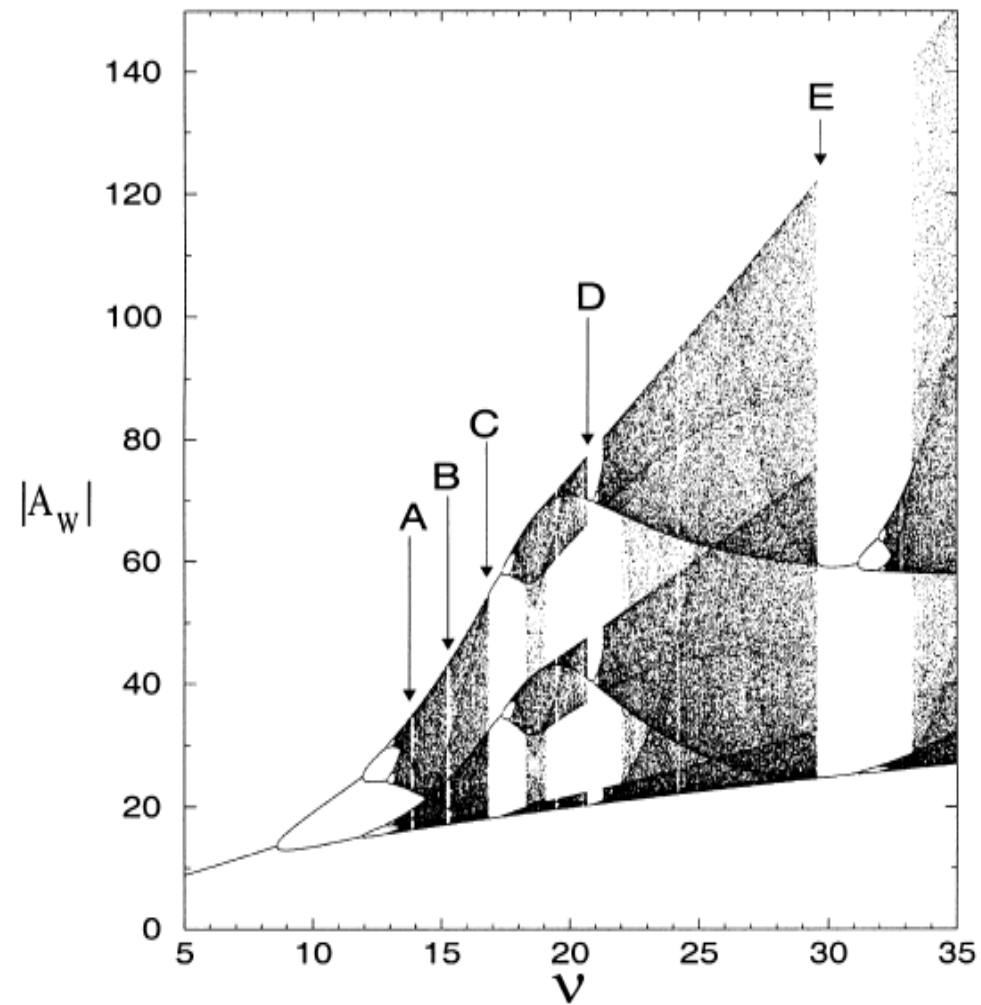


Fig. 1. Bifurcation diagram $|A_w(\nu)|$ for $\delta=2$. Type-I Pomeau-Manneville intermittency occurs at $\nu \sim 13.81$ (A), 15.21 (B), 16.82 (C), 20.64 (D) and 29.56 (E).

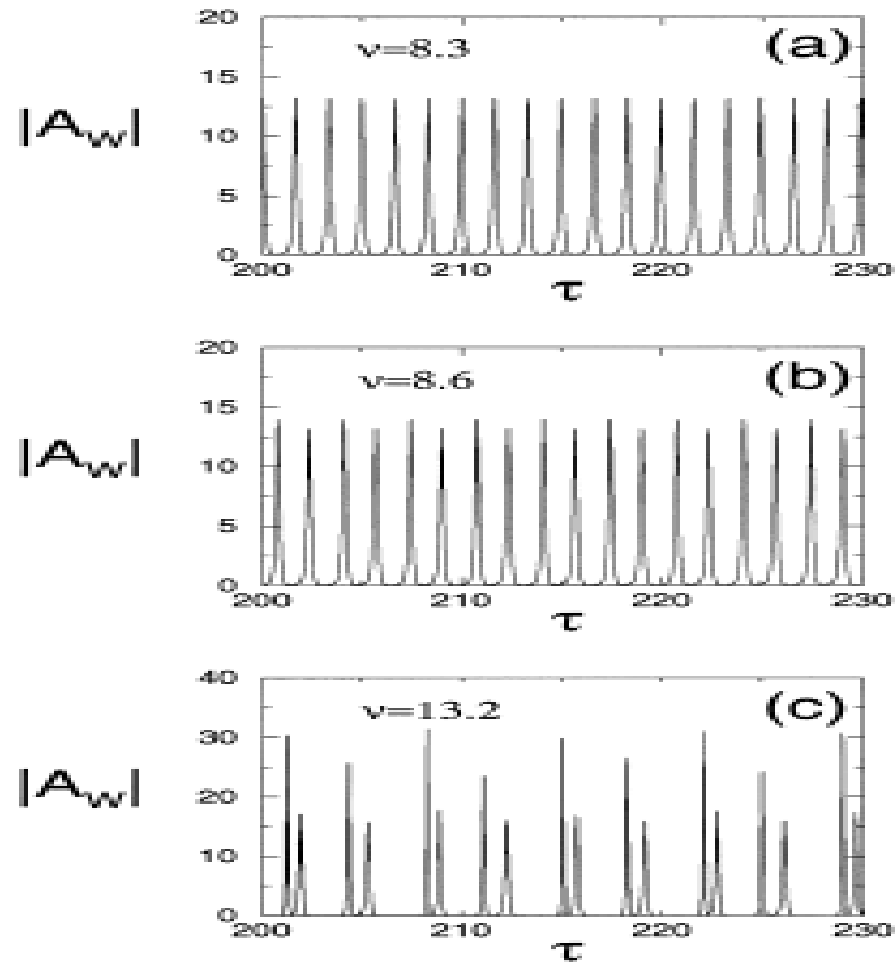


Fig. 2. Time series $|A_w(\tau)|$ of the period doubling route to chaos for $\delta=2$ and $\nu=8.3$ (a), $\nu=8.6$ (b) and $\nu=13.2$ (c).

Pomeau-Manneville intermittency & Crisis-induced intermittency

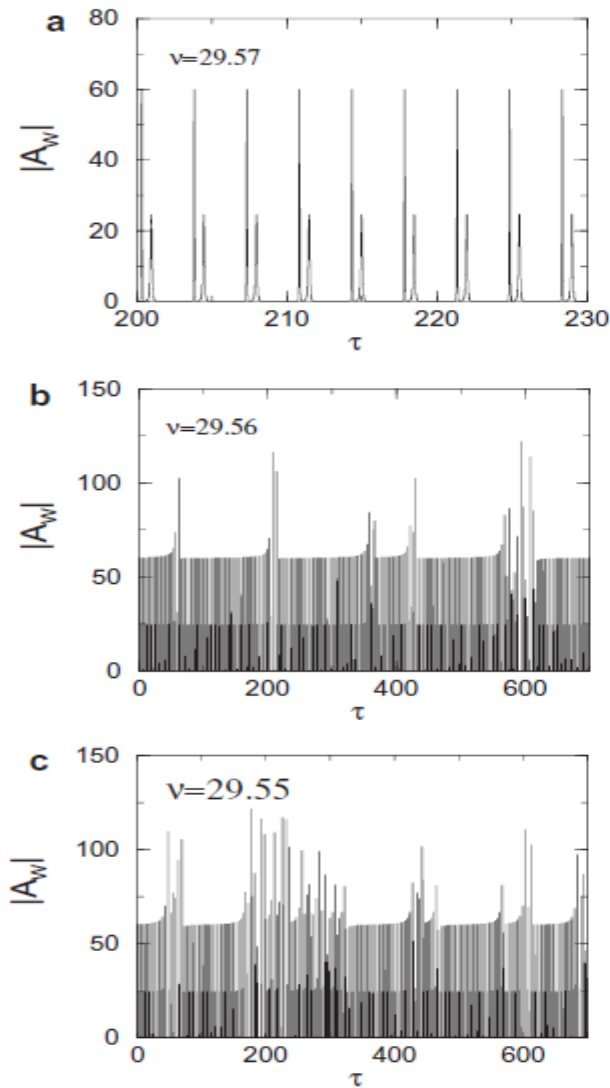


Fig. 3. Time series of $|A_w|$ as a function of τ for the type-I Pomeau–Manneville intermittency route to chaos for: (a) $\nu = 29.57$, (b) $\nu = 29.56$, and (c) $\nu = 29.55$.

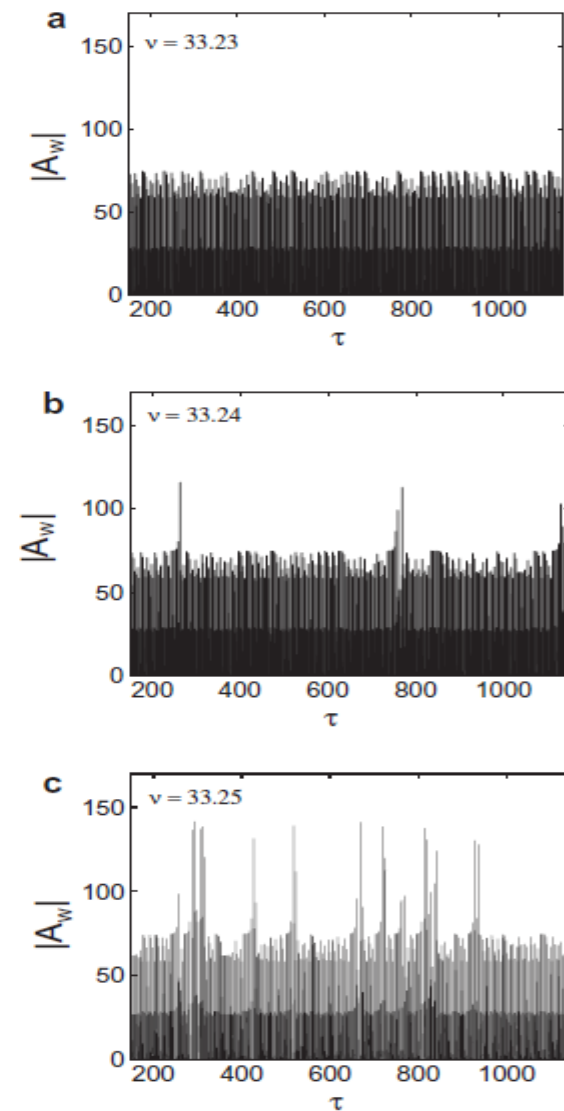
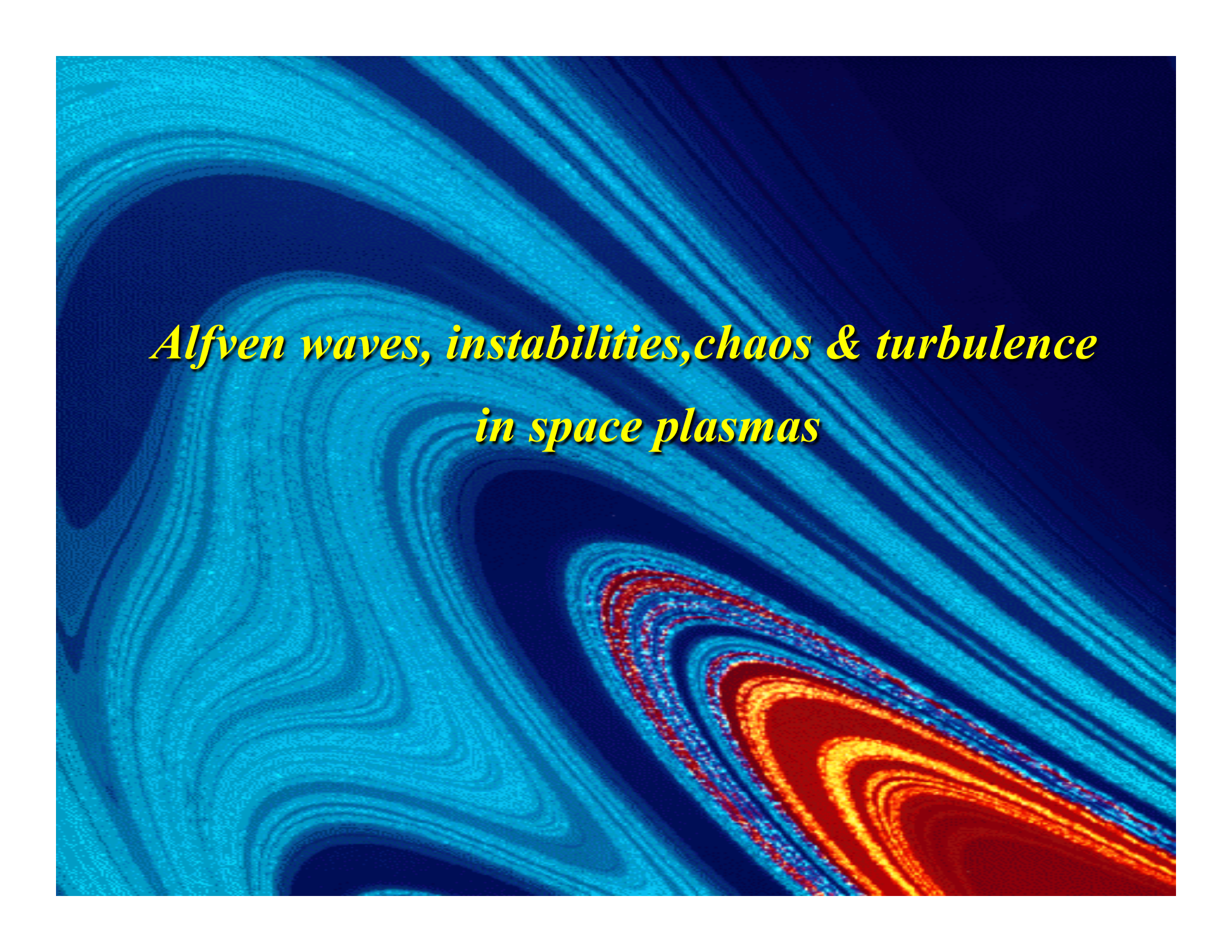


Fig. 4. Time series of $|A_w|$ as a function of τ for the crisis-induced intermittency for: (a) $\nu = 33.23$, (b) $\nu = 33.24$, and (c) $\nu = 33.25$.

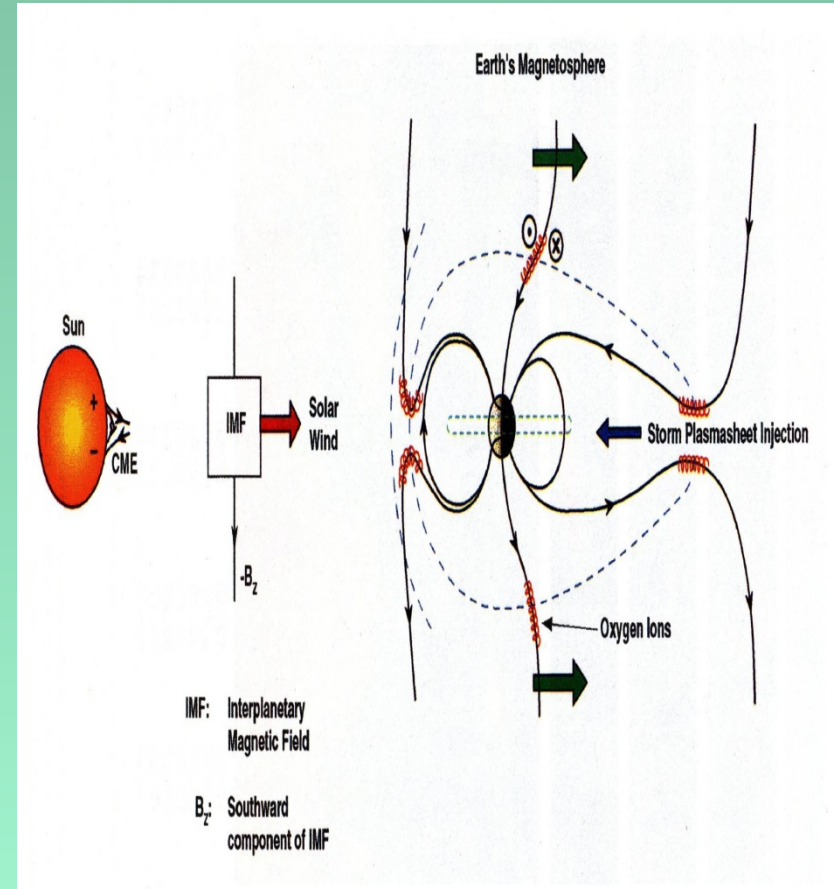
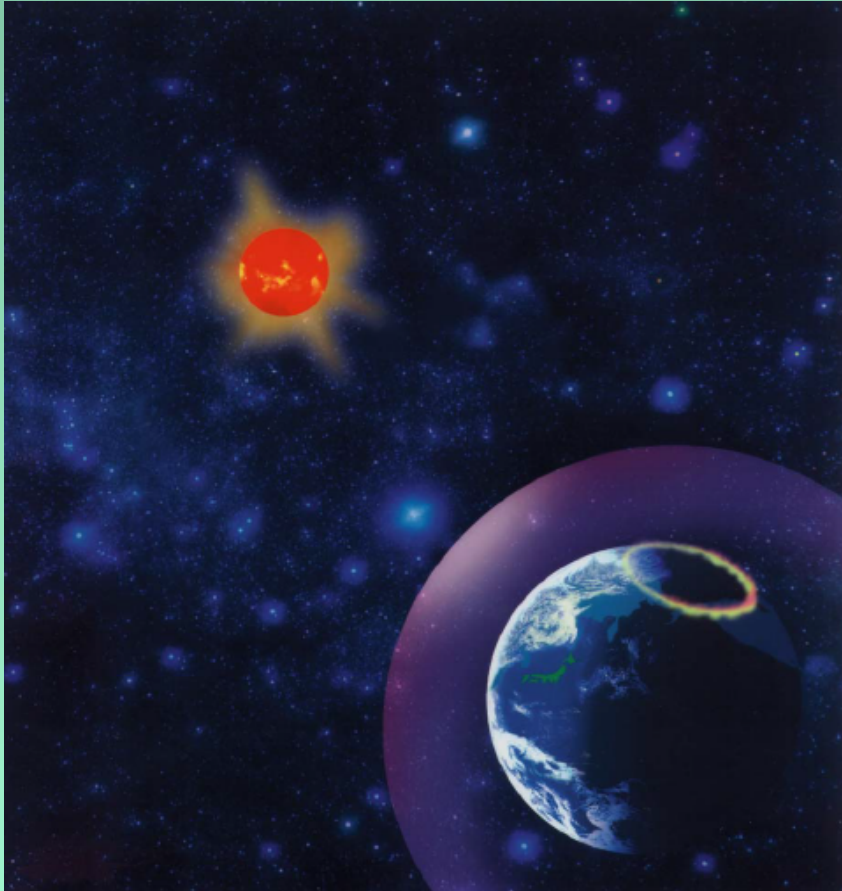
Observational evidence of chaos, complexity, fractals and nonlinearity in solar radio bursts:

- Route to chaos during a pulsation event
(Kurths et al, 1989)
- Nonlinear properties of the dynamics of bursts and flares in the solar and stellar coronae
(Isliker et al., 1994)
- Determination of fractal dimensions of solar radio bursts
(Veronig et al., 2000)
- Nonlinear statistical analysis of narrowband dm-spikes observed during the June 15, 1991 flare
(Meszarosova et al., 2000)



*Alfven waves, instabilities, chaos & turbulence
in space plasmas*

Complex dynamics of solar-terrestrial relation: Sun-Earth relation & Space weather



Gonzalez and Tsurutani, INPE/JPL

3 Solar Atmosphere

E.R. Priest

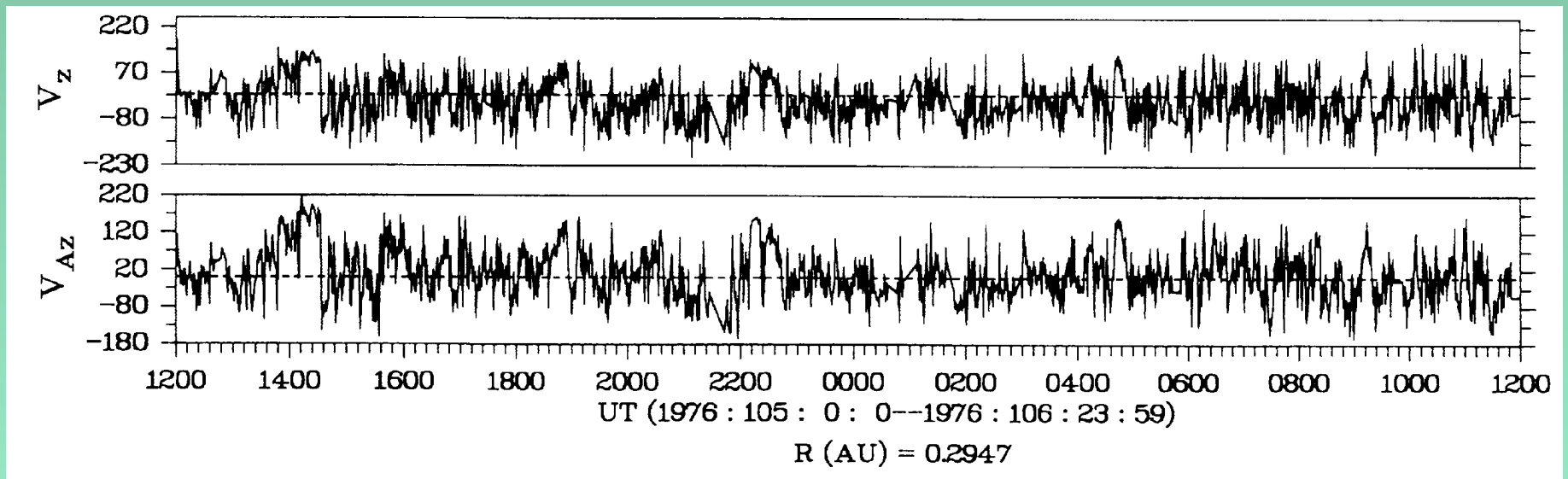
3.1	Introduction	56
3.1.1	Solar Activity	57
3.1.2	The Solar Revolution	57
3.1.3	Recent Surprises	59
3.2	The Role of the Magnetic Field	62
3.2.1	Basic Equations	62
3.2.2	Magnetic Waves	65
3.2.3	Magnetic Reconnection	66
3.3	Prominences	70
3.4	Solar Flares.....	71
3.4.1	Introduction	71
3.4.2	Energy Release by Magnetic Reconnection	73
3.4.3	Conditions for Flare Occurrence	75
3.4.4	Catastrophe and Instability Models for Eruption	76
3.5	Coronal Heating	76
3.5.1	Introduction	76
3.5.2	Numerical Experiment on Global Active Region Heating.....	80
3.5.3	Heating by MHD Waves	81
3.5.4	Heating by Magnetic Reconnection	81
3.6	Conclusion	90
	References	91

16 Ultra Low Frequency Waves in the Magnetosphere

U. Villante

16.1	Introduction	398
16.2	Linear Theory of Hydromagnetic Waves	400
16.2.1	The Uniform Field	400
16.2.2	The Dipole Field	401
16.3	Sources of Geomagnetic Pulsations	402
16.3.1	Upstream Waves	402
16.3.2	Kelvin–Helmholtz Instability	403
16.3.3	Ion-Cyclotron Instability	403
16.4	Effects of the Ionosphere and Field Line Eigenperiods	404
16.5	Field Line Resonance	405
16.6	Cavity Resonance	407
16.7	Low Frequency Pulsations	407
16.8	Mid-Frequency Pulsations	409
16.9	FLR and Magnetospheric Diagnostics	412
16.10	Cavity/Waveguide Modes	414
16.11	High Frequency Pulsations	415
16.12	Irregular Pulsations	417
16.13	Concluding Remarks	419
	References	419

ALFVÉN WAVES IN THE SOLAR WIND



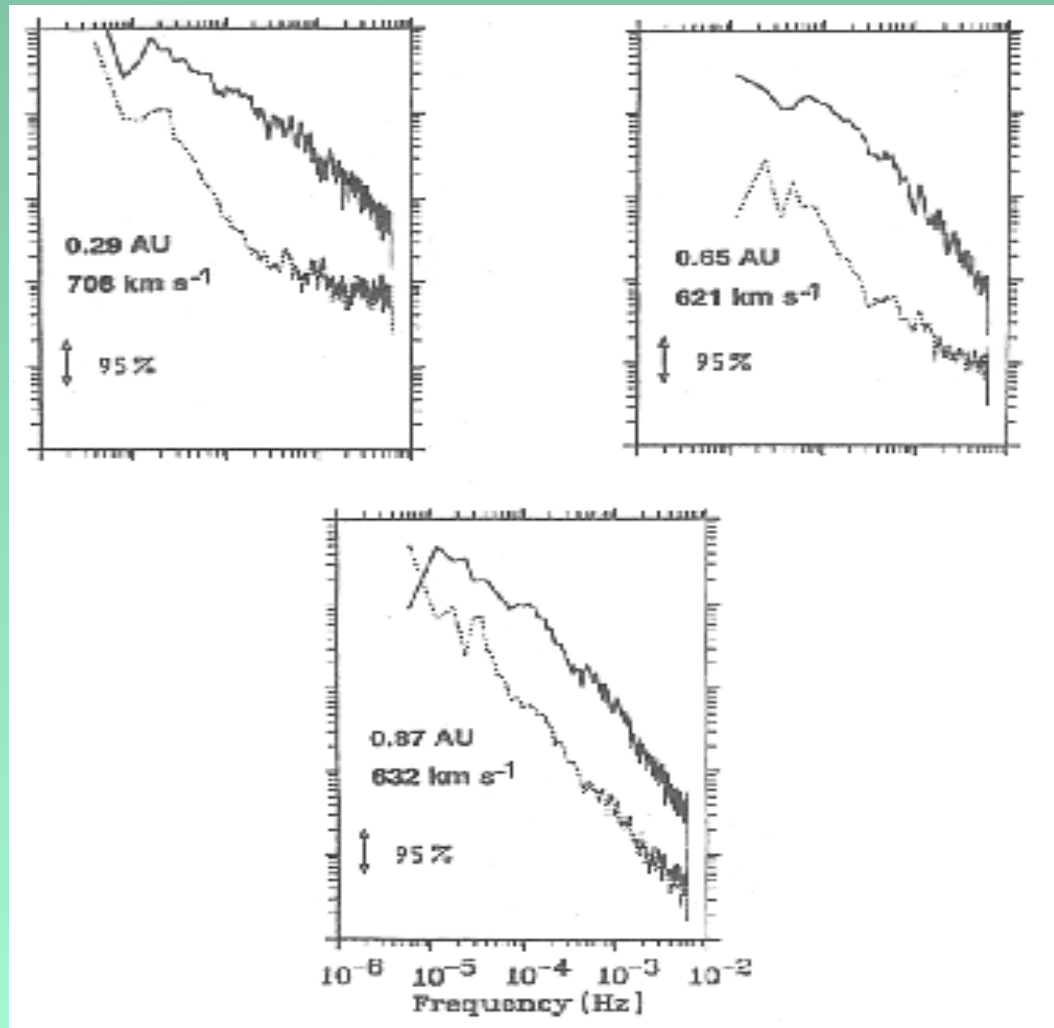
Helios (Marsch and Liu, 1993; Bruno and Carbone 2005)

$$\omega = kv_A$$

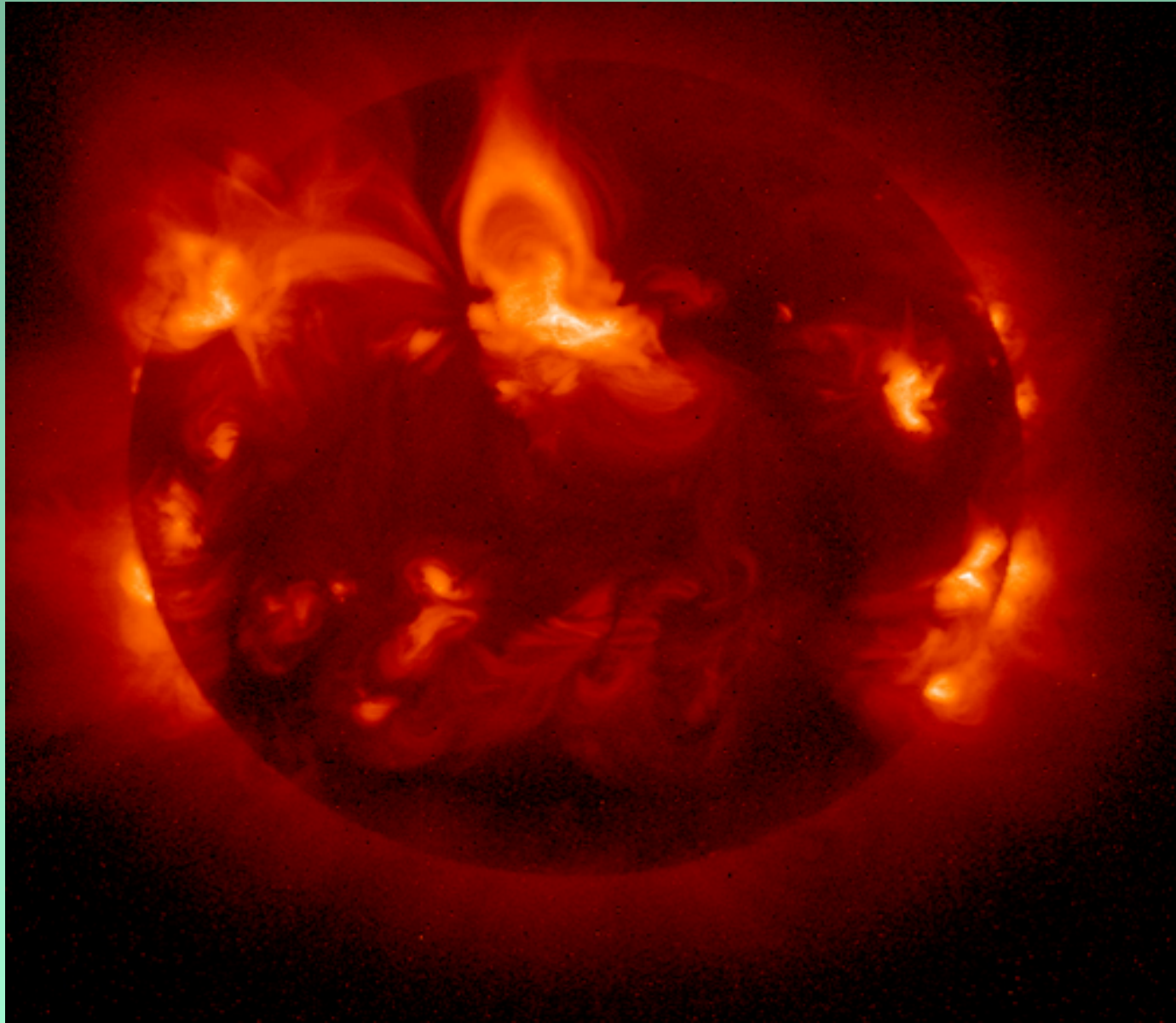
$$v_A = B_0 / (4\pi\rho_0)^{1/2}$$

Power-law behavior in the power spectrum of Alfvén intermittency in high-speed solar wind

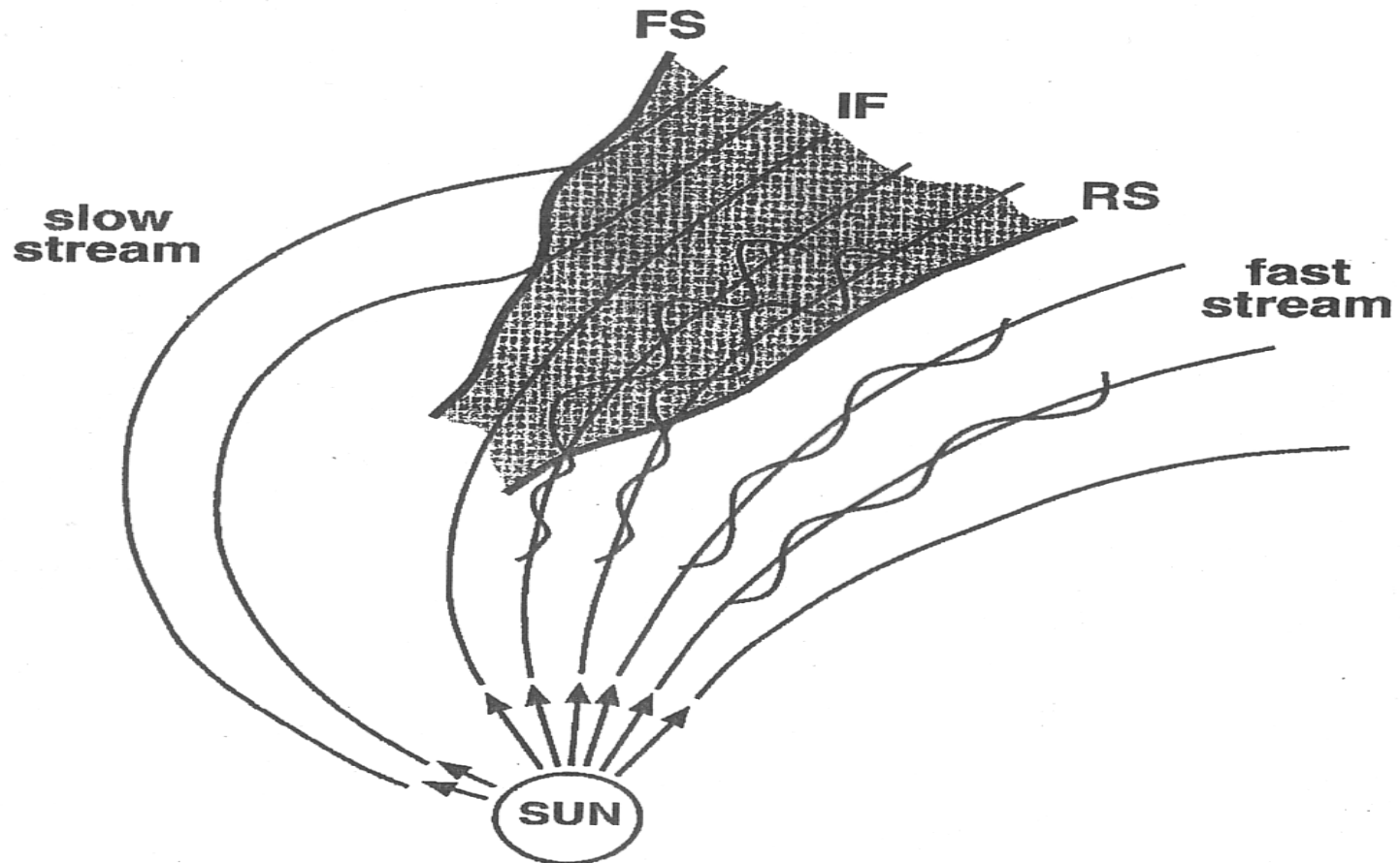
Power spectra of outward (solid lines) and inward (dotted lines) propagating Alfvénic fluctuations in high-speed solar wind, indicating power-law behavior



- Helios spacecraft (Marsch & Tu, 1990)



Corotating Interaction Region



Schematic of formation of corotating interaction regions (CIRs) during the descending phase of solar cycle. The composition of the plasma and magnetic field fluctuations are also shown. FS denotes fast shock; IF denotes interface; RS denotes reverse shock.

HILDCAAs (High-Intensity Long-Duration Continuous Auroral Activities) events: Large-amplitude Alfvén waves in the solar wind

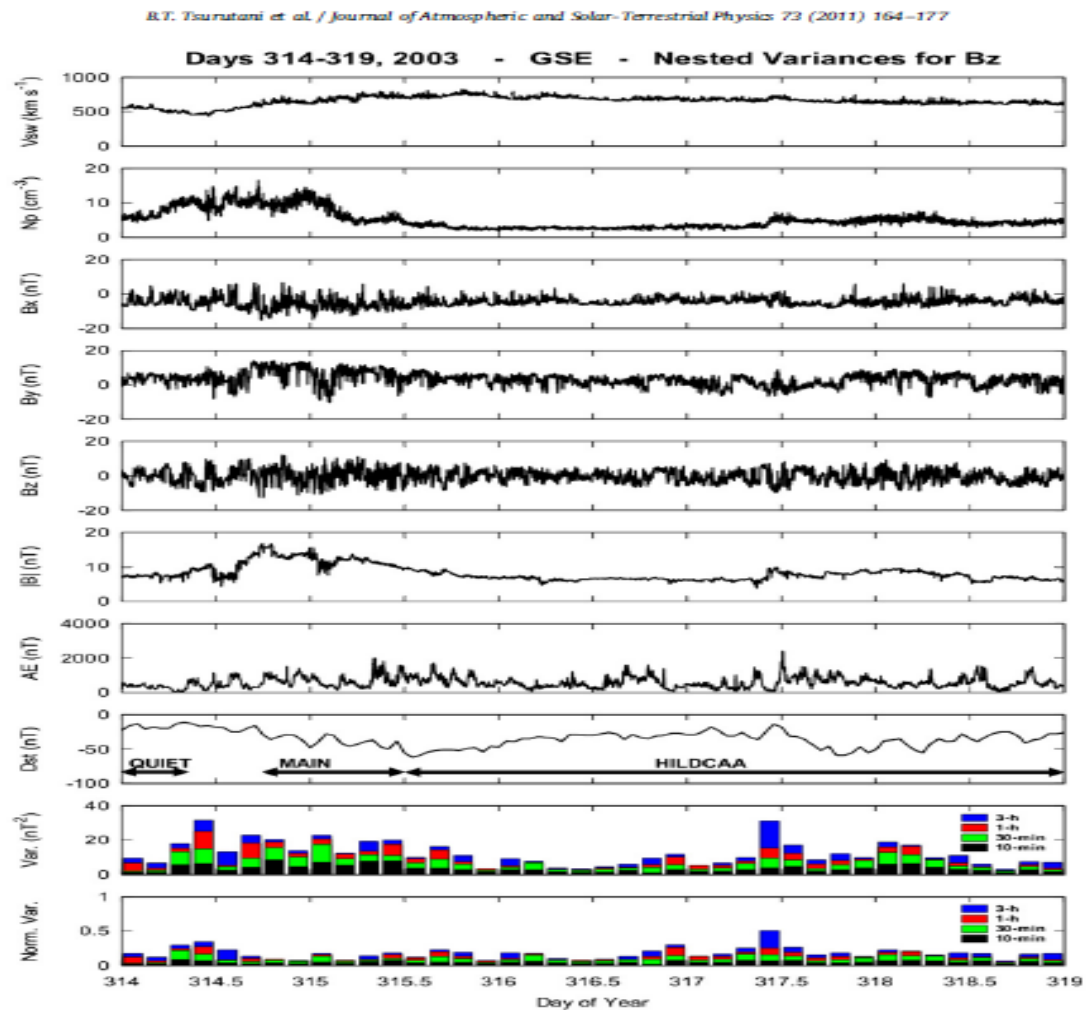


Fig. 6. Event 2, days 314–319. From top to bottom are solar wind speed and density, the 3 components of the IMF in GSE coordinates, and the AE and Dst indices. The bottom two panels are the nested 10-min, 30-min, 1-h and 3-h variances and normalized variances. All of the variances are highest during the GR. However, the normalized variances are about the same as those in the high speed stream.

Ref: Tsurutani et al. JASTP 2011

Nonlin. Processes Geophys., 14, 17–29, 2007
www.nonlin-processes-geophys.net/14/17/2007/
© Author(s) 2007. This work is licensed
under a Creative Commons License.



**Nonlinear Processes
in Geophysics**

Chaos in driven Alfvén systems: unstable periodic orbits and chaotic saddles

A. C.-L. Chian¹, W. M. Santana¹, E. L. Rempel², F. A. Borotto³, T. Hada⁴, and Y. Kamide⁵

¹National Institute for Space Research (INPE) and World Institute for Space Environment Research (WISER), P.O. Box 515, São José dos Campos – SP, CEP 12227-010, Brazil

²Institute of Aeronautical Technology (ITA), São José dos Campos – SP, CEP 12228-900, Brazil

³Universidad de Concepción, Departamento de Física, Concepción, Chile

⁴Kyushu University, Department of Earth Sciences and Technology, Fukuoka 8168580, Japan

⁵Solar-Terrestrial Environment Laboratory, Nagoya University, Toyokawa 4428507, Japan

Derivative nonlinear Schrödinger equation

$$\partial_t b + \alpha \partial_x (|b|^2 b) + i(\mu + i\eta) \partial_x^2 b = S(x, t)$$

and $\beta = c_S^2/c_A^2$. The external forcing $S(b, x, t) = A \exp(ik\phi)$ is a monochromatic left-hand circularly polarized wave with a wave phase $\phi = x - Vt$, where V is a constant wave velocity, A is the driver amplitude, and k is the driver wave number.

Low-dimensional model of nonlinear Alfvén waves

The first integral of Eq. (1) reduces to a system of ordinary differential equations by seeking stationary wave solutions with $b = b(\phi)$, giving

$$\dot{b}_y - \nu \dot{b}_z = \frac{\partial H}{\partial b_z} + a \cos \theta, \quad (2)$$

$$\dot{b}_z + \nu \dot{b}_y = -\frac{\partial H}{\partial b_y} + a \sin \theta, \quad (3)$$

$$\dot{\theta} = \Omega, \quad (4)$$

where $H = (\mathbf{b}^2 - 1)^2/4 - (\lambda/2)(\mathbf{b} - \hat{\mathbf{y}})^2$, $\hat{\mathbf{y}}$ denotes a unit vector in the y direction, the overdot denotes derivative with respect to the phase variable $\tau = -\alpha b_0^2 \phi / \mu$, the normalized dissipation parameter $\nu = \eta / \mu$, $b \rightarrow b/b_0$ (where b_0 is a complex integration constant, for simplicity, we assume in this paper that b_0 is real), $\mathbf{b} = (b_y, b_z)$, $\theta = \Omega \phi$, $\Omega = -\mu k / \alpha b_0^2$, $a = A / \alpha b_0^2 k$, $\lambda = -1 + V / \alpha b_0^2$. We assume $\beta < 1$, hence $\alpha > 0$.

Refs: Hada et al., PF 1990; Chian et al., NPG 2007; Rempel et al. IJBC 2008

Poincaré map

To simplify the analysis of a nonlinear trajectory (orbit or flow) of a complex system, it is often convenient to reduce a flow in the state space, namely, the numerical solution of equation (2.14), to a discrete time map by the Poincaré surface of section method (Ott 1993). In this monograph, we define the Poincaré surface of section (Poincaré map) by

$$P : x(t) \rightarrow x(t + T), \quad (2.18)$$

where $T = 2\pi/\omega$ is the driver period. Figure 2.3 is an illustration of a state-space trajectory and the Poincaré map.

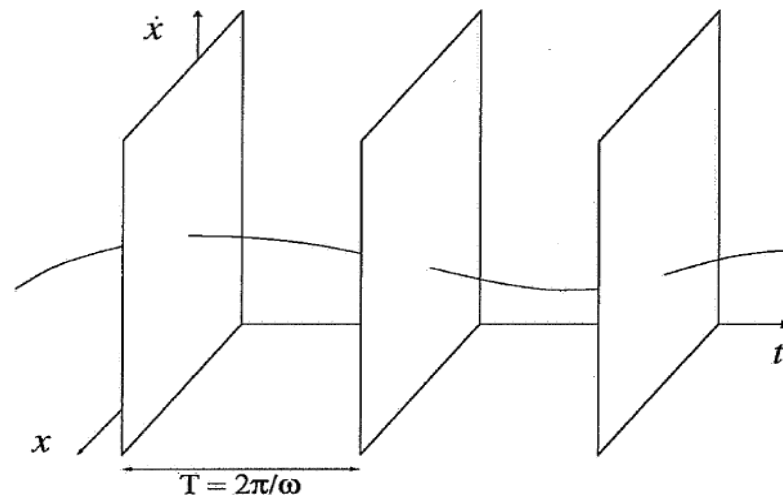
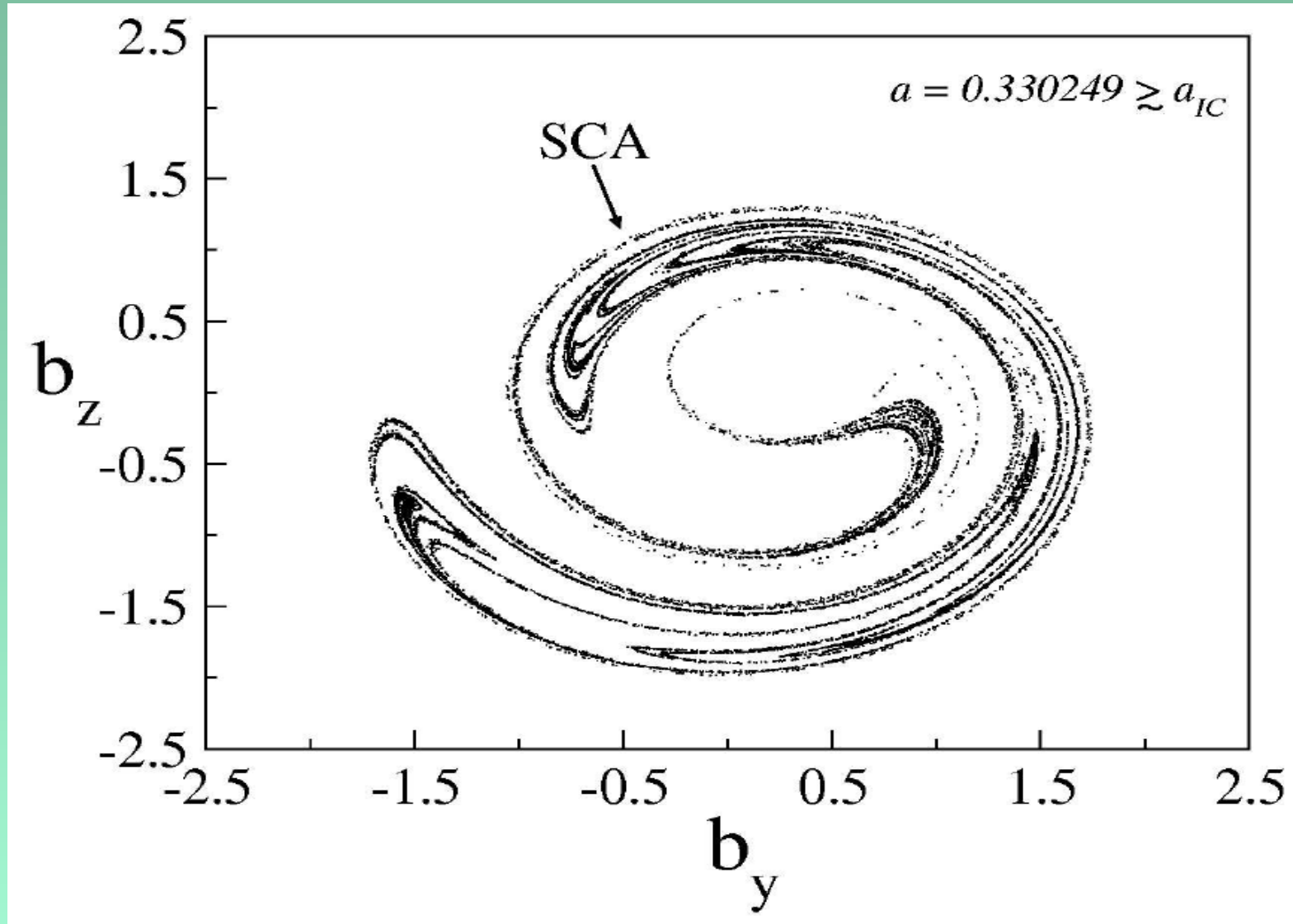


Fig. 3. State-space trajectory and Poincaré map. An illustration of a state-space trajectory and the Poincaré map, T is the driver period and ω is the driver frequency.

Chaotic attractor: Poincaré map



Bifurcation diagram & Maximum Lyapunov exponent

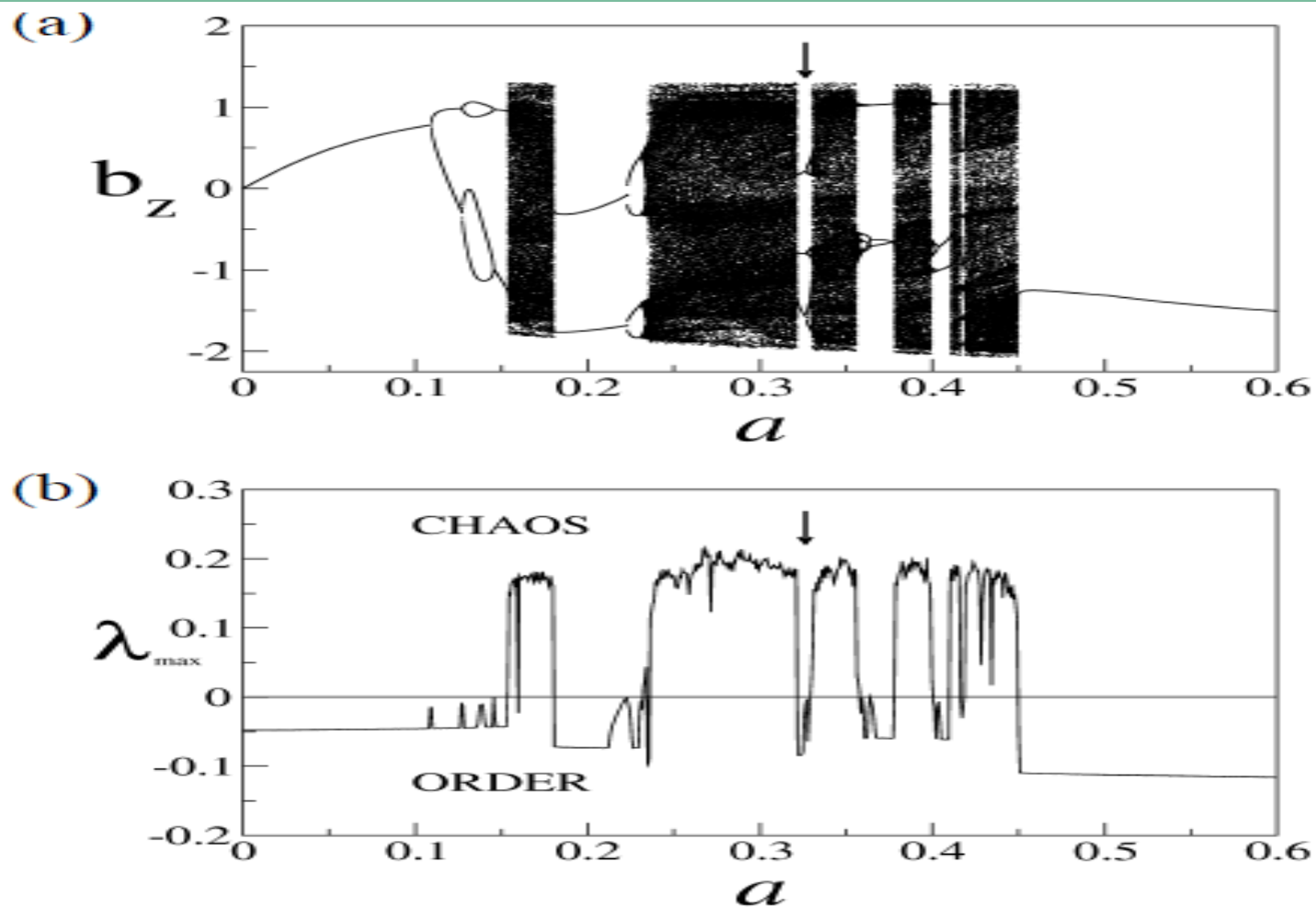


Fig. 1. Limit point diagram and maximum Lyapunov exponent: global view. (a) Limit point diagram, b_z as a function of the driver amplitude a ; (b) maximum Lyapunov exponent λ_{\max} as a function of a . The arrow indicates a period-3 periodic window. $\nu=0.02$, $\Omega=-1$, $\lambda=1/4$, $\mu=1/2$.

Periodic window: Chaotic attractors & Chaotic saddles

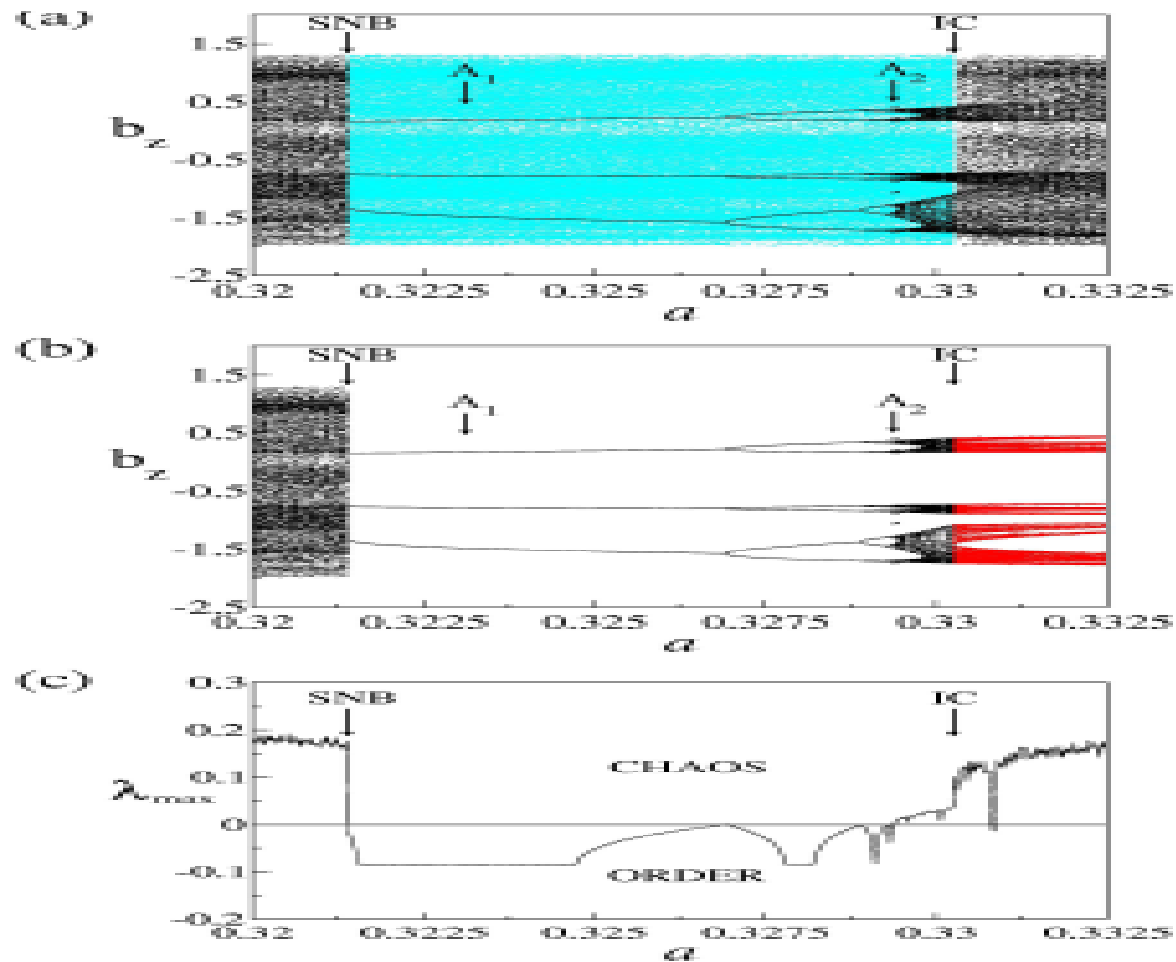


Fig. 2. Limit point diagram and maximum Lyapunov exponent: period-3 periodic window. (a) Limit point diagram, b_z as a function of the driver amplitude a , for attractors A_1 and A_2 , superimposed by the surrounding chaotic saddle (blue); (b) the same as (a), showing the conversion of the pre-crisis banded chaotic attractor (black) into the post-crisis banded chaotic saddle (red); (c) maximum Lyapunov exponent, λ_{max} as a function of a , for the attractor A_1 . SNB denotes saddle-node bifurcation, and IC denotes interior crisis.

Alfvén intermittency induced by crisis

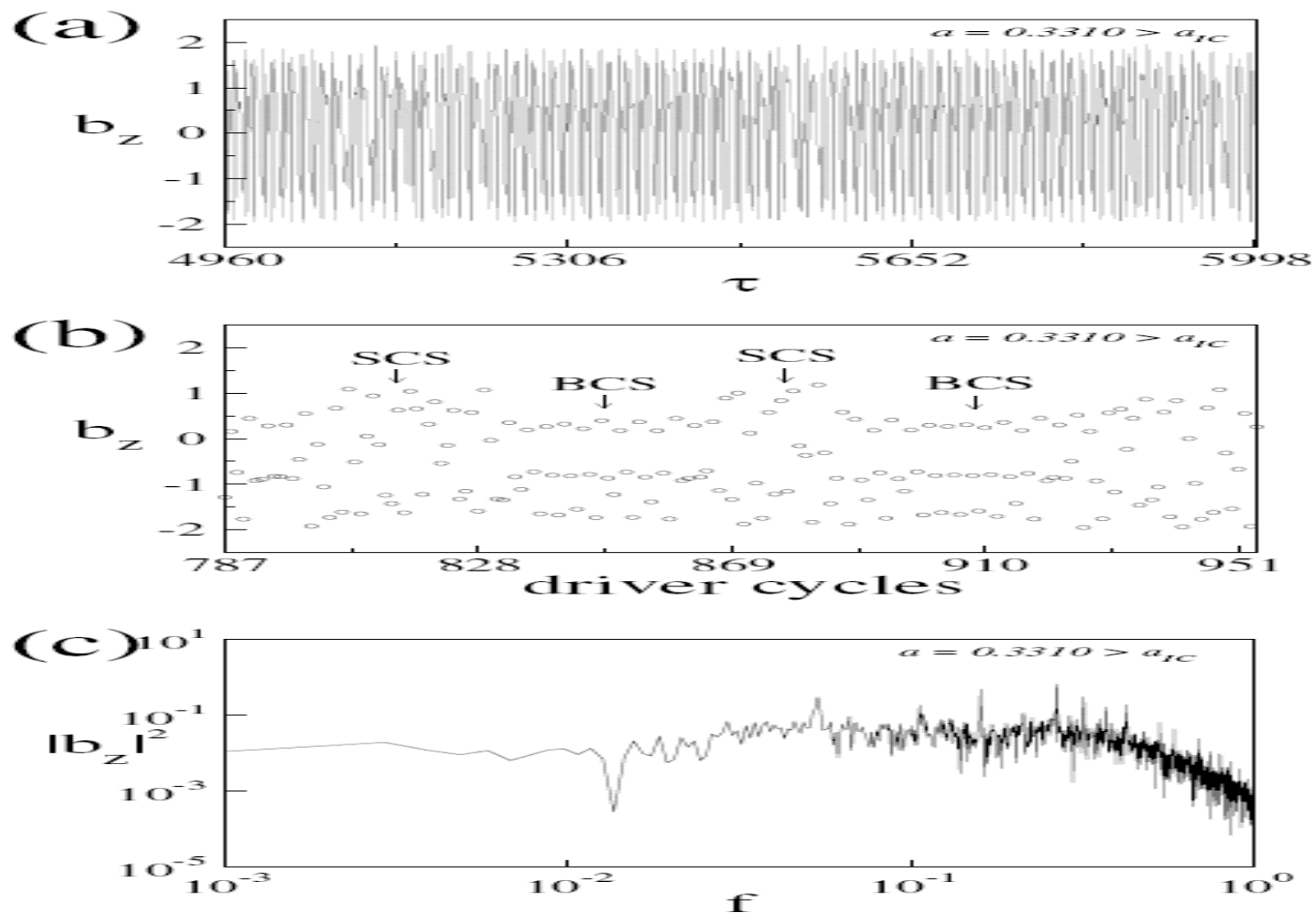
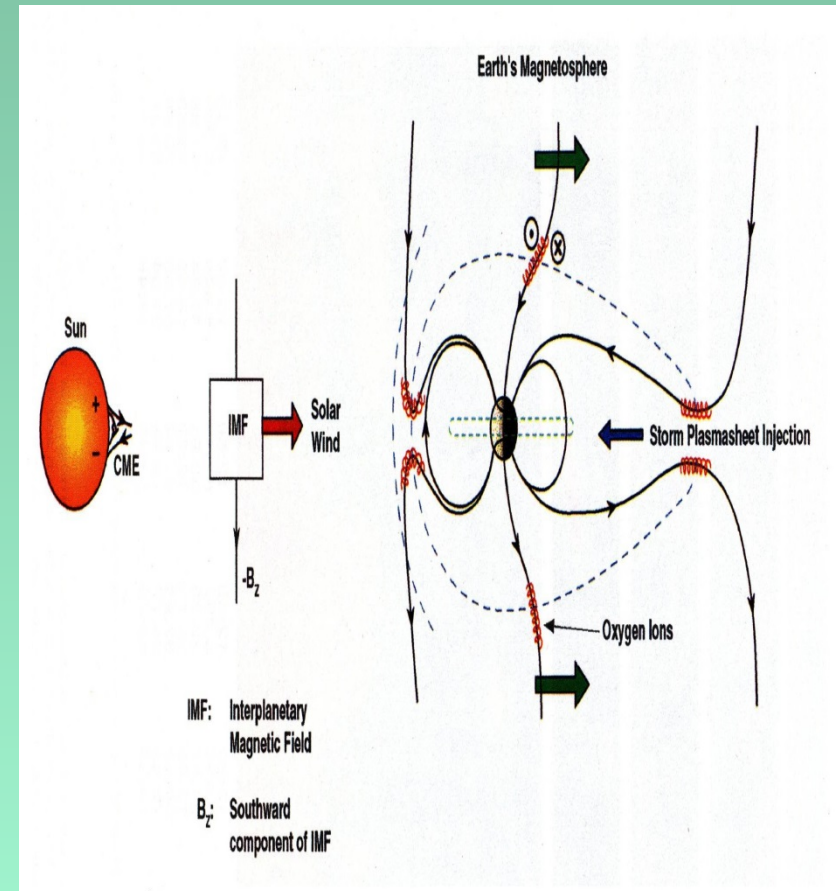
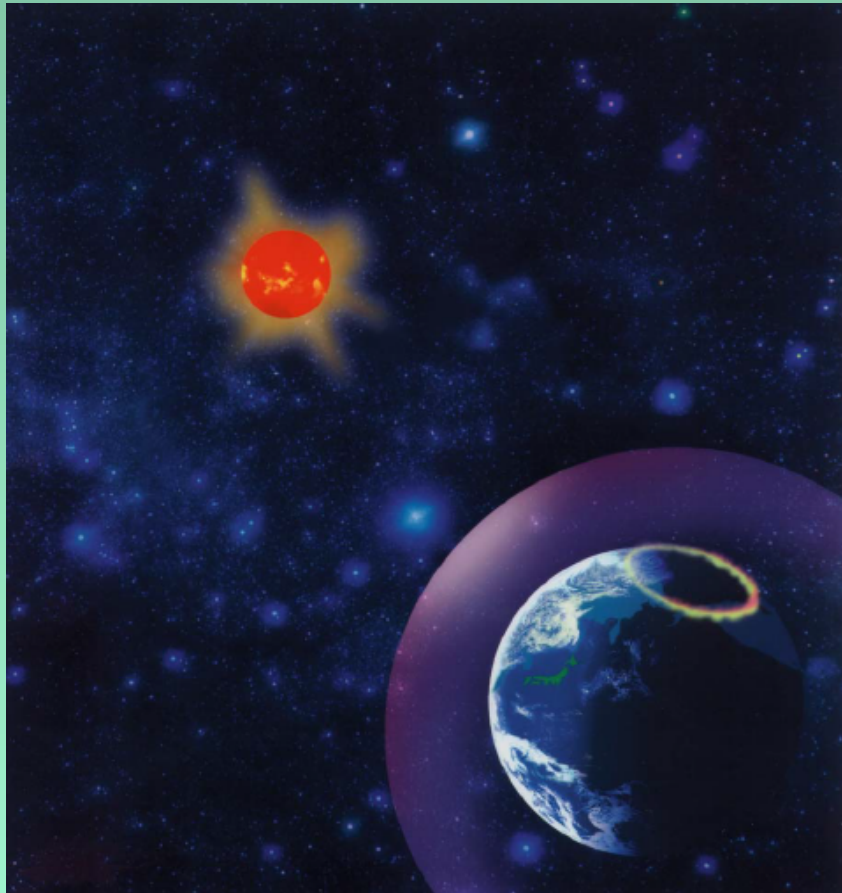


Fig. 12. Alfvén crisis-induced intermittency. (a) Time series b_z as a function of τ for $a=0.3310$, (b) same time series as (a) plotted as a function of driver cycles, (c) power spectrum of (a). SCS denotes surrounding chaotic saddle and BCS denotes banded chaotic saddle.

The image displays a complex, swirling pattern of magnetic field lines and plasma structures. The colors range from deep blue to bright red, indicating different physical properties or intensities. The structures are highly organized and show signs of reconnection and turbulence. The text is centered over the image in a yellow, italicized font.

Magnetic reconnection, coherent structures & turbulence in space plasmas

Complex dynamics of solar-terrestrial relation: Sun-Earth relation & Space weather



Gonzalez and Tsurutani, INPE/JPL

5 Coronal Mass Ejection

P.J. Cargill and L.K. Harra

5.1	Introduction	118
5.2	CMEs at the Sun	119
5.2.1	Properties	120
5.2.2	What Causes CMEs: Observational Evidence	121
5.2.3	Theoretical Ideas	125
5.3	Interplanetary Coronal Mass Ejections	128
5.3.1	Properties at 1 AU	128
5.3.2	Putting the Solar and Interplanetary Parts Together	130
5.4	Conclusions and Future Prospects	130
	References	131

11 Magnetic Reconnection

A. Nishida

11.1	Introduction	280
11.2	Reconnection on the Magnetopause	281
11.2.1	Formation and Topology of Open Field Lines	281
11.2.2	Structure of the Magnetopause in Terms of Magnetohydrodynamics ...	283
11.2.3	Direct Consequences of the Magnetopause Reconnection	289
11.3	Reconnection Inside the Magnetotail	292
11.3.1	Sites of the Magnetotail Reconnection	292
11.3.2	Structure of the Reconnection Region	294
11.3.3	Consequences of the Magnetotail Reconnection	301
11.3.4	Cause of the Near-Earth Reconnection	306
	References	308

A magnetic reconnection X-line extending more than 390 Earth radii in the solar wind

T. D. Phan¹, J. T. Gosling², M. S. Davis¹, R. M. Skoug³, M. Øieroset¹, R. P. Lin¹, R. P. Lepping⁴, D. J. McComas⁵, C. W. Smith⁶, H. Reme⁷ & A. Balogh⁸

Magnetic reconnection in a current sheet converts magnetic energy into particle energy, a process that is important in many laboratory¹, space^{2,3} and astrophysical contexts^{4,5}. It is not known at present whether reconnection is fundamentally a process that can occur over an extended region in space or whether it is patchy and unpredictable in nature⁷. Frequent reports of small-scale flux ropes and flow channels associated with reconnection^{8–13} in the Earth's magnetosphere raise the possibility that reconnection is intrinsically patchy, with each reconnection X-line (the line along which oppositely directed magnetic field lines reconnect) extending at most a few Earth radii (R_E), even though the associated current sheets span many tens or hundreds of R_E . Here we report three-spacecraft observations of accelerated flow associated with reconnection in a current sheet embedded in the solar wind flow, where the reconnection X-line extended at least $390R_E$ (or 2.5×10^6 km). Observations of this and 27 similar events imply that reconnection is fundamentally a large-scale process. Patchy reconnection observed in the Earth's magnetosphere is therefore likely to be a geophysical effect associated with fluctuating boundary conditions, rather than a fundamental property of reconnection. Our observations also reveal, surprisingly, that reconnection can operate in a quasi-steady-state manner even when undriven by the external flow.

Until recently, *in situ* observations of reconnection in space plasmas were made almost exclusively in the Earth's magnetosphere, in current sheets formed by the interaction between the solar wind and the geomagnetic field. Such current sheets have finite extents, and their boundary conditions (determined by the solar wind magnetic field) often change rapidly. It is generally difficult to establish the presence of an extended reconnection X-line in the magnetosphere from *in situ* measurements since that requires the presence of widely separated spacecraft detecting the same reconnection events. The chances of such conjunctions are exceedingly small because the spacecraft are seldom ideally positioned for such observations and because of the variable boundary conditions. The single event reported where two spacecraft (separated by $3R_E$) detected the same reconnection event at the magnetopause only allowed the deduction that the X-line was at least $3R_E$ long¹⁴. Remote observations of proton auroras¹⁵ and ionospheric convection¹⁶ have hinted at the presence of a magnetopause X-line up to $40R_E$ in length but that has not yet been confirmed by *in situ* observations.

The recent discovery of reconnection exhausts in the solar wind^{17,18} introduces a new laboratory where reconnection can be investigated by *in situ* measurements. The solar wind reconnection events are often associated with interplanetary coronal mass ejections, and the magnetic field orientations on the two sides of the current sheets are

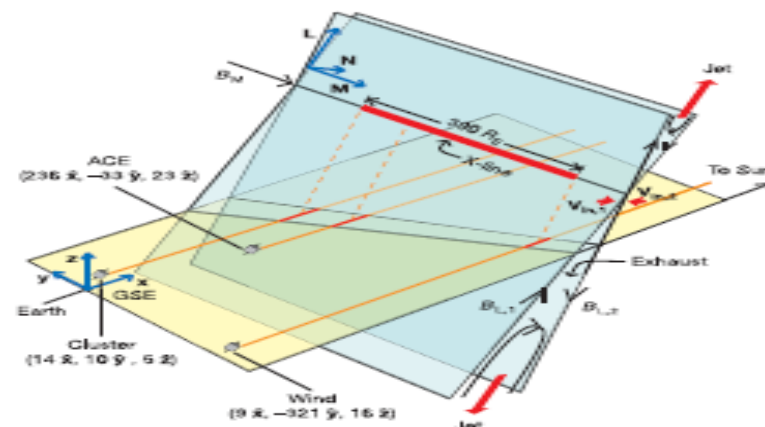
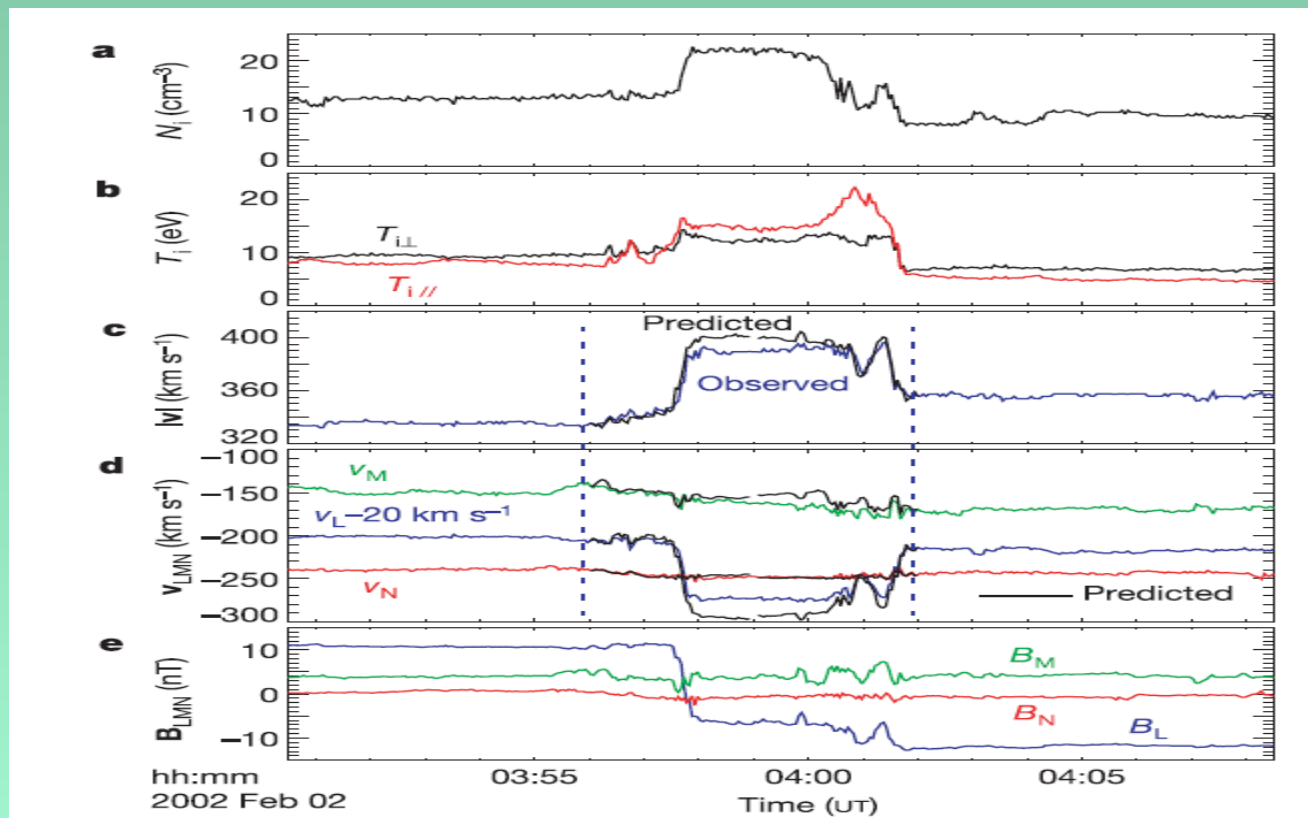


Figure 1 | Diagram of the encounters of three spacecraft with an extended ($390R_E$) magnetic reconnection X-line in the solar wind. Reconnection in the current sheet (in blue) occurs at the X-line between magnetic field lines with large anti-parallel components $B_{L,1}$ and $B_{L,2}$; the resulting bi-directional plasma jets (confined to the reconnection exhausts) can be observed far from the X-line. The ACE, Cluster and Wind spacecraft positions are shown in units of Earth radius (R_E) and in geocentric solar ecliptic (GSE) coordinates with the x-axis pointing from Earth to Sun, the y-axis pointing towards dusk and the z-axis parallel to the ecliptic pole. All three spacecraft were relatively close to the ecliptic plane (in yellow). ACE was $222R_E$ upstream of Cluster while Wind was $331R_E$ downstream of Cluster. Also shown is the LMN current sheet coordinate system, with N along the overall current sheet normal, M along the X-line direction and L along the anti-parallel magnetic field direction. The current sheet normal ($0.71\hat{x} + 0.60\hat{y} - 0.37\hat{z}$) in GSE, is tilted 45° relative to the Sun–Earth line. The X-line is oriented along $(0.47\hat{x} - 0.79\hat{y} - 0.39\hat{z})$ in GSE. The thick solid red line is the ($390R_E$) portion of the X-line whose effect is observed by the three spacecraft. The solid orange lines denote the spacecraft trajectory relative to the solar wind, with the red line portion marking the intersections of the exhaust with the spacecraft. The total reconnected magnetic flux ($= V_{in,1}B_{L,1}L_{X-130e}$ or $V_{in,2}B_{L,2}L_{X-130e}$) is determined by the inflow velocity, V_{in} , the strength of the anti-parallel field components, $B_{L,1}$, and the length of the X-line, L_{X-130e} . The angle of the diverging exhausts is exaggerated for illustration. The actual calculated angle is -4° . B_M is the magnetic field along the X-line.

Evidence of magnetic reconnection in the solar wind

- Bifurcated current sheets
- Double-step magnetic rotations with a plateau in the middle
- Anti-correlated (correlated) V-B => Parallel (anti-parallel) Alfvén waves
- Jet (Reconnection exhaust)



Magnetic reconnection at Magnetic Cloud Boundary Layers

Outer boundaries (Mf, Mt) of MCBL often display properties of magnetic reconnection characterized by a 3 “high-state” of plasma:

- high proton temperature
- high proton density
- high plasma beta

and corresponding 3 magnetic signatures:

- intensity drop
- abrupt latitudinal angle changes
- abrupt azimuthal angle changes

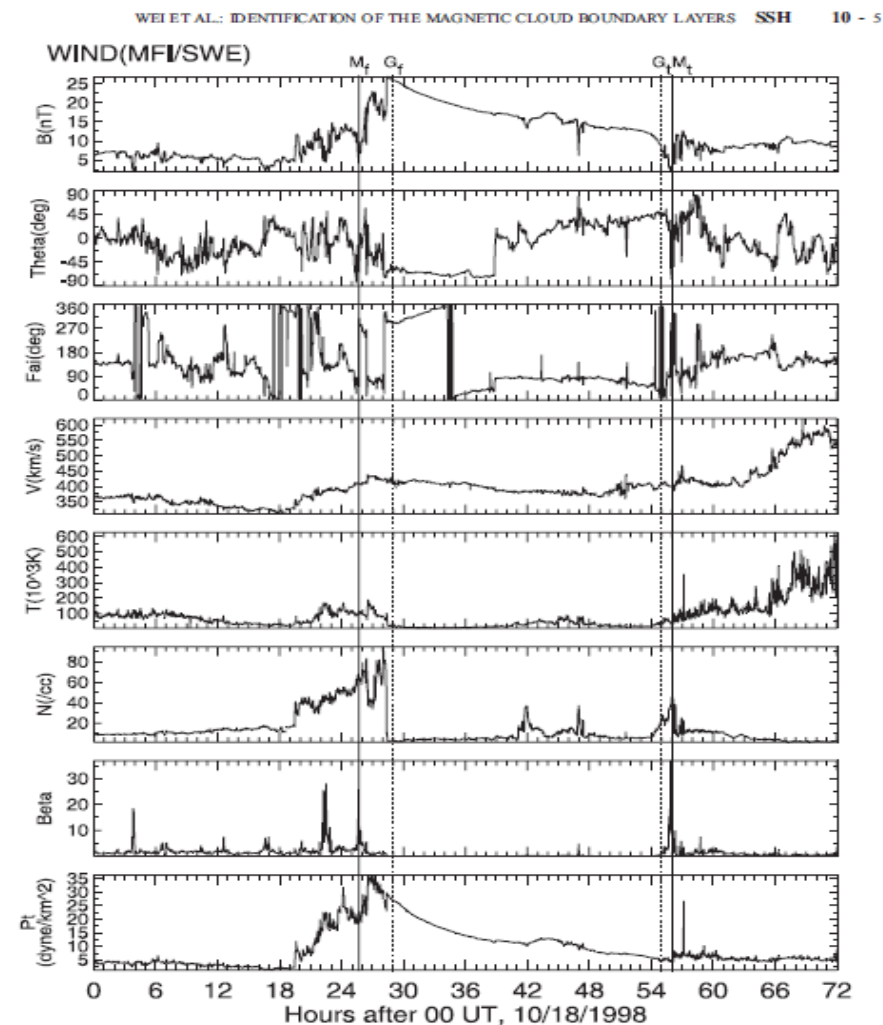


Figure 2. A magnetic cloud preceded by a shock was observed by Wind during 19–20 October 1998. The panels show from top to bottom the magnetic field magnitude, its latitude and azimuthal angles, θ and ϕ , in GSE coordinates, the proton temperature, density and velocity, plasma β , and total pressure.

Ref: Wei et al., JGR (2003): WIND data of ICME of 10/18/1998

DETECTION OF CURRENT SHEETS AND MAGNETIC RECONNECTIONS AT THE TURBULENT LEADING EDGE OF AN INTERPLANETARY CORONAL MASS EJECTION

ABRAHAM C.-L. CHIAN^{1,2} AND PABLO R. MUÑOZ²

¹California Institute of Technology, Pasadena, CA 91125, USA

²National Institute for Space Research (INPE) and World Institute for Space Environment Research (WISER), P.O. Box 515, São José dos Campos SP 12227-010, Brazil; abraham.chian@gmail.com, pablocus@gmail.com

Received 2010 November 25; accepted 2011 April 18; published 2011 May 10

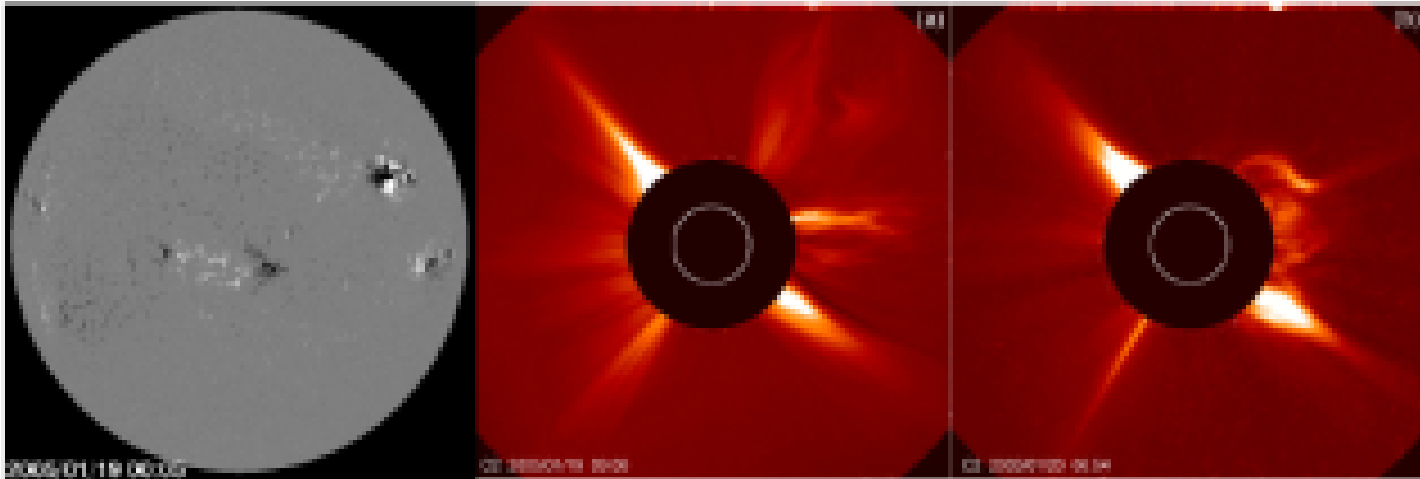
ABSTRACT

The relation between current sheets, turbulence, and magnetic reconnections at the leading edge of an interplanetary coronal mass ejection detected by four *Cluster* spacecraft on 2005 January 21 is studied. We report the observational evidence of two magnetically reconnected current sheets in the vicinity of a front magnetic cloud boundary layer with the following characteristics: (1) a Kolmogorov power spectrum in the inertial subrange of the magnetic turbulence, (2) the scaling exponent of structure functions of magnetic fluctuations exhibiting multi-fractal scaling predicted by the She–Leveque magnetohydrodynamic model, and (3) bifurcated current sheets with the current density computed by both single-spacecraft and multi-spacecraft techniques.

Key words: magnetic reconnection – plasmas – shock waves – solar wind – Sun: coronal mass ejections (CMEs) – turbulence

Coronal Mass Ejection (CME) events of 19-20 January 2005

(AR 10720)



Left panel shows a MDI image on 19 January 2005. An X-class solar flare occurred at 08:22 UT within active region AR 10720, visible in the upper right-hand corner of the Middle panel which shows a LASCO C2 image of the CME on 19 January 2005. Right panel shows a LASCO C2 image of the CME on 20 January 2005.

Refs: Chian & Muñoz ApJL, 2011

Miranda, Chian, et al., IAU 286, 2010

Muñoz, Chian, et al., IAU 286, 2010

ICME event of 21-22 January 2005: Cluster data upstream of the Earth's bow shock

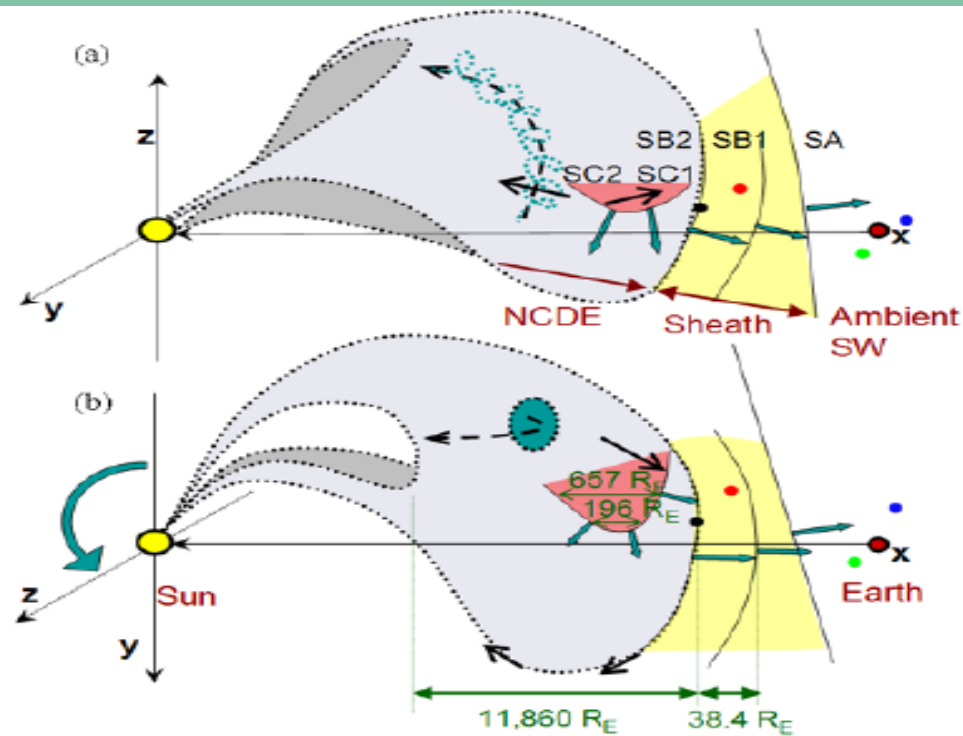


Figure 9 Possible interpretation of the global geometry of the ICME observed on 21 – 22 January 2005 near L1. The ICME shock front, sheath and ejecta are projected on (a) the noon – midnight meridional plane and (b) the ecliptic plane (in the GSE Cartesian coordinate system), with perspective rendered in dark grey. Scales in the \hat{X}_{GSE} direction are shrinking (with time). *Wind*, *ACE*, *Cluster* and *Geotail* are indicated by circles filled in black, red, green and blue, respectively. The yellow and blue grey areas represent the sheath and the ejecta, respectively. Discontinuity normals are indicated with blue arrows. IMF orientations observed or inferred at different locations in the ejecta are indicated with plain black arrows. A curved dashed black arrow represents the main axis of the interplanetary flux rope, with the stronger inner helicoidal fields indicated in blue. The counterclockwise rotation of the corresponding coronal flux rope axis is indicated by a blue rounded arrow in (b).

Ref: Foullon et al., SP (2007)

Detection of current sheets & Kolmogorov magnetic turbulence

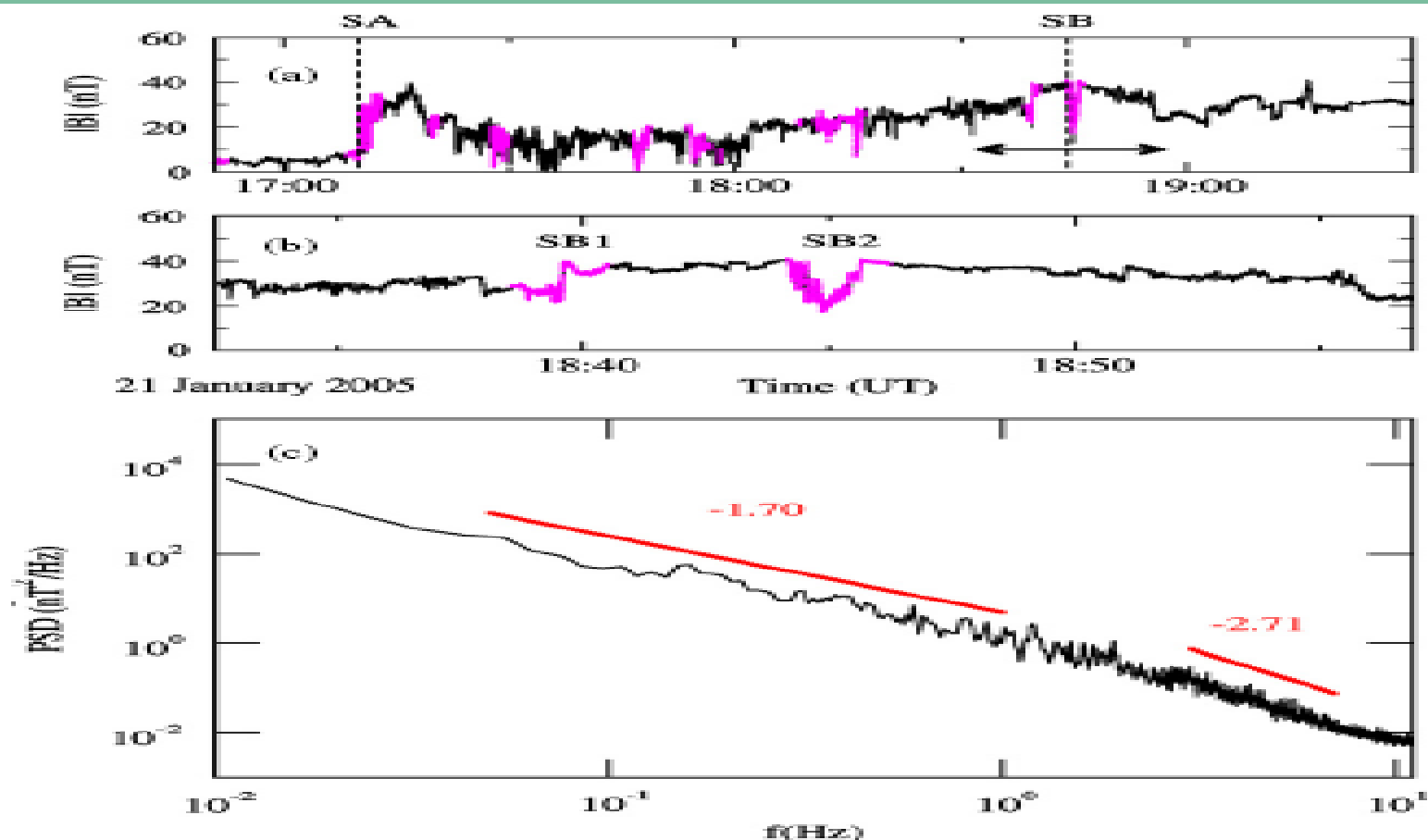


Figure 1. Detection of current sheets and magnetic turbulence by *Cluster-I* at the ICME shock of 2005 January 21. (a) Time series of $|B|$ (nT) superposed by current sheets detected by the Li (2008) method, for the critical angle $\theta = 60^\circ$ and the timescale $T = 120$ s. Magenta dots indicate the points that belong to a current sheet. SA denotes the primary shock arrival. SB1 and SB2 denote the two current sheets associated with the leading edge (SB) of the ICME ejecta. (b) An enlargement of the time interval marked by a bar in (a). (c) Power spectral density, PSD ($\text{nT}^2 \text{Hz}^{-1}$), of $|B|$ for the time interval of (b); straight lines indicate the inertial and dissipative subranges. The spectral indices are calculated by a linear regression of the log-log PSD data.

- *Current sheets detected by the technique of Li, ApJL (2008)*

Universal scaling laws for well-developed MHD turbulence

The departure from self-similarity in the magnetic field fluctuations can be quantified by comparing the scaling exponents of higher-order structure functions within the inertial subrange against the Kolmogorov universality theory (Frisch, 1995). The characterization of departures from Kolmogorov's 1941 theory (hereafter K41) is of great interest since the K41 theory is a result based on the assumption that the turbulence is homogeneous and isotropic (i.e., self-similar). The upper panels of Fig. 8 show the structure functions obtained from the following formula (de Wit and Krasnoselskikh, 1996).

$$S_p(\tau) = \langle |B_{i+\tau} - B_i|^p \rangle \sim \tau^{\alpha(p)}, \quad (3)$$

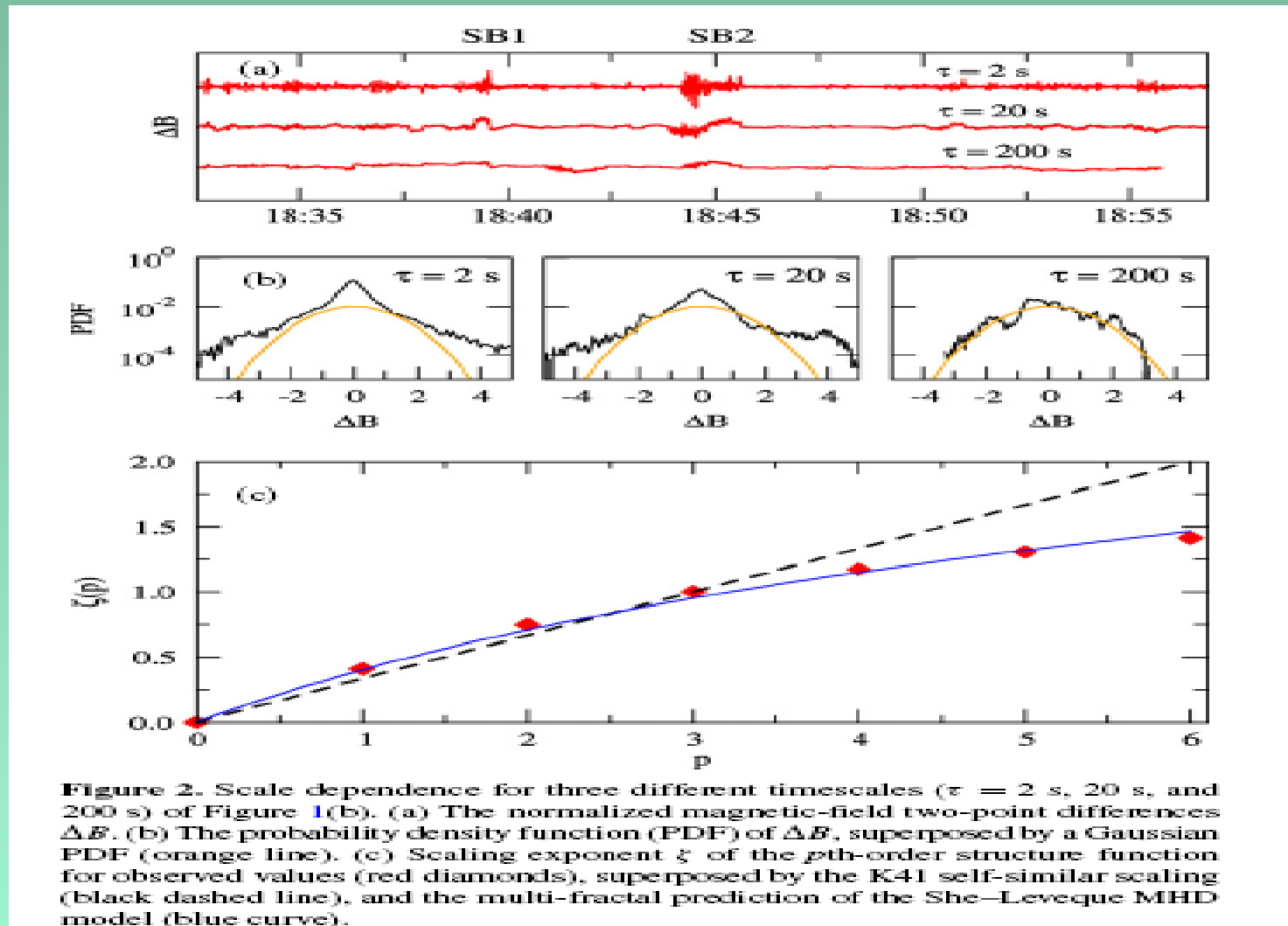
Applying the extended self-similarity (ESS) technique of Benzi et al. (PRE 1993) to compute the **scaling exponent**:

$$\zeta(p) \sim \alpha(p)/\alpha(3), \quad S_p(\tau) \sim [S_3(\tau)]^{\zeta(p)}$$

She-Leveque (PRL1994) model for the universality of the scaling exponent of structure function (of order p), for a Kolmogorov $-5/3$ power spectrum, was extended by Muller, Biskamp & Grappin (PRE 2003) for sheetlike dissipative structures in a well-developed anisotropic MHD turbulence, where g is an adjustable parameter:

$$\zeta(p) = \frac{p}{g^2} + 1 - \left(\frac{1}{g}\right)^{p/g}$$

Magnetic turbulence: Intermittent, nongaussian & multifractal



- Good agreement with the multi-fractal scaling predicted by the She-Leveque model of fully-developed MHD turbulence developed by Muller, Biskamp & Grappin (PRE 2003)

Magnetic reconnection: Anti-correlated /correlated Alfvén waves

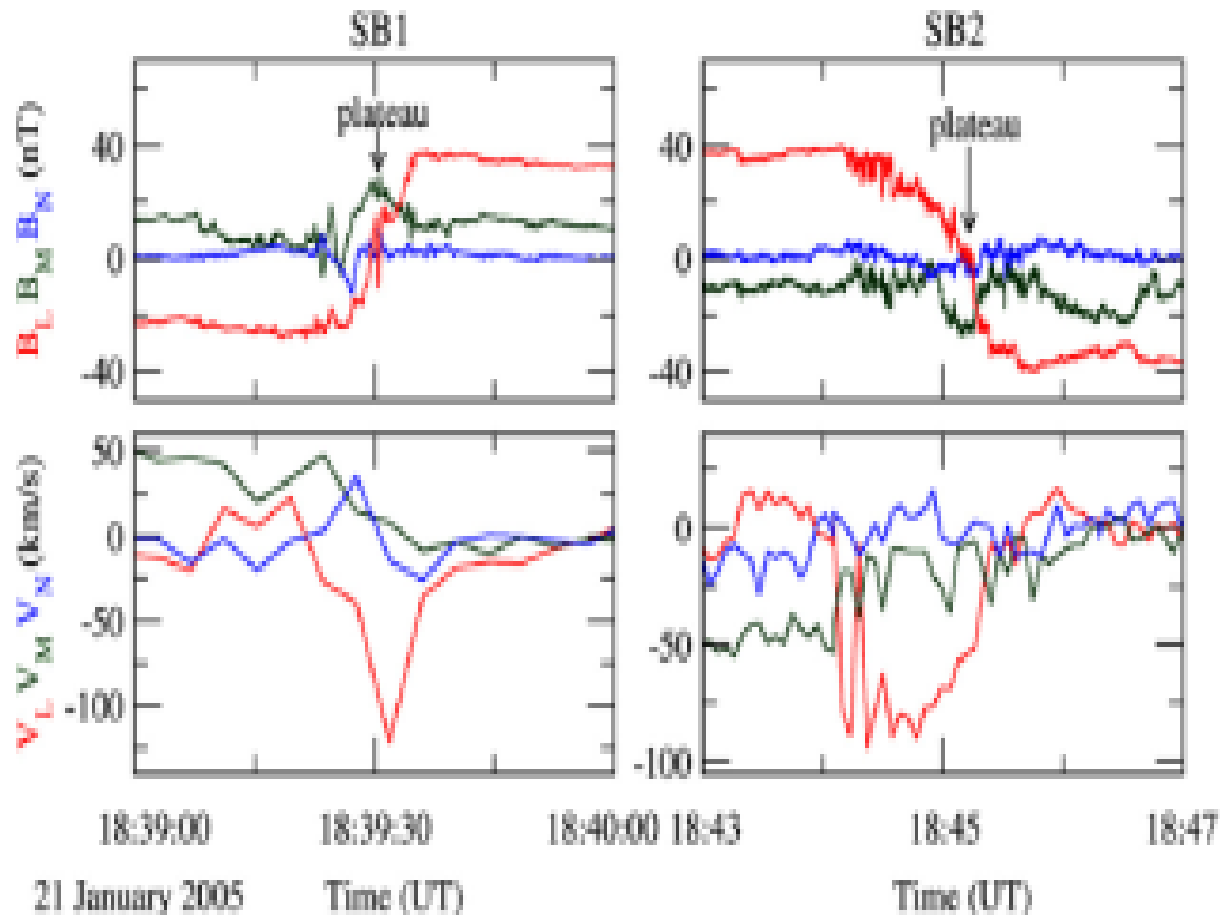


Figure 4. B_L (red), B_M (green), and B_Y (blue) are the components of \mathbf{B} measured by Cluster-1 in the LMN coordinates; V_L (red), V_M (green), and V_Y (blue) are the components of \mathbf{V} . This figure shows observational evidence of bifurcated current sheets SB1 and SB2, with a plateau at B_L in the middle of each bifurcated current sheet, and counter-propagating Alfvén waves at two edges of SB1 and SB2.

- *[BL, VL] of SB1 (SB2) present evidence of anti-correlated (correlated) and correlated (anti-correlated) Alfvén waves: minimum variance analysis*

Magnetic reconnection: Current sheets & Jets

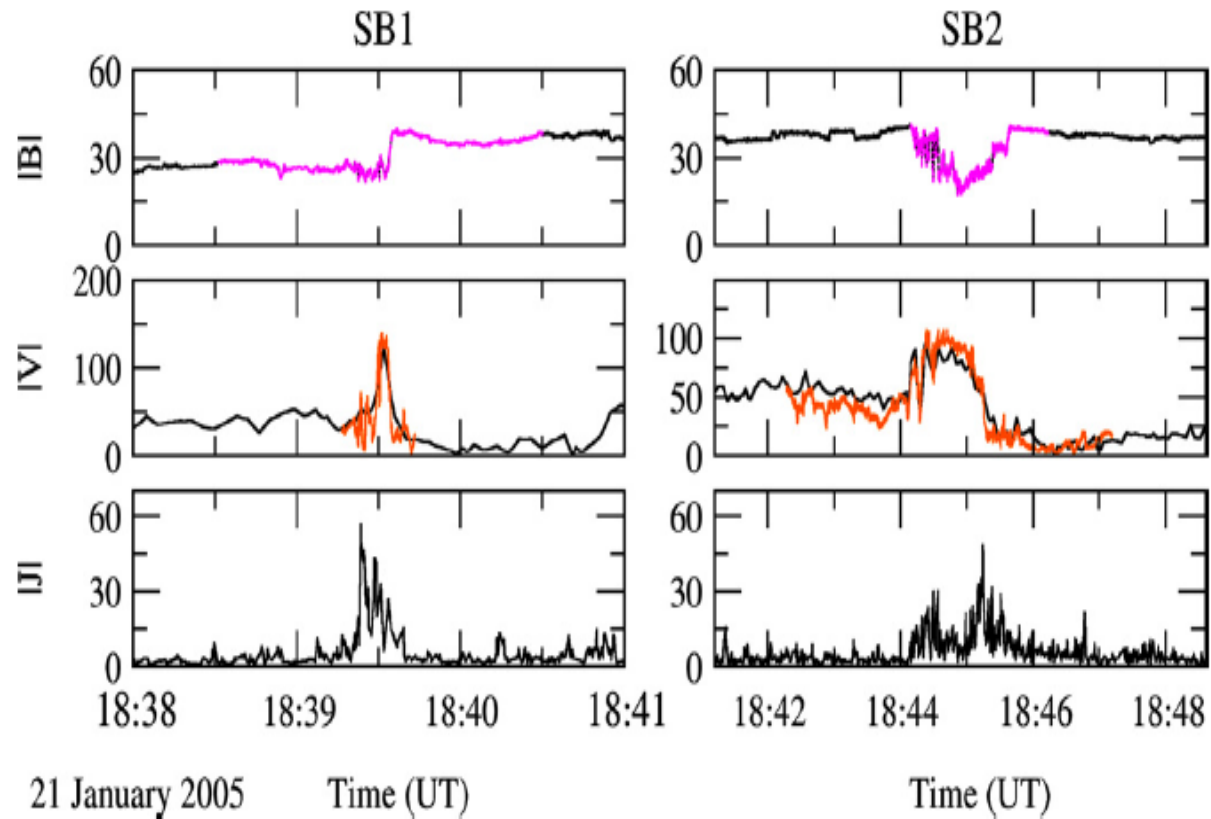


Figure 3. Detection of magnetic reconnections at the leading edge of ICME associated with the current sheets SB1 and SB2 (magenta). $|\mathbf{B}|$ (nT) is the modulus of magnetic field (enlargement of Figure 1(b)); $|\mathbf{V}|$ (km s^{-1}) is the modulus of the observed plasma velocity (black) and the plasma velocity (orange) predicted by the magnetic reconnection theory of Sonnerup et al. (1981); $|\mathbf{J}|$ (nA m^{-2}) is the modulus of current density computed by the multi-spacecraft curlometer technique of Dunlop et al. (2002).

- V computed by the magnetic reconnection theory of Sonnerup et al. (1981)
- J computed by the curlometer technique using multi-spacecraft Cluster data

Magnetic reconnection: Bifurcated current sheets

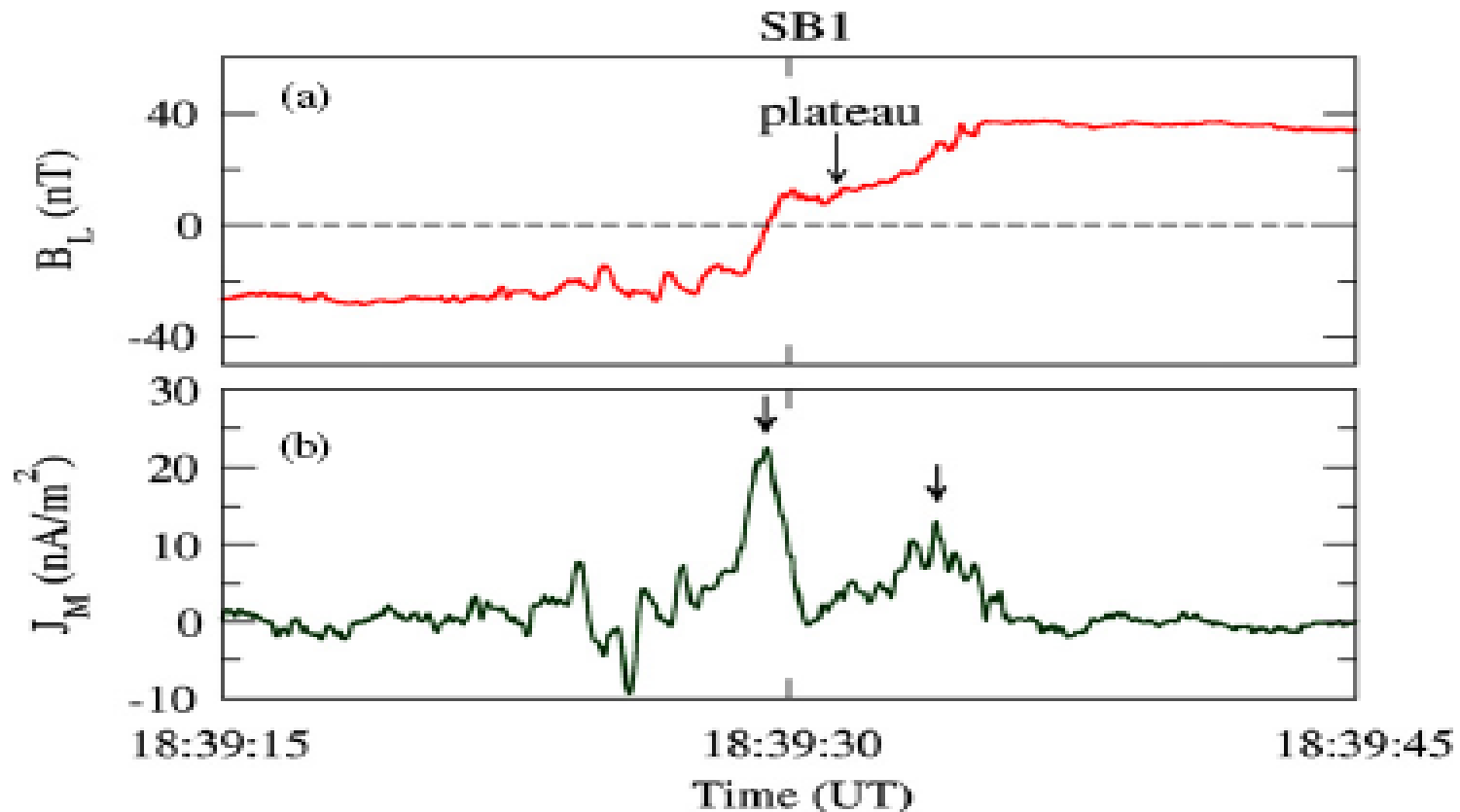


Figure 5. Direct evidence of a bifurcated current sheet SB1 measured by *Cluster-3*. (a) Two-step temporal variation of B_L with a plateau in the middle of the current sheet. (b) J_M calculated from B_L showing double peaks at both edges of the current sheet.

JM computed from BL using Ampere's Law & Taylor's hypothesis => Bifurcated current sheets

Ground observation of the ICME of 21-22 January 2005

Ground magnetometer data at Vassouras (VSS), Brazil

(Geomagnetic latitude: $\sim 19^\circ$)

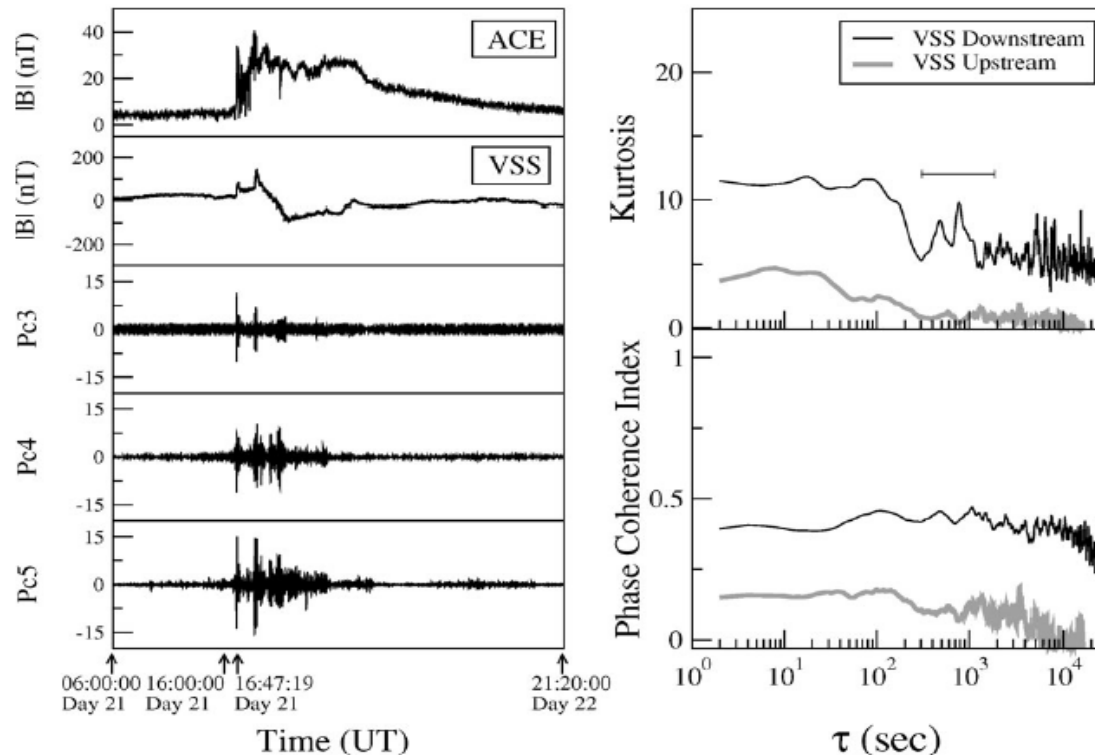


Figure 6. (a) From top to bottom: time series of $|B|$ (nT) measured by ACE for the ICME event of 21–22 January 2005; modulus of the Earth's geomagnetic field $|B|$ (nT) measured by a ground magnetometer at Vassouras, Brazil; time series of Pc3 (10–45 s), Pc4 (45–150 s) and Pc5 (150–1000 s) micropulsations. (b) Kurtosis (upper panel) and the phase coherence index (lower panel) of $|B|$ measured by ACE and the ground magnetometer at VSS as a function of time scale τ .

Ref: Miranda, Chian+, IAU 264 (2010); Du et al. JGR (2008)

Upstream/downstream of shock ahead of an erupting coronal flux rope
3 November 2010

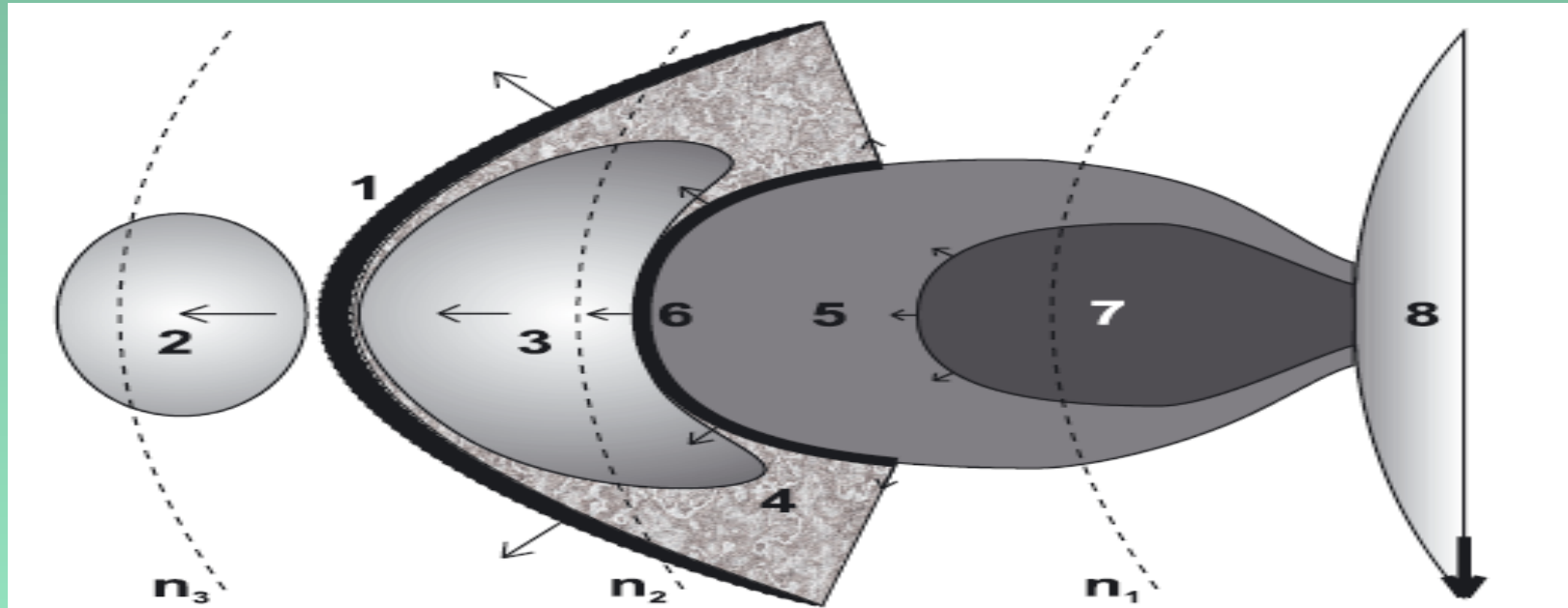


Fig. 9. Schematic illustration of the 3 November 2010 eruptive event observations combined with their interpretation in the frame of the upstream-downstream scenario (see text). View is from the heliographic north pole. Direction to the Earth is marked by a thick black arrow. Notations: (1) hypothetical shock wave, (2) LFC source of the type II burst, (3) its HFC source, (4) turbulent magnetosheath, (5) warm ($T \approx 1-2$ MK) plasma rim and (6) its LE, (7) hot ($T \approx 10$ MK) erupting flux rope or plasma blob if observed from the Earth, (8) photosphere. Thin black arrows show directions of the eruptive plasmas, shock wave, LFC and HFC sources motion. Lengths of the arrows are proportional to the corresponding velocities of motion. Levels of constant undisturbed background electron plasma concentration, assuming the natural gravitational stratification, are marked by black dashed arc-lines, and $n_1 > n_2 > n_3$.

Refs: Zimovets, Vilmer, Chian+, A&A 2012

SDO UV, RHESSI X ray & Nancay radio images of an erupting coronal flux rope

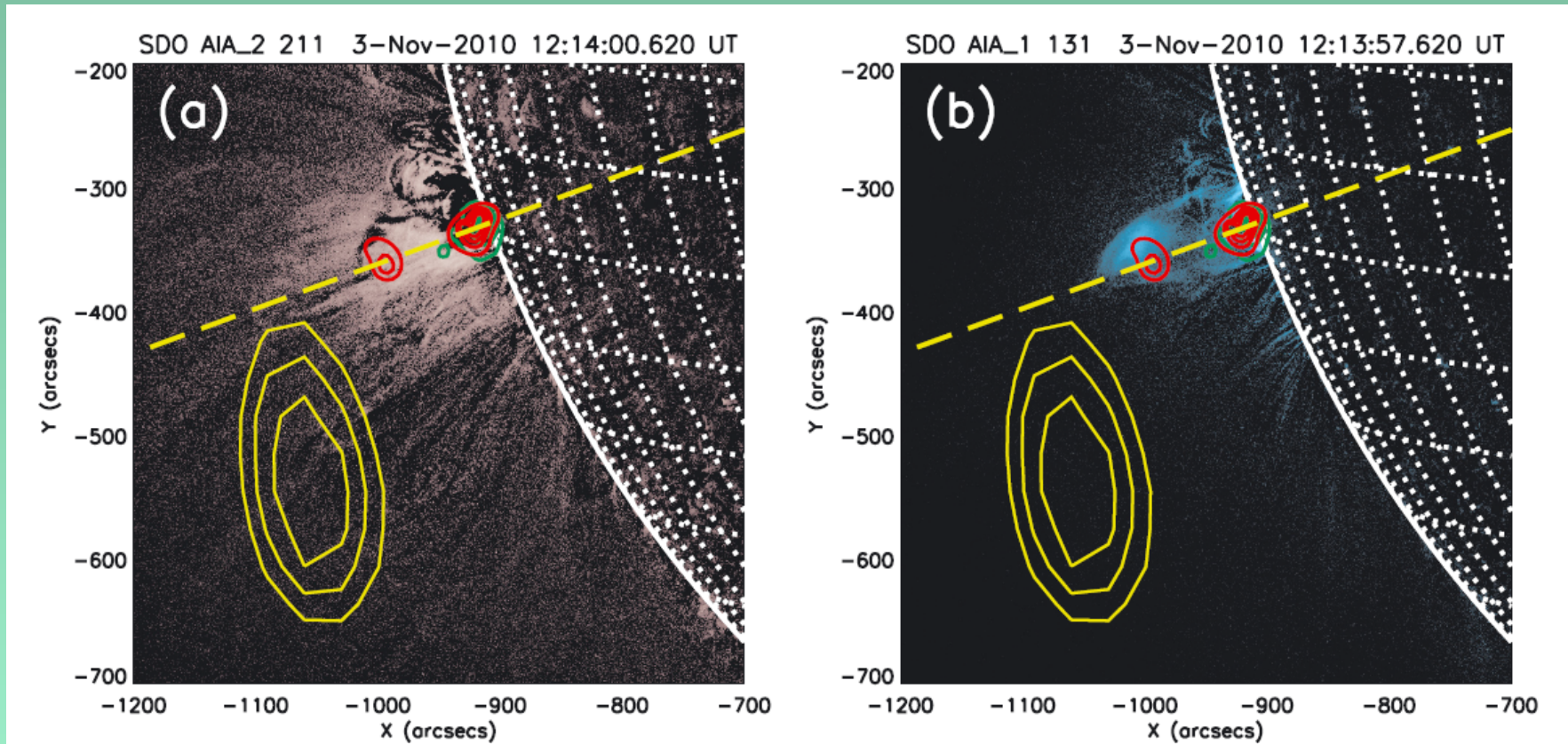


Fig. 2. Active area near the eastern limb of the Sun in the impulsive phase of the 3 November 2010 eruptive flare. AIA 211 Å a) and 131 Å b) base-difference images are overlaid by the RHESSI 6–12 keV (12:13:54–12:14:14 UT; light green) and 25–50 keV (12:13:54–12:14:14 UT; red) contours (20%, 40%, 60%, 80% of the peak flux), indicating locations of the flare soft and hard X-ray sources, respectively. AIA 211 Å base image was made at $\approx 12:00:02$ UT and 131 Å base image – at $\approx 12:00:11$ UT. Yellow ellipses are the NRH 445 MHz contours (70%, 80%, and 90% of the peak flux), which indicate the location of the decimetric radio emission source at the same moment. The thick dashed yellow straight line indicates a projection of the radius-vector passing through the centroid of the flare soft X-ray source onto the image plane.

LF type-II radio bursts ahead of an erupting coronal flux rope

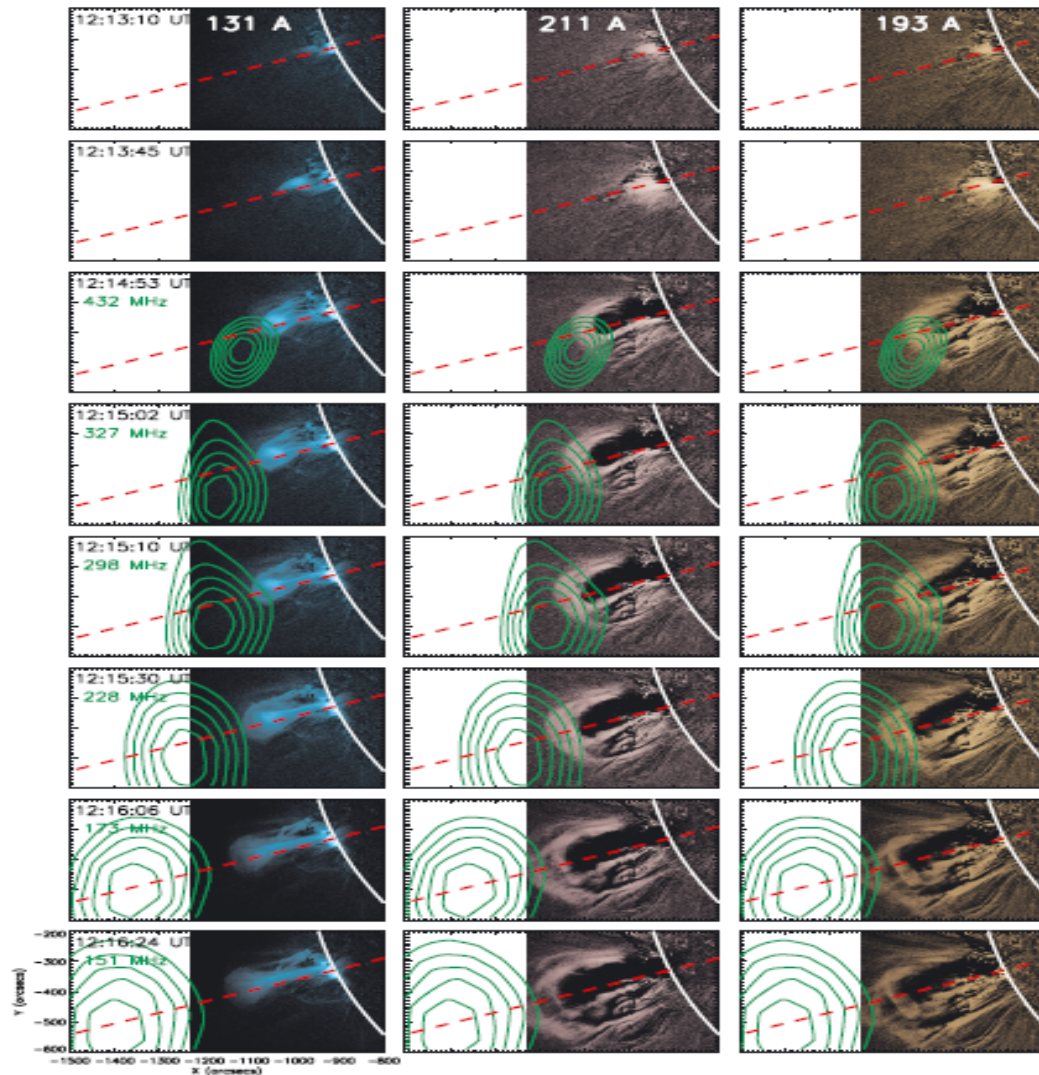


Fig. 6. Partial time sequence of AIA/SDO 131, 211, and 193 Å base-difference images in between 12:13:10 UT and 12:16:30 UT of 3 November 2010. Overplotted are the iso-intensity contours (50%, 60%, 70%, 80%, and 90% of the maximum) of the LFC source observed by NRH at different frequencies at a vicinity of times of its first appearance (indicated in the upper left corner of the AIA 131 Å images). One-second integrated NRH data is used. The closest AIA images in time to the NRH ones are shown (the time difference is less than eight seconds in each case). Solar limb is depicted by the thick white line. The red dashed straight line in all panels indicates a projection of the radius vector passing through the X-ray flare onto the image plane. The AIA's field of view is less than that of the NRH.

LF/HF type-II radio bursts at the leading edge of an erupting coronal flux rope

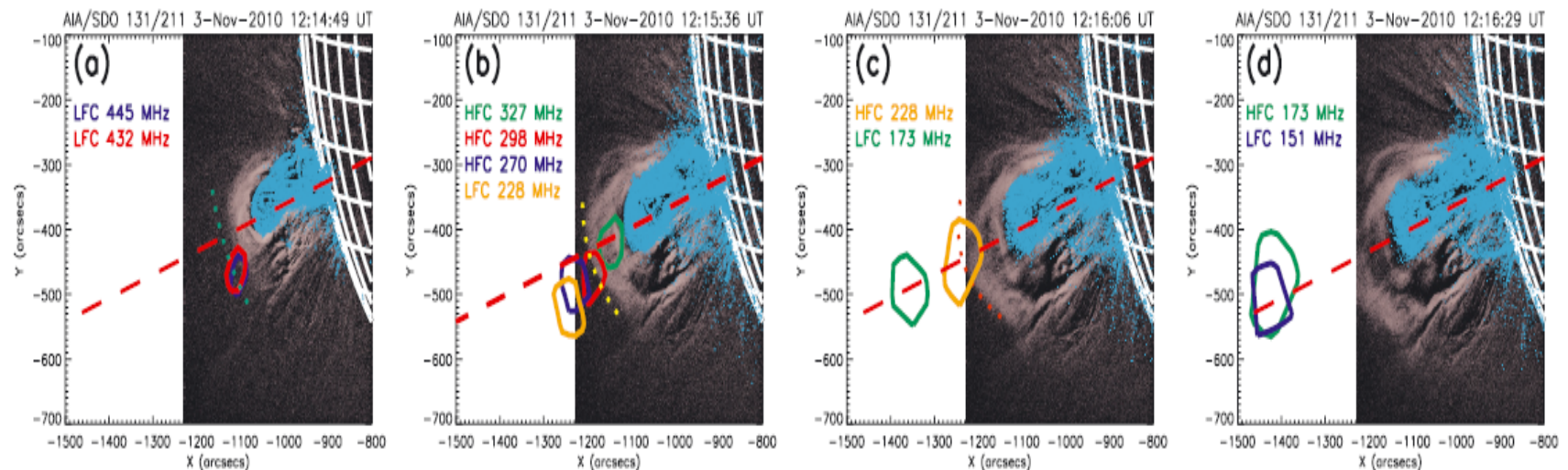
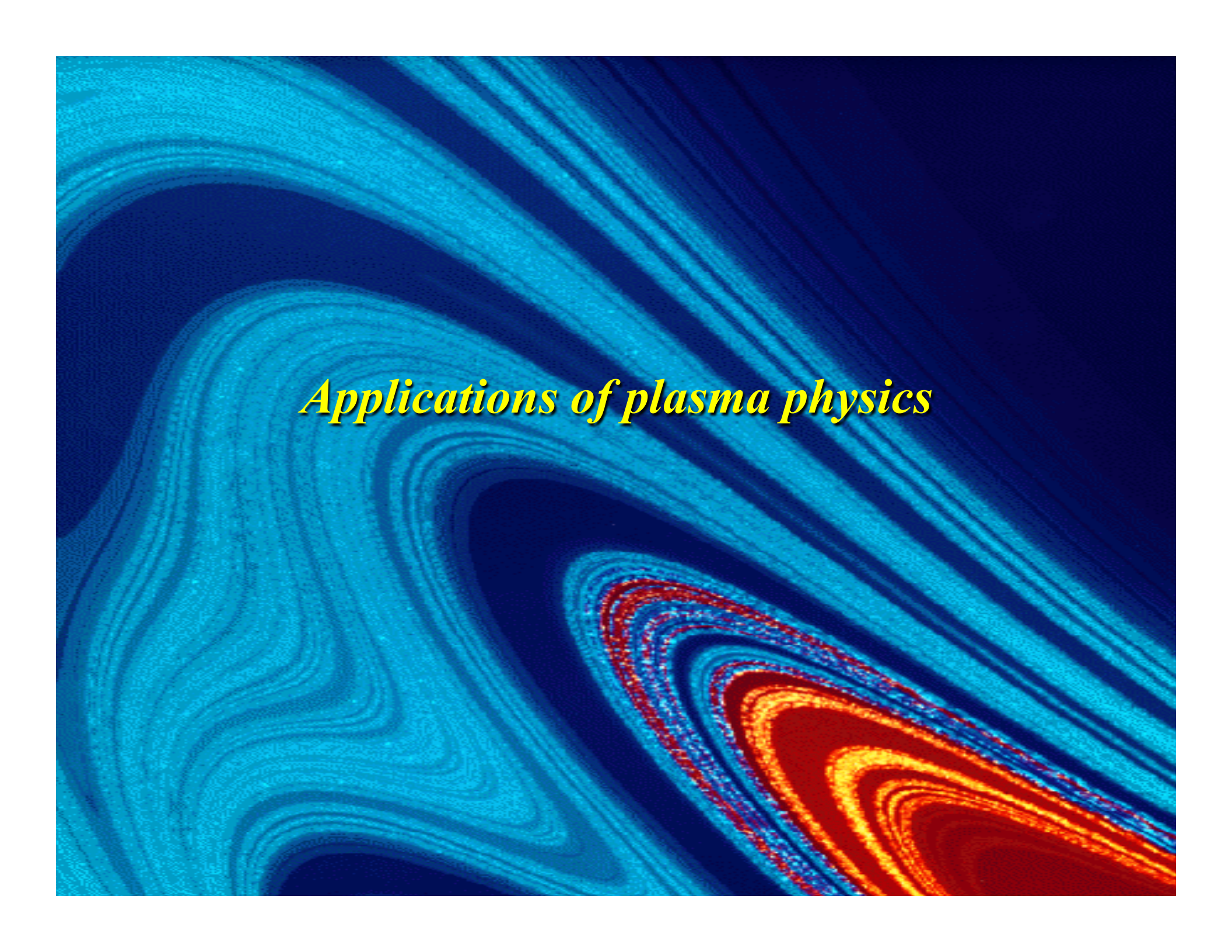
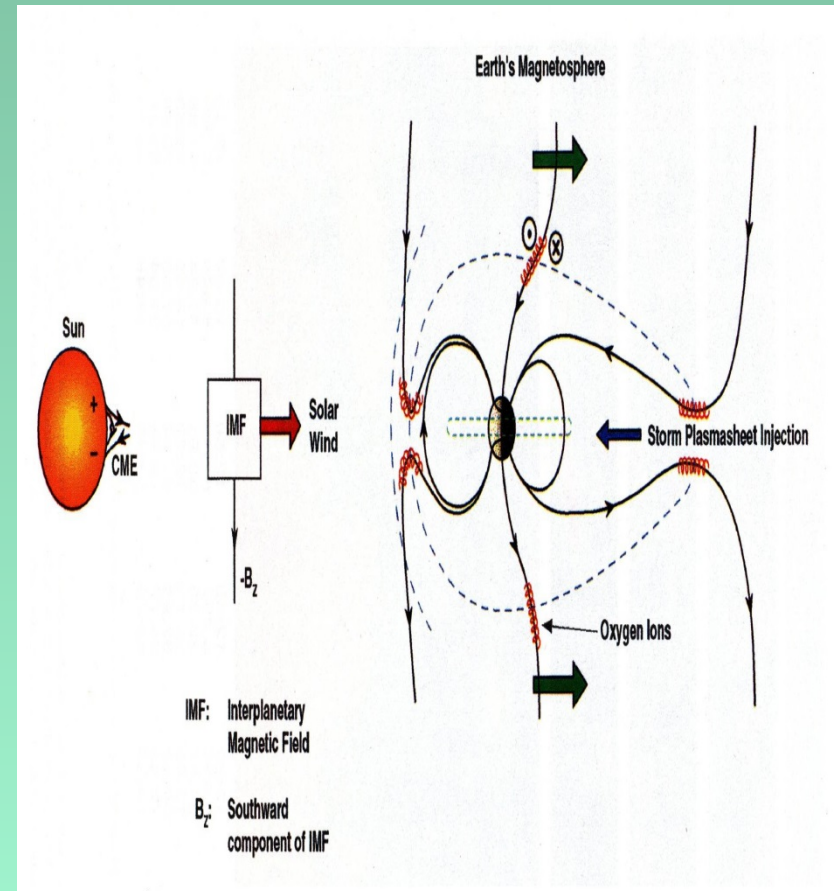
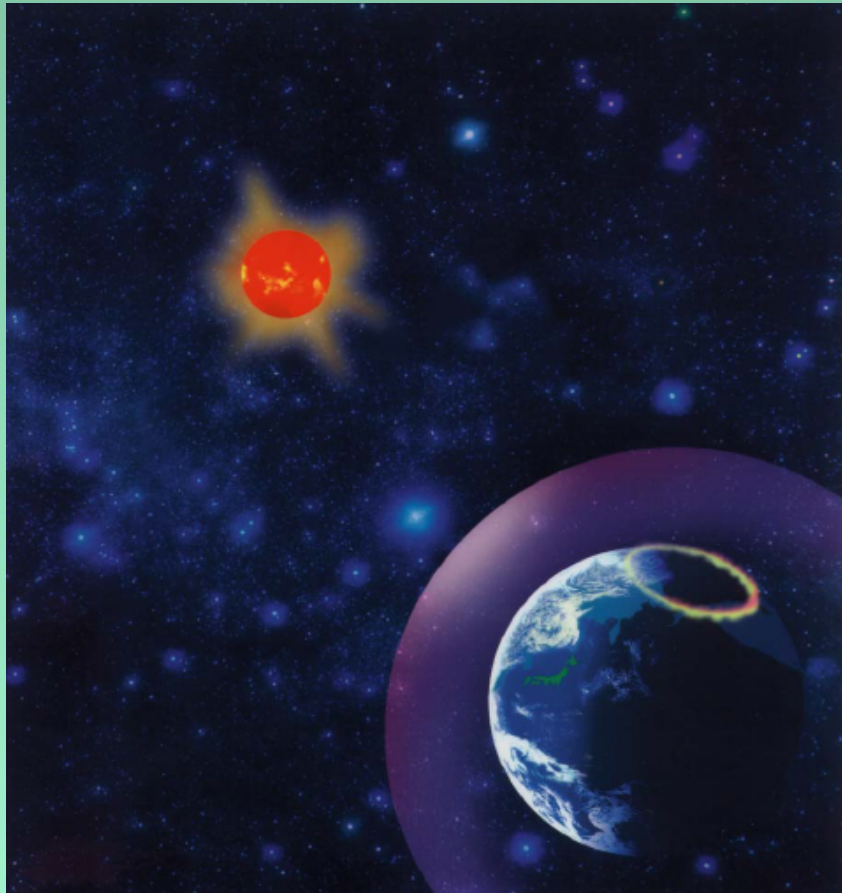


Fig. 7. Composite base-difference images of the active area near the eastern limb of the Sun made by AIA in 131 Å (turquoise) and 211 Å (purple) passbands at four different times of the 3 November 2010 event. These times are marked by dash-dotted vertical lines in Figs. 4 and 8. Green, yellow, and red dashed parabolas on panels a), b) and c), respectively, indicate the approximated LE of eruptive plasma observed by AIA in 211 Å passband. The parabolas' colors are consistent with the colorbar in Fig. 3. Solid lines of different colors are the NRH contours (95% of the peak flux), which indicate locations of centroids of the type II burst sources at different frequencies (indicated within each panel) at appropriate moments. All AIA and NRH images are matched within 5 s. Red dashed line in all panels indicates a projection of the radius-vector passing through the X-ray flare onto the image plane.

The background of the slide is an abstract, high-resolution image featuring complex, wavy patterns. The color palette is primarily deep blue and cyan, with a prominent region in the lower right corner transitioning into bright orange and red. The patterns resemble fluid dynamics or plasma instabilities, with swirling, layered structures that create a sense of depth and movement. The overall effect is a visually striking and scientific aesthetic.

Applications of plasma physics

Complex dynamics of solar-terrestrial relation: Sun-Earth relation & Space weather



Gonzalez and Tsurutani, INPE/JPL

Applications of plasma physics

- **Space weather**
- **Space climatology**
- **Plasma astrophysics**
- **Controlled thermonuclear fusion**
- **Plasma medicine**

17 Space Weather

L.J. Lanzerotti

17.1	Introduction	424
17.2	Early Technologies: Telegraph and Wireless	425
17.3	Growth in Electrical Technologies	427
17.4	The Space Age and Space Weather	429
17.4.1	Ionosphere and Earth Currents	429
17.4.2	Ionosphere and Wireless	430
17.4.3	Solar Radio Noise	431
17.4.4	Space Radiation Effects	432
17.4.5	Magnetic Field Variations	436
17.4.6	Micrometeoroids (and Space Debris)	436
17.4.7	Atmosphere: Low Altitude Spacecraft Drag	436
17.4.8	Atmosphere Water Vapor	437

**18 Effects of the Solar Cycle
on the Earth's Atmosphere**

K. Labitzke

18.1	Introduction	446
18.2	Data and Methods	446
18.3	Variability in the Stratosphere	447
18.4	Influences of the 11-Year Sunspot Cycle on the Stratosphere	448
18.4.1	The Stratosphere During the Northern Winter	448
18.4.2	The Stratosphere During the Northern Summer	453
18.5	The Solar Signal in the Troposphere	458
18.6	The QBO–Solar–Relationship Throughout the Year	459
18.7	Models and Mechanisms	461
18.8	Summary	463
	References	464

Part 5 Planets and Comets in the Solar System

19 Planetary Magnetospheres

M.G. Kivelson

19.1	Introduction	470
19.2	Parameters that Control Magnetospheric Configuration and Dynamics .	470
19.2.1	Properties of the Flowing Plasma	470
19.2.2	Properties of the Planet or Moon	473
19.2.3	Dimensionless Ratios Controlling Size and Dynamics	473
19.3	A Tour of Planetary Magnetospheres	474
19.3.1	Mini-Magnetospheres	474
19.3.2	Giant Magnetospheres of Rapidly Rotating Planets	480
19.3.3	Unclassified Magnetospheres	490
19.3.4	Mars: a Special Case	490
19.4	Summary: some Lessons for Earth	491
	References	492

20 The Solar-Comet Interactions

D.A. Mendis

20.1	Introduction	494
20.2	Cometary Reservoirs	494
20.3	The Nature of the Cometary Nucleus	496
20.4	Interaction with Solar Radiation	498
20.5	The Interaction with the Solar Wind	501
20.6	Comets as Probes of the Solar Wind	507
	References	514

An asymmetric solar wind termination shock

Edward C. Stone¹, Alan C. Cummings¹, Frank B. McDonald², Bryant C. Heikkilä³, Nand Lal³ & William R. Webber⁴

Voyager 2 crossed the solar wind termination shock at 83.7 AU in the southern hemisphere, ~ 10 AU closer to the Sun than found by Voyager 1 in the north^{1–4}. This asymmetry could indicate an asymmetric pressure from an interstellar magnetic field^{5,6}, from transient-induced shock motion⁷, or from the solar wind dynamic pressure. Here we report that the intensity of 4–5 MeV protons accelerated by the shock near Voyager 2 was three times that observed concurrently by Voyager 1, indicating differences in the shock at the two locations. (Companion papers report on the

plasma⁸, magnetic field⁹, plasma-wave¹⁰ and lower energy particle¹¹ observations at the shock.) Voyager 2 did not find the source of an anomalous cosmic rays at the shock, suggesting that the source is elsewhere on the shock^{12–14} or in the heliosheath^{15–19}. The small intensity gradient of Galactic cosmic ray helium indicates that either the gradient is further out in the heliosheath²⁰ or the local interstellar Galactic cosmic ray intensity is lower than expected²¹.

Low energy ions accelerated at the termination shock are observed upstream of the shock and in the heliosheath (Fig. 1). Voyager 2

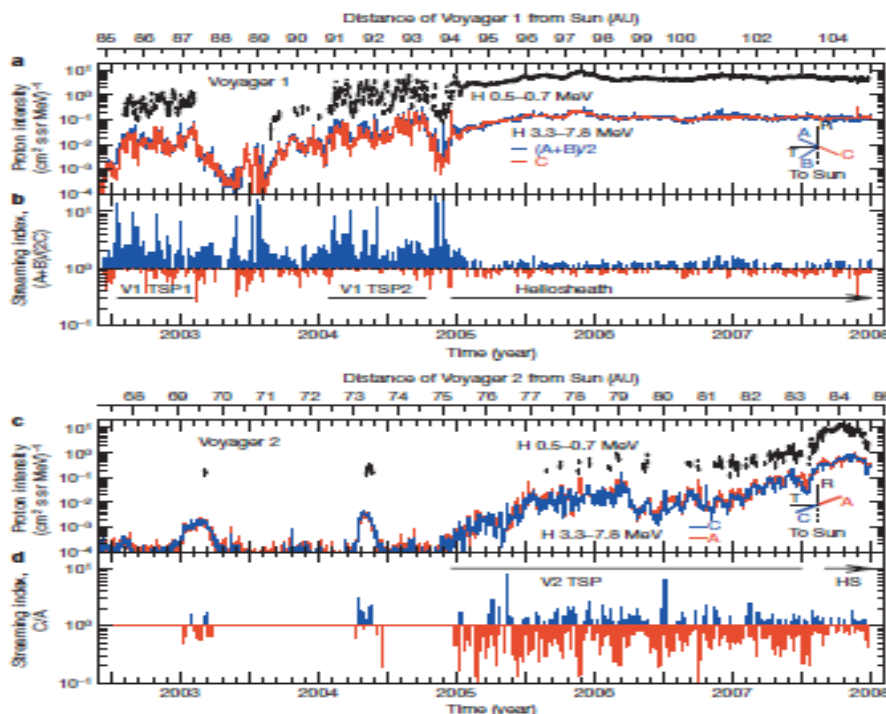
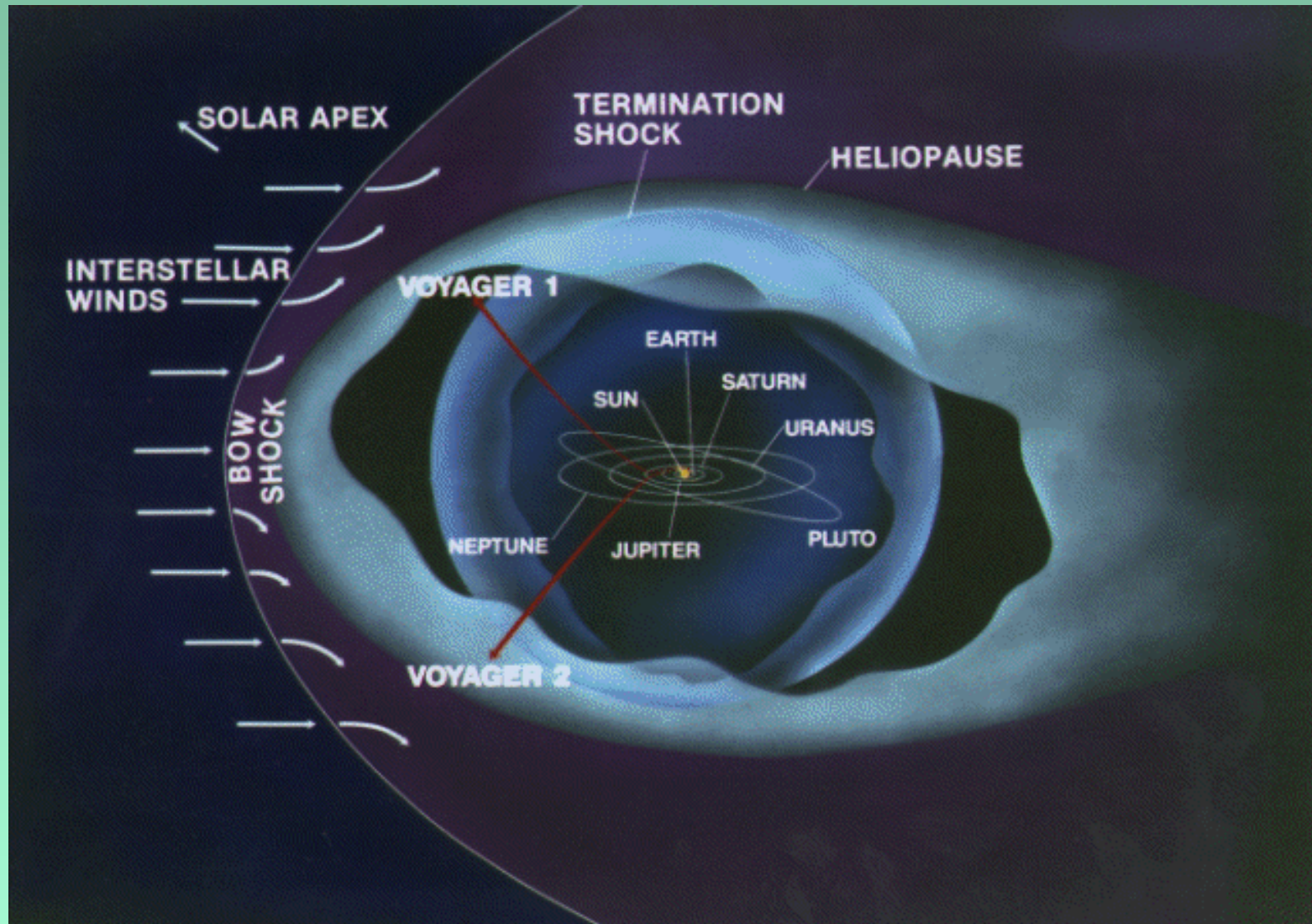


Figure 1 | Daily-averaged intensities and streaming of energetic termination shock particles that are accelerated at nearby regions of the shock. Voyager 1 and Voyager 2 crossed the shock and entered the heliosheath on 2004.96 (16 December 2004) at heliographic coordinates of $(34.3^\circ, 173^\circ)$ and on 2007.66 (30 August 2007) at $(-27.5^\circ, 216^\circ)$, respectively. Insets, telescope (A, B and C) viewing directions projected into the R-T plane, where $-R$ is towards the Sun and T is azimuthal. Error bars on black filled circles, ± 1 s.d. **a**, The proton intensities (H) at 3.3–7.8 MeV observed by Voyager 1 particle telescopes (A+B)/2 (blue trace) and by C (red trace) are highly variable upstream of the shock owing to variations in the connectivity along the spiral field line^{22,23}. The energetic ions are convected into the heliosheath, resulting in reduced variations. Similar properties are apparent in the intensity of 0.5–0.7 MeV protons observed by telescope A (black filled circles) and shown when the background correction was $<60\%$. V1 TSP1 and V1 TSP2, two episodes of termination shock particles observed by Voyager 1. **b**, The streaming index $(A+B)/(2C)$ for 3.3–7.8 MeV protons shows that upstream the ions at Voyager 1 were strongly beamed in the $-T$ direction, with intensities in the oppositely directed detectors differing by up to a factor of 10. The intensities are more nearly isotropic in the heliosheath. Blue indicates that the average intensity in telescopes A and B exceeds that in C, indicating flow in the $-T$ direction; red indicates the opposite. **c**, Same as **a** for Voyager 2 except that only telescopes A and C are used in determining the directional intensities of 3.3–7.8 MeV protons. **d**, Same as **b** for Voyager 2 except that only telescopes A and C are used. The upstream beaming was mainly in the $+T$ direction, opposite to that observed by Voyager 1 and consistent with the predicted east–west shock asymmetry resulting from a local interstellar magnetic field^{4–6}. Voyager 2 began observing upstream energetic ions at 75 AU from the Sun¹, 10 AU closer than did Voyager 1, leading to predictions that the shock would be closer in the southern hemisphere than in the north, but with significant differences in the predicted asymmetry^{24–27}. H.S., heliosheath.

¹California Institute of Technology, Pasadena, California 91125, USA. ²Institute for Physical Science and Technology, University of Maryland, College Park, Maryland 20742, USA. ³NASA/Goddard Space Flight Center, Greenbelt, Maryland 20771, USA. ⁴Department of Physics and Astronomy, New Mexico State University, Las Cruces, New Mexico 88003, USA.

Heliosphere



THE ASTROSPHERE OF THE ASYMPTOTIC GIANT BRANCH STAR IRC+10216

RAGHVENDRA SAHAI AND CHRISTOPHER K. CHRONOPOULOS

Jet Propulsion Laboratory, MS 183-900, California Institute of Technology, Pasadena, CA 91109, USA; sahai@jpl.nasa.gov

Received 2009 December 7; accepted 2010 January 26; published 2010 February 17

ABSTRACT

We have discovered a very extended shock structure (i.e., with a diameter of about $24'$) surrounding the well-known carbon star IRC+10216 in ultraviolet images taken with the *Galaxy Evolution Explorer* satellite. We conclude that this structure results from the interaction of IRC+10216's molecular wind with the interstellar medium (ISM), as it moves through the latter. All important structural features expected from theoretical models of such interactions are identified: the termination shock, the astrosheath, the astropause, the bow shock, and an astrotail (with vortices). The extent of the astropause provides new lower limits to the envelope age (69,000 years) and mass ($1.4 M_{\odot}$, for a mass-loss rate of $2 \times 10^{-5} M_{\odot} \text{ yr}^{-1}$). From the termination-shock standoff distance, we find that IRC+10216 is moving at a speed of about $\gtrsim 91 \text{ km s}^{-1} (1 \text{ cm}^{-3}/n_{\text{ISM}})^{1/2}$ through the surrounding ISM.

Key words: circumstellar matter – dust: extinction – ISM: structure – stars: AGB and post-AGB – stars: individual (IRC+10216) – stars: mass-loss

Asterosphere of CW Leonis (IRC+10216)

L54

SAHAI & CHRONOPOULOS

Vol. 711

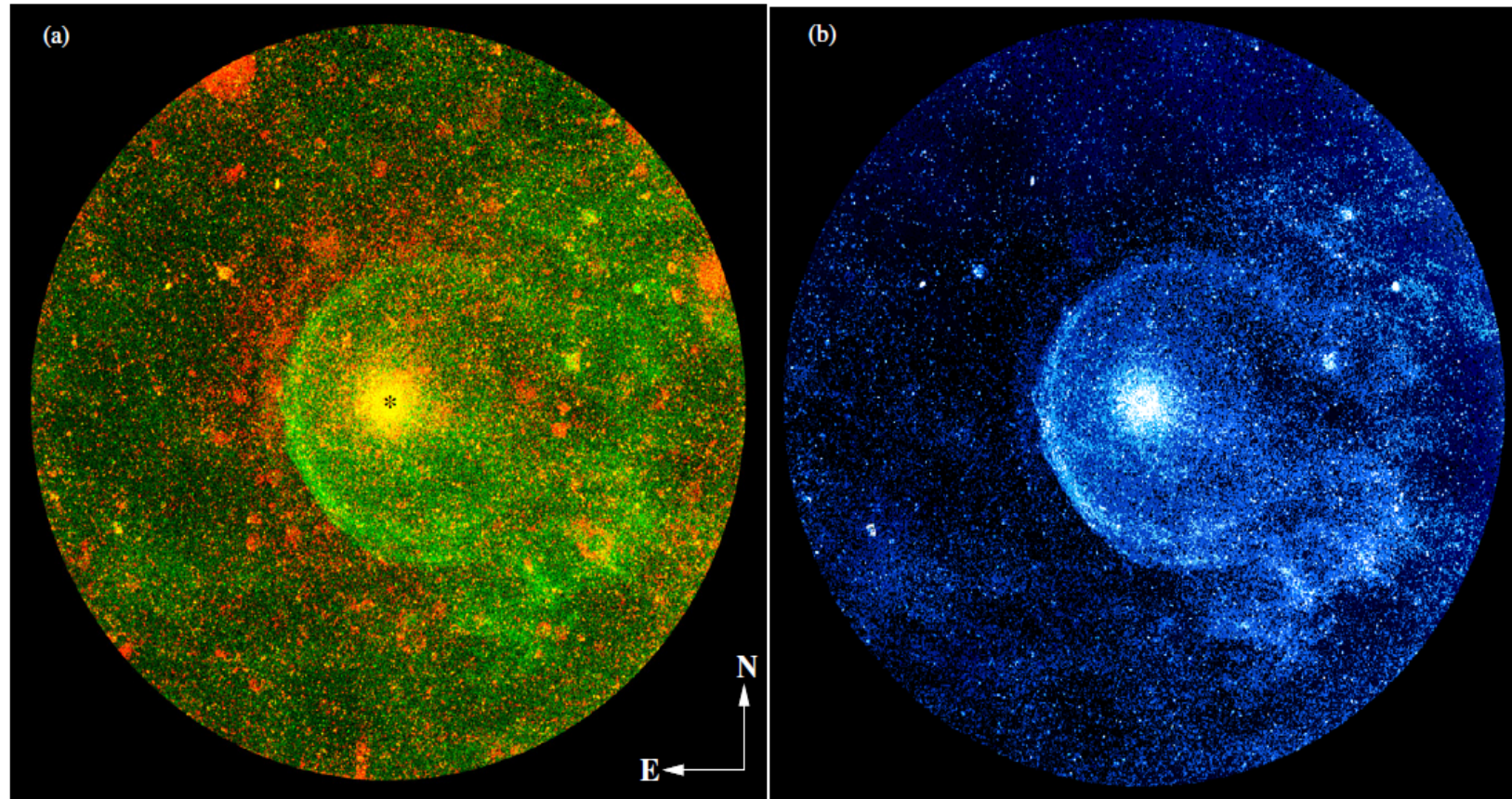


Figure 1. (a) Composite (NUV (red) and FUV (green)) *GALEX* image of IRC+10216 (the circular field of view (FOV) has a diameter of $61'.6 \times 61'.6$); the NUV (FUV) image was boxcar smoothed using a 3×3 (2×2) pixels box, and displayed using a linear (square-root) stretch. The location of the central star is indicated by a *; the bright round red patches and streaks at the edges of the NUV image are due to bright stars which could not be removed, and detector edge artifacts. (b) The FUV image (same FOV as in panel (a)), which is less affected by bright star residuals and artifacts, boxcar-smoothed using a 3×3 pixels box, and displayed using a linear stretch (in false color), to clearly show the detailed structure of the astropause and its tail.



Available online at www.sciencedirect.com



Advances in Space Research 46 (2010) 472–484

ADVANCES IN
SPACE
RESEARCH

(a COSPAR publication)

www.elsevier.com/locate/ast

The planetary–exoplanetary environment: A nonlinear perspective

Abraham C.-L. Chian^{a,*}, Maoan Han^b, Rodrigo A. Miranda^a, Chenggang Shu^c,
Juan A. Valdivia^d

^a *National Institute for Space Research (INPE) and World Institute for Space Environment Research (WISER), P. O. Box 515,
São José dos Campos-SP 12227-010, Brazil*

^b *Department of Mathematics, Shanghai Normal University, Shanghai 200234, China*

^c *Key Laboratory for Astrophysics, Shanghai Normal University, Shanghai 200234, China*

^d *Department of Physics, University of Chile, Santiago, Chile*

Received 15 March 2008; received in revised form 25 July 2009; accepted 25 July 2009

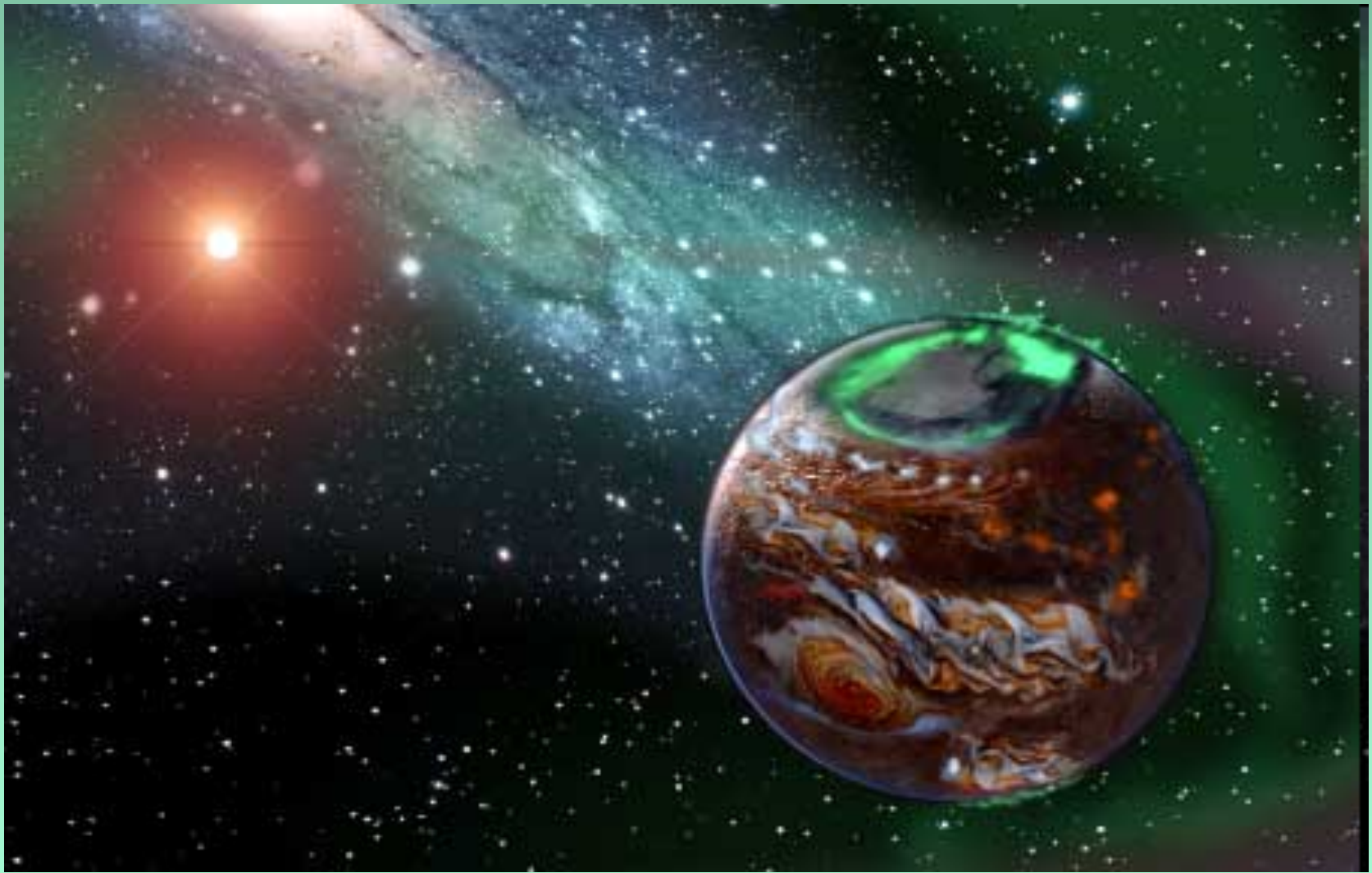
Abstract

A review of the fundamental physical processes in the planetary–exoplanetary environment is presented, with emphasis on nonlinear phenomena. First, we discuss briefly the detection of exoplanets and search for radio emissions from exoplanets. Next, we give an overview of the concepts of waves, instabilities, chaos and turbulence in the planetary–exoplanetary environment based on our present knowledge of the solar-terrestrial environment. We conclude by discussing cyclotron masers and chaos in nonthermal radio emissions in the planetary–exoplanetary environment.

© 2009 COSPAR. Published by Elsevier Ltd. All rights reserved.

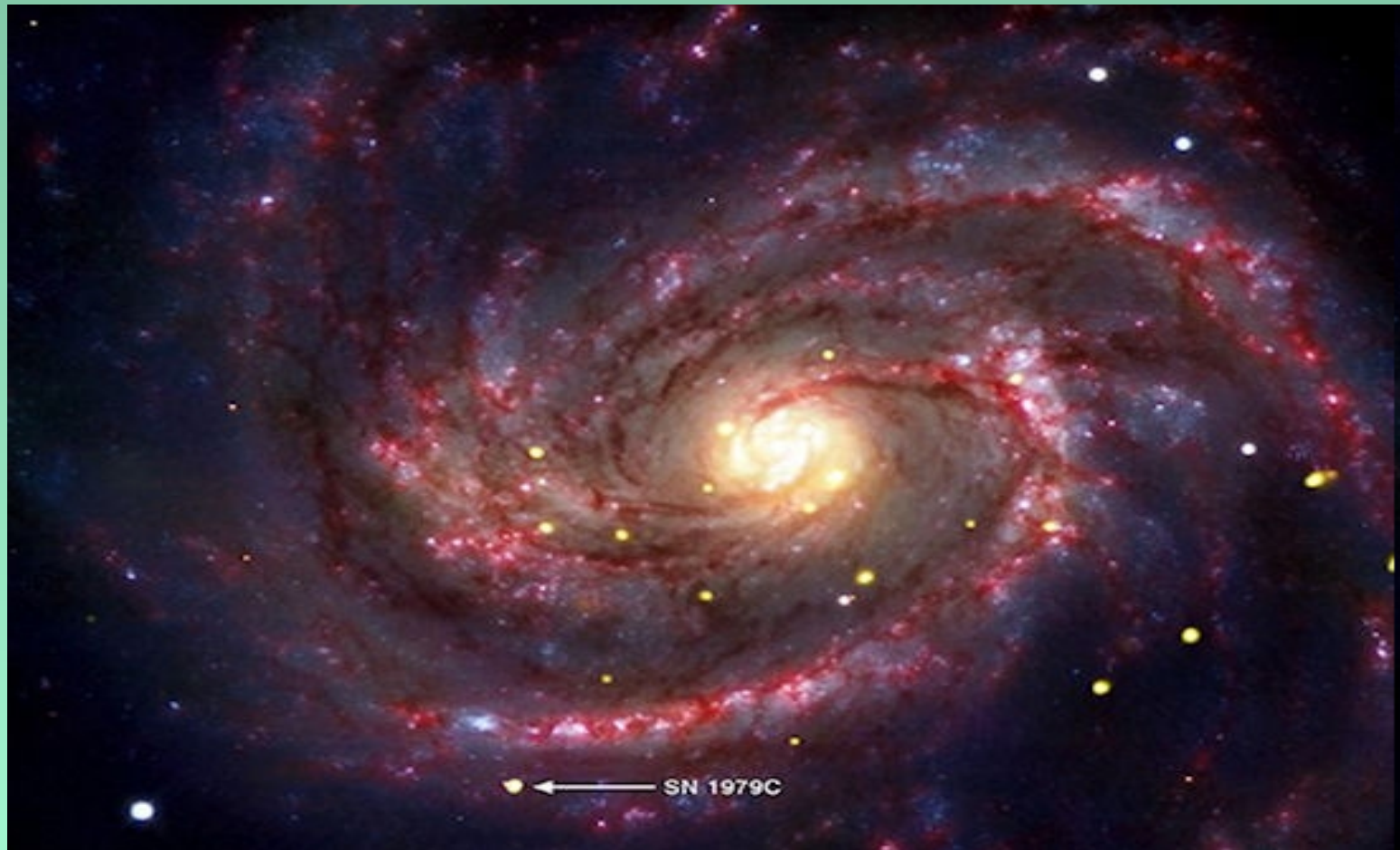
Keywords: Plasmas; Radio emissions; Nonlinear dynamics; Planets; Exoplanets

Star-planet relation: **complex system**



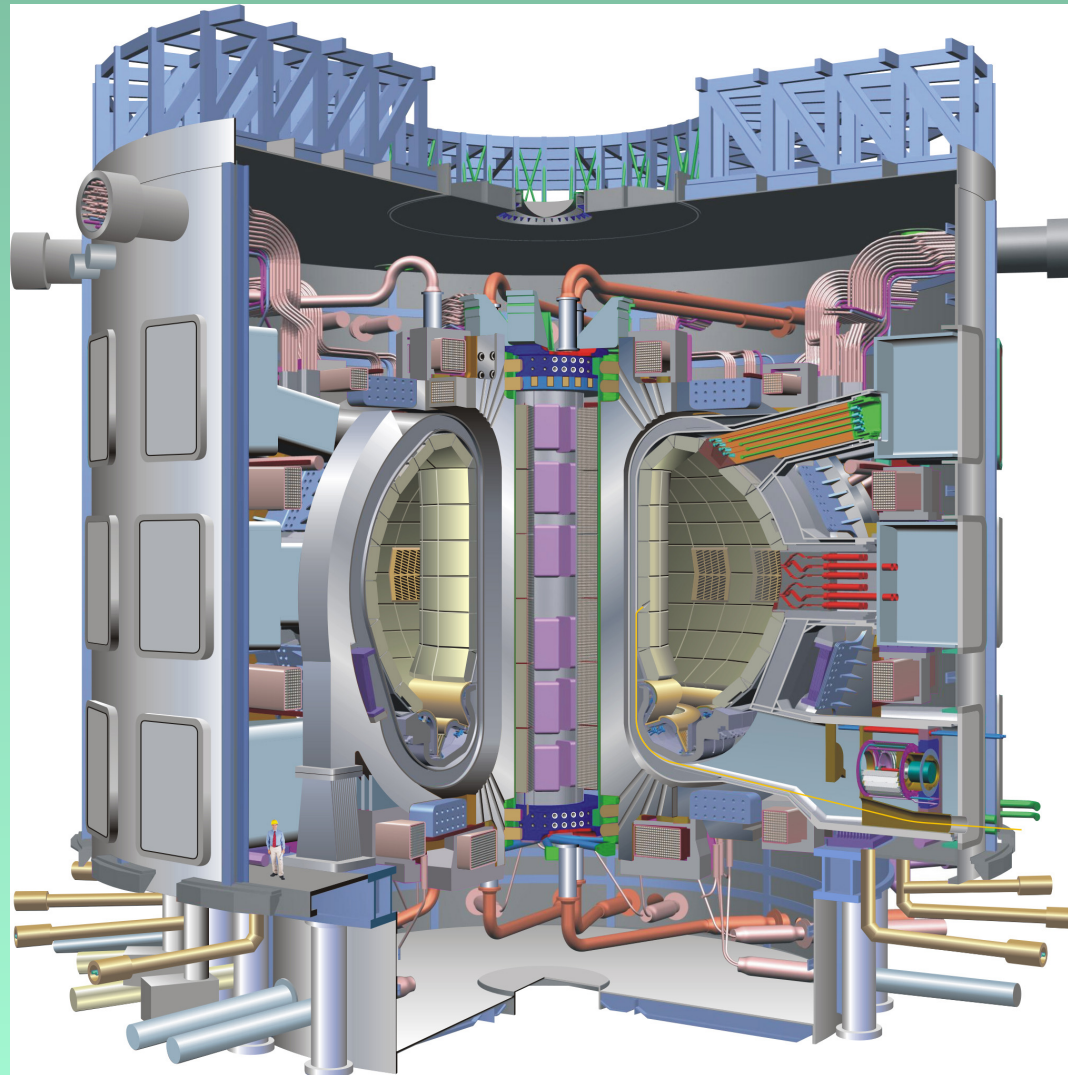
Spiral galaxy: complex system

Discovery of a youngest nearby black hole SN 1979c in M100:
NASA's Chandra X-ray Observatory



Ref: Patnaude et al, New Astronomy (2010)

Controlled Thermonuclear Fusion - ITER



Plasma medicine: an introductory review

M G Kong¹, G Kroesen², G Morfill^{3,5}, T Nosenko^{3,4}, T Shimizu³,
J van Dijk² and J L Zimmermann^{3,4}

¹ Loughborough University, Loughborough LE11 3TU, UK

² Eindhoven University of Technology, 5600 MB Eindhoven, The Netherlands

³ Max Planck Institut für extraterrestrische Physik, D-85748 Garching, Germany

⁴ Institut für Allgemeine Pathologie und Pathologische Anatomie, Technische Universität München, D-81675 Munich, Germany

E-mail: gem@mpe.mpg.de

New Journal of Physics **11** (2009) 115012 (35pp)

Received 29 July 2009

Published 26 November 2009

Online at <http://www.njp.org/>

doi:10.1088/1367-2630/11/11/115012

Abstract. This introductory review on plasma health care is intended to provide the interested reader with a summary of the current status of this emerging field, its scope, and its broad interdisciplinary approach, ranging from plasma physics, chemistry and technology, to microbiology, biochemistry, biophysics, medicine and hygiene. Apart from the basic plasma processes and the restrictions and requirements set by international health standards, the review focuses on plasma interaction with prokaryotic cells (bacteria), eukaryotic cells (mammalian cells), cell membranes, DNA etc. In so doing, some of the unfamiliar terminology—an unavoidable by-product of interdisciplinary research—is covered and explained. Plasma health care may provide a fast and efficient new path for effective hospital (and other public buildings) hygiene—helping to prevent and contain diseases that are continuously gaining ground as resistance of pathogens to antibiotics grows. The delivery of medically active ‘substances’ at the molecular or ionic level is another exciting topic of research through effects on cell walls (permeabilization), cell excitation (paracrine action) and the introduction of reactive species into cell cytoplasm. Electric fields, charging of surfaces, current flows etc can also affect tissue in a controlled way. The field is young and hopes are high. It is fitting to cover the beginnings in *New Journal of Physics*, since it is the physics (and non-equilibrium chemistry) of room temperature atmospheric pressure plasmas that have made this development of plasma health care possible.

⁵ Author to whom any correspondence should be addressed.



Thank you !